Contributions to the Shape Synthesis of Directivity-Maximized Dielectric Resonator Antennas

by

Mohammed Nassor

A thesis submitted in partial fulfillment of the requirements for the Doctor of Philosophy degree in Electrical & Computer Engineering

Ottawa-Carleton Institute for Electrical and Computer Engineering
School of Electrical Engineering and Computer Science
Faculty of Engineering
University of Ottawa

ABSTRACT

Antennas are an important component of wireless ("without wires") communications, regardless of their use. As these systems have become increasingly complex, antenna design requirements have become more demanding. Conventional antenna design consists of selecting some canonical radiator structure described by a handful of key dimensions, and then adjusting these using an optimization algorithm that improves some performance-related objective function that is (during optimization) repeatedly evaluated via a full-wave computational electromagnetics model of the structure. This approach has been employed to great effect in the enormously successful development of wireless communications antenna technology thus far, but is limiting in the sense that the "design space" is restricted to a library of canonical (or regular near-canonical) shapes. As increased design constraints and more complicated placement requirements arise such an approach to antenna design could eventually become a bottleneck. The use of antenna shape synthesis, a process also referred to as inverse design, can widen the "design space", and include such aspects as occupancy and fabrication constraints, the presence of a platform, even weight constraints, and much more. Dielectric resonator antennas (DRAs) hold the promise of lower losses at higher frequencies. This thesis uses a three-dimensional shape optimization algorithm along with a characteristic mode analysis and a genetic algorithm to shape synthesize DRAs. Until now, a limited amount of work on such shape synthesis has been performed for single-feed fixed-beam DRAs. In this thesis we extend this approach by devising and implementing a new shaping methodology for significantly more complex problems, namely directivity-maximized multi-port fixed-beam DRAs, and multi-port DRAs capable of the beam-steering required to satisfy certain spherical coverage constraints, where the location, type and number of feed-ports need not be specified prior to shaping. The approach enables even low-profile enhanced-directivity DRAs to be shape synthesized.

ACKNOWLEDGEMENTS

All praise and thanks be to my Lord, the Lord of the Universe, for His unwavering help, guidance, and blessings throughout my PhD journey. His grace and mercy have been my constant source of strength and inspiration.

I would like to express my heartfelt gratitude to my supervisors, Prof. Derek McNamara and Prof. Mustapha Yagoub, for their unwavering guidance, mentorship, and support throughout my PhD journey. Their expertise, encouragement, and feedback have been invaluable in shaping my research and academic growth.

I am immensely thankful to my family, especially my wife, for their unconditional love, unwavering support, and sacrifices. Their constant encouragement, understanding, and belief in me have been a driving force in my pursuit of higher education.

I am grateful to former members of the Antenna Group in the School of EECS, especially Dr. Hamad Alroughani and Dr. Eqab Almajali, for their support, valuable insights, and contributions to my research. Their guidance, feedback, and encouragement have been instrumental in enhancing the quality of my work.

I would like to extend a special thank you to my esteemed colleague, Dr. Amal Mohammed, for her motivation, inspiration, and camaraderie during our research journey. Her enthusiasm, positivity, and support have been a source of encouragement to me.

I am also grateful to all the professors, researchers, colleagues, and friends who have contributed to my academic and personal growth in various ways.

CONTENTS

LIST OF FIGURES

LIST OF TABLES

LIST OF ACRONYMS

3D	Three-Dimensional
BFN	Beamforming Network
CDF	Cumulative Distribution Function
CEM	Computational Electromagnetics
CM	Characteristic Mode
DRA	Dielectric Resonator Antenna
EIRP	Equivalent Isotropically Radiated Power
EM	Electromagnetics
GA	Genetic Algorithm
IE	Integral Equation
MM	Moment Method
NM	Natural Modes
QFA	Quadratic Form Approach
SIE	Surface Integral Equation
PEC	Perfect Electrical Conductor
VIE	Volume Integral Equation

CHAPTER 1: INTRODUCTION

1.1 MOTIVATION

Antennas are an important component of wireless ("without wires") communications, regardless of their use. As these systems have become increasingly complex, antenna design requirements[1] have become more demanding. Conventional antenna design consists of selecting[2] some canonical (or regular near-canonical) radiator structure described by a handful of key dimensions (features), and then adjusting these using an optimization algorithm[3] that improves some performance-related objective function that is repeatedly evaluated (during optimization) via a full-wave computational electromagnetics model of the structure. This approach has been employed to great effect in the enormously successful development of wireless communications antenna technology thus far, but is limiting in the sense that the "design space" is restricted to a library of regular canonical shapes. As increased design constraints and more complicated placement requirements arise such an approach to antenna design could eventually become a bottleneck. The use of antenna shape synthesis, a process also referred to as inverse design, can widen the "design space", and include such aspects as occupancy and fabrication constraints, the presence of a platform, and much more. Antenna **shape synthesis** is the process of taking a set of desired performance characteristics and other restrictions, and employing an algorithm to actually determine the geometry of the antenna that provides the performance demanded subject to the restrictions.

Antennas can be classified in many different ways: by application, by fabrication/construction method, by geometry/structure, by electrical size, by operating principle, by some specific performance measure, and many more. The principal radiating mechanism for many antennas (e.g. microstrip antennas) is the presence of conduction currents on the conducting portions of the structure. In other antennas (e.g. dielectric resonator antennas), the polarization currents in the dielectric portions of the antenna structure provide the main contribution to the radiated field performance.

[1] By this we mean not only the performance requirements, but non-electrical design constraints as well.
[2] Usually based on much physical insight and experience,
[3] This design route is sometimes called "feature optimization".

There are several advantages[4] offered by **dielectric resonator antennas** (DRAs) that are especially attractive when the operating frequency is in the millimetre-wave frequency range (roughly 30 GHz – 300 GHz). In the antenna field, shape synthesis research appears to have begun in the mid-1990's. The number of publications on the shape synthesis of antennas[5] is relatively small, and (except for one) all have dealt with conducting antennas.

It might seem like hyperbole, but there is a developing broad field of research, crossing many different areas of engineering, referred to as **computational design and manufacturing** (or similar). Its goal, over the next few decades, is this[6] : *You start with the specifications of what some product is supposed to do (that is, its function). Automated tools must figure out the shape and material properties of its parts, not only to achieve the require functionality, but subject to possible constraints on material costs, ease of fabrication, weight, size, form, and so on, even making trade-offs between conflicting objectives. Such computational design must then provide the user with manufacturing instructions to be executed by a group of machines to arrive at the complete physical product (or several component parts). This change is apparently already underway in a number of fields, even that of electronics.* It is very likely that such approaches will eventually involve products with wireless connectivity, and thus automated antenna shape synthesis capabilities will be needed.

1.2 THESIS CONTRIBUTION

We repeat the oft-stated maxim that the ideal antenna synthesis procedure would allow one to "start with a set of electrical, mechanical, and system specifications that would lead to a particular antenna together with its specific geometry and material specification", recognizing that "this ideal general antenna synthesis method does not exist" [STUT 08]. The goal just mentioned is the inspiration, not yet achievable, and progress on antenna shape synthesis has to tackle less ambitious cases of steadily increasing complexity. In this thesis we extend the complexity of DRA problem amenable to shape synthesis.

[4] These are listed in Section 2.3.
[5] These will be reviewed in Section 2.7.
[6] Interview with W.Matusik in *Manufacturing Tomorrow*, April 2018 (www.manufacturingtomorrow.com). The paragraph in italics is a paraphrase of the said interview.

The maximum practical directivity ("normal directivity") that an antenna may possess is limited by the electrical size of the region of space that the antenna structure may occupy. We are here, for a DRA, interested in specifying this size (e.g. low profile requirement), and the electromagnetic properties of the materials that may be used, and then shape synthesizing the DRA, in order to obtain the maximum normal directivity under such (and other) restrictions. We do not wish to specify the details of the feed mechanism(s) of the DRA prior to shaping as this would be an additional restriction. Instead, the locations and number of such mechanisms must only be required in a post-shaping phase, and their selection must be guided by the electromagnetic analyses used during the shape synthesis process. The shape synthesis process reveals the shape with the largest attainable normal directivity under the given constraints; how close we are able to approach this attainable value depends on the complexity of the feed mechanism(s) considered acceptable for a particular design. Such a shape synthesis process for directivity-maximized DRAs (or in fact conducting antennas) has not yet been described by others, and so is being contributed here for the first time. It is applied to both fixed-beam DRAs, and steered-beam DRAs (subject to a probabilistic spherical coverage measure).

1.3 THESIS OUTLINE

Chapter 2 defines the conventional performance metrics used for antennas. The thesis deals solely with dielectric resonator antennas (DRAs), and these are therefore briefly reviewed, but only to the extent that the present work can be placed in context. A brief description of the class of optimization algorithm used in this work is provided. It then outlines existing approaches to driven and eigenvalue computational electromagnetics analysis of dielectric resonator antennas that are used in this thesis. As the title of the thesis suggests, it is the automated shape synthesis of DRAs that is offered as the principal original contribution of this thesis, and thus existing shape synthesis techniques for antennas are overviewed.

The primary goal of **Chapter 3** is to describe the shape synthesis tool developed and implemented as part of the research of this thesis. A flowchart of the shaping process is thus provided and described. The various steps of this process necessitated the derivation of various mathematical expressions and procedures, and these are thus also derived in this chapter. Apart from problem-specific objective functions, at the end of Chapter 3 we have all that is necessary to apply the shape synthesis process to DRA design.

The demonstration, validation and elucidation of the extended shape synthesis method for DRAs developed in Chapter 3 is the subject of **Chapter 4** (fixed-beam cases) and **Chapter 5** (steered-beam case). Finally, **Chapter 6** summarizes the contributions of this thesis and suggests possible future work[7].

[7] Although such suggestions are sprinkled throughout the thesis as well.

CHAPTER 2: FUNDAMENTAL BACKGROUND CONCEPTS & ANALYSIS METHODS

2.1 INTRODUCTORY REMARKS

This chapter offers a review of certain key concepts concerning antennas and computational electromagnetics that are necessary to describe the work presented in Chapters 3 through 6. Section 2.2 defines the conventional[8] metrics in terms of which antenna performance is usually quantified. The thesis deals solely with dielectric resonator antennas (DRAs), and so these are briefly reviewed in Section 2.3, but only to the extent[9] that the present work can be placed in context. Section 2.4 describes how a complete DRA, located on a groundplane, along with its actual feed mechanisms that act as the port(s) of the antenna, can be modelled as a deterministic[10] driven problem. The characteristic mode (CM) concept is used in the research work of the thesis and so it is described in Section 2.5, but once again only to the depth needed for appreciating its usefulness in the thesis. The shape synthesis process must use, as one of its components, some optimization algorithm. We use such algorithms as an existing resource in this work, but a few apposite comments on these are given in Section 2.6. It is important that we be able to convince the reader how the work of this thesis has made original contributions to the subject of antenna shape synthesis generally, and so a review of work done by others on the topic is provided in Section 2.7. Section 2.8 concludes the chapter.

2.2 CONVENTIONAL ANTENNA PERFORMANCE MEASURES

2.2.1 Antenna Input/Output Port Properties

Any antenna has a port at which the desired signals are input (transmitting case) or extracted (receive case). Fig.2.2-1 shows a transmission line that connects the transmitter to an antenna[11]. A certain amount of power P_{inc} is incident on the antenna terminals. Due to mismatch between

[8] A somewhat "unconventional" metric is described in Section 3.4.
[9] More extensive literature reviews for such antennas are available in the literature, and these will be referenced in Section 2.3.
[10] Deterministic as opposed to an eigenvalue problem.
[11] We will here discuss antennas as if they are transmitting. All of the antennas in this thesis are composed of isotropic linear (and hence reciprocal) materials, and so the performance in the receiving situation will always be the same as in the transmitting situation.

the transmission line and the antenna some of this power (P_{refl}) is reflected back towards the transmitter with the remainder P_{in} accepted by the antenna, giving

$$P_{in} = P_{inc} - P_{refl} \tag{2.2-1}$$

Of the power (2.2-1), a portion P_{loss} is dissipated on the antenna structure due to material losses, and the rest P_{rad} is radiated, so that

$$P_{rad} = P_{in} - P_{loss} \tag{2.2-2}$$

Antenna designers wish, for a given P_{inc}, to maximize P_{rad} by minimizing P_{refl} and P_{loss}. An important quantity, then, is the input reflection coefficient Γ_{in}, which is defined such that

$$|\Gamma_{in}|^2 = P_{refl} / P_{inc} \tag{2.2-3}$$

at the antenna input terminals. The electromagnetic wave transporting P_{rad} is in many cases also required to be of a certain polarization. And all the above requirements must be met at frequencies f over a specific frequency band $f_L \le f \le f_U$ between lower frequency f_L and upper frequency f_U.

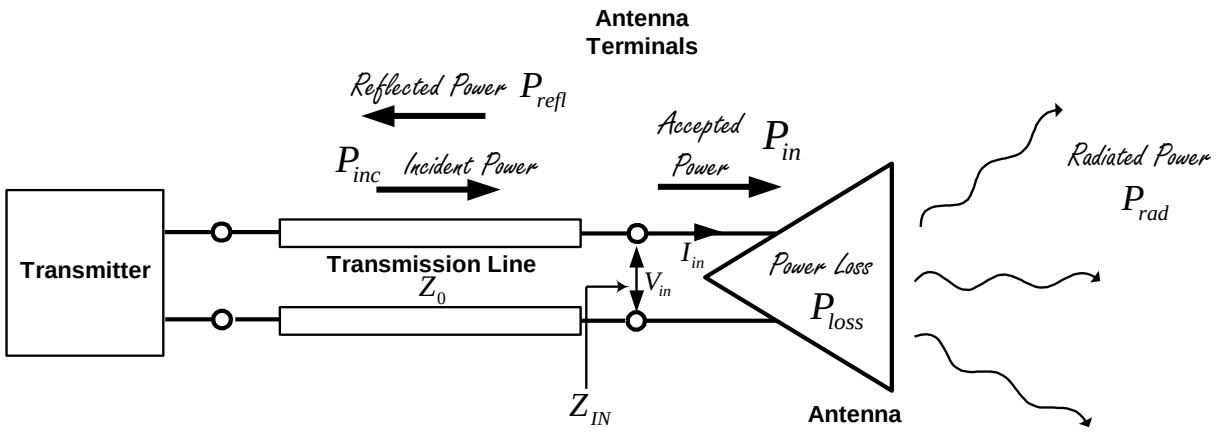

Figure 2.2-1: Power budget for an antenna. (After [MCNA 20])

2.2.2 Far-Zone Fields & Radiation Patterns of Antennas

Any antenna's electromagnetic field can be described as (with respect to the specified coordinate origin)

$$\bar{E}(r,\theta,\phi) = E_\theta(r,\theta,\phi)\,\hat{\theta} + E_\phi(r,\theta,\phi)\,\hat{\phi} + E_r(r,\theta,\phi)\,\hat{r} \qquad (2.2\text{-}4)$$

where (r,θ,ϕ) denotes a point of observation in the three-dimensional space around the antenna. The direction of the observation point is given by the pair of angles (θ,ϕ), while the distance from the coordinate system's origin is given by r, as shown in Fig.2.2-2. The fields in the far-zone region can be separated into direction-dependent and distance-dependent parts as [MCNA 20]

$$\bar{E}(r,\theta,\phi) = \bar{E}(\theta,\phi)\frac{e^{-jkr}}{r} = \left\{E_\theta(\theta,\phi)\,\hat{\theta} + E_\phi(\theta,\phi)\,\hat{\phi}\right\}\frac{e^{-jkr}}{r} \qquad (2.2\text{-}5)$$

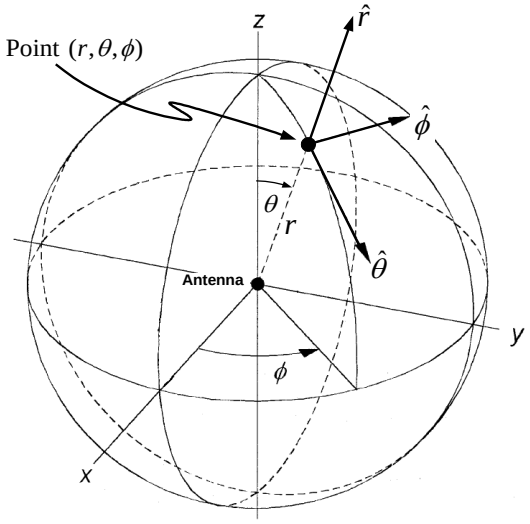

Figure 2.2-2: Spherical coordinate system. (After [MCNA 20])

2.2.3 Directivity of an Antenna

The (total) directivity $D(\theta,\phi)$ of an antenna in direction (θ,ϕ) is defined as[12]

$$D(\theta,\phi)=\frac{\text{Radiation Intensity in Direction }(\theta,\phi)}{\text{Spatially Averaged Radiation Intensity}} \tag{2.2-6}$$

As a result, the (total) directivity may be expressed as

$$D(\theta,\phi)=\frac{4\pi U(\theta,\phi)}{P_{\text{rad}}} \tag{2.2-7}$$

with (total) radiation intensity being

$$U(\theta,\phi)=\frac{\left|\bar{E}(\theta,\phi)\right|^2}{2\eta_o} \tag{2.2-8}$$

and the total radiated power (TRP) being

$$P_{\text{rad}}=\int_0^{2\pi}\int_0^{\pi}U(\theta,\phi)\sin\theta\,d\theta\,d\phi=\frac{1}{2\eta_o}\int_0^{2\pi}\int_0^{\pi}\left|\bar{E}(\theta,\phi)\right|^2\sin\theta\,d\theta\,d\phi \tag{2.2-9}$$

where $\bar{E}(\theta,\phi)$ is the electric field in the far-zone region and $\eta_o=\sqrt{\mu_o/\varepsilon_o}$ the intrinsic impedance in free space. Expression (2.2-8) allows us to write (2.2-7) as

$$D(\theta,\phi)=\frac{2\pi}{\eta_o}\frac{\left|\bar{E}(\theta,\phi)\right|^2}{P_{\text{rad}}} \tag{2.2-10}$$

Directivity is typically expressed in deciBels (dBi), namely

$$D^{dBi}(\theta,\phi)=10\log\{D(\theta,\phi)\} \tag{2.2-11}$$

If $\bar{E}(\theta,\phi)$ in all the above expressions is replaced by $\bar{E}_\theta(\theta,\phi)$, the resulting quantity in (2.2-10) will provide the partial directivity $D_\theta(\theta,\phi)$; if $\bar{E}(\theta,\phi)$ is replaced by $\bar{E}_\phi(\theta,\phi)$, the resulting quantity in (2.2-10) will provide the partial directivity $D_\phi(\theta,\phi)$; and similarly for other polarization components.

[12] IEEE Std 145 : *IEEE Standard for Definitions of Terms for Antennas.*

2.2.4 Gain of an Antenna

The gain of an antenna is related to the directivity as

$$G(\theta,\phi) = \eta_{\text{rad}} D(\theta,\phi) \tag{2.2-12}$$

where

$$\eta_{\text{rad}} = P_{rad} / (P_{rad} + P_{loss}) \tag{2.2-13}$$

is the radiation efficiency. The *realized* gain of the antenna is defined as [MCNA 20]

$$G_{realized}(\theta,\phi) = \left(1 - \left|\Gamma_{in}\right|^2\right) \eta_{\text{rad}} D(\theta,\phi) \tag{2.2-14}$$

Similarly, the partial gains are defined as $G_\theta(\theta,\phi) = \eta_{\text{rad}} D_\theta(\theta,\phi)$ and $G_\phi(\theta,\phi) = \eta_{\text{rad}} D_\phi(\theta,\phi)$.

2.2.5 Equivalent Isotropically Radiated Power (EIRP) of an Antenna

The equivalent isotropically radiated power (EIRP), in a given direction (θ,ϕ), is the gain $G(\theta,\phi)$ of a transmitting antenna in that direction, multiplied by the net power accepted (P_{in}) by the antenna from the transmitter. In other words,

$$EIRP(\theta,\phi) = P_{in}\, G(\theta,\phi) \tag{2.2-15}$$

2.2.6 Axial Ratio of an Antenna

The polarization of an antenna in some direction (θ,ϕ) can be quantified in terms of its axial ratio (AR) in that direction. If the far-zone fields are $\bar{E}(\theta,\phi) = E_\theta(\theta,\phi)\,\hat{\theta} + E_\phi(\theta,\phi)\,\hat{\phi}$, then the axial ratio in direction (θ,ϕ) can be found as

$$AR(\theta,\phi) = \frac{\left|\rho_c(\theta,\phi)\right| + 1}{\left|\rho_c(\theta,\phi)\right| - 1} \tag{2.2-16}$$

with quantity

$$\rho_c(\theta,\phi)=\frac{1+j\rho_\ell(\theta,\phi)}{1-j\rho_\ell(\theta,\phi)} \tag{2.2-17}$$

found from

$$\rho_\ell(\theta,\phi)=\frac{E_\phi(\theta,\phi)}{E_\theta(\theta,\phi)} \tag{2.2-18}$$

The far-zone fields of an actual antenna are elliptically polarized in general. The axial ratio is a signed quantity, the sign indicating the sense of the elliptical polarization. Its magnitude is usually expressed in dBs as $AR^{dB}(\theta,\phi)=20\log\{|AR(\theta,\phi)|\}$. If $|AR^{dB}|=0$ we have perfect circular polarization (CP) and for perfect linearly polarization (LP) we have $|AR^{dB}|\to\infty$.

2.3 DIELECTRIC RESONATOR ANTENNAS (DRA)

Many dielectric resonator antenna designs have been published that offer quite astounding performance: low loss, wide bandwidth and small physical/electrical size compared to alternative conducting antennas. It is thus **important to recognize** that we are not here trying to imply that the shape synthesis method to be developed could offer DRAs with a performance that exceeds such achievements. Instead, the goal of this thesis is the development of a shape synthesis method for DRAs that can provide us with a DRA design in an automated manner subject to constraints such as the allowable volume (size and external form) occupied by the DRA, the material parameters prescribed (e.g. for reasons such as cost, ease of fabrication, amount of loss, mass, and so on), the vicinity of other scattering objects (e.g. when the DRA must be mounted on some platform), and other restrictions. In other words, it can provide some desired performance subject to constraints that could not be taken into account if conventional design methods were used. Although a comprehensive review of DRAs is therefore not required, it is sensible to provide some remarks on this type of antenna.

DRAs with astonishingly good performance are described in both earlier reviews that remain relevant [PETO 07][KISH 07][PETO 10][LIAN 08][KEYR 16], and more recent ones [DASH 17][MUKH 20][SING 22][ALAN 23], all of which contain copious references. At first, canonical shapes, such as rectangular and circular cylinders, were used, with coaxial probe, slot, proximity,

and microstrip-fed conformal conducting probe [LIAN 08] feeding mechanisms. Information on the natural modes[13] (NMs) of the particular DRA geometry, determined either approximately or using numerical methods, were used to assist in design work. Impedance bandwidths of up to 38% were reported. Subsequent work used alternative near-canonical dielectric geometries (e.g. stepped, H-shaped, P-shaped, L-shaped, arched, tetrahedral), as well as multi-dielectric conventional shapes, with impedance bandwidths approaching 85%. Discussions on the latter DRAs [YAO 21][CHAI 07][LIAN 08][IQBA 15][THAM 10] reveal that the shapes were selected based on insightful physical arguments (e.g. coupled resonator ideas also used in microstrip patch antenna work) rather than direct use of the NMs of the near-canonical dielectric geometries.

Most DRAs are designed so that the polarisation currents in the dielectric material constitute the main source of radiation. With so-called hybrid DRA structures [ZUO 21][PETO 10], the conduction currents of the feed mechanism, and other intentionally located conductor shapes, are purposely allowed to contribute significantly to the radiation characteristics via its conduction currents. Case where metasurface groundplanes [QAMA 20], metasurface superstrate [MISH 21], as well as internally located split-ring resonators [ZHAN 21] and metasurfaces [ZHEN 20] are used can be classified as such hybrid DRAs as well. Although often successful, much of this work has been undertaken in a phenomenological manner, using exhaustive parametric studies (based on full-wave computational electromagnetics driven models) of conjectured geometries, rather than the more insightful approaches (with electromagnetic-physics-based explanations) adopted a decade ago for the near-canonical and hybrid configurations.

A study of the findings in the above-mentioned references, amongst others, reveals the following:

■ *Potential Compactness* – The size of DRA is proportional to $\lambda_o / \sqrt{\varepsilon_r}$ compared to λ_o in conducting antennas[14] with ε_r the relative permittivity of the material forming the DRA. Compactness is highly desirable in modern wireless technology, especially mobile devices. Although DRAs can indeed be compact, they are not as low-profile as microstrip patch-like antennas.

[13] Defined in Section 2.5.1.

[14] Symbol λ_o denotes the free space wavelength.

■ *Potential High Radiation Efficiency* – Conducting antennas such as microstrip patch-like suffer from increasing conductor losses with increasing frequency, especially troublesome at millimetrewave frequencies. DRAs do not have the level of metallic losses (only the groundplane) and can have a high radiation efficiency when a low-loss dielectric material is chosen. Although DRAs have not yet become "workhorse" antennas (such as monopoles, dipoles and microstrip patches) in wireless systems, many believe that their use will become a necessity when such systems move to ever-increasing millimetrewave frequencies, especially if low-profile versions are available. Hybrid DRA designs do not necessarily possess this advantage to the same extent.

■ *Variety of Feeding Mechanisms Possible* – different ways such as microstrip line/beamforming-network feed (proximity feed), coplanar waveguide feed, aperture coupling feed (slot feed, such as microstrip fed slots and slots in the wall of a rectangular waveguide), and coaxial probe feed can be used to excite DRAs, which is useful in a variety of applications.

■ *Large Impedance Bandwidth* - DRAs have been designed with significantly larger impedance bandwidths than conducting antennas. Even if such bandwidths are not needed, their wide bandwidths permit the relaxation of fabrication tolerances.

■ *Ease of Fabrication* - Low loss and suitable permittivity materials for 3D printers are under development specifically for RF applications. Thus 3D printing[15] of DRAs directly onto electronics layouts (that is, easy integration with electronics) will become feasible in future manufacturing. There are still problem issues printing "RF-friendly" materials [NGUY 21][HU 21][ELSA 22][HEHE 21], and problems experienced by the present author are discussed in Section 3.7. It is expected that these will be overcome as 3D printing technology rapidly improves due to its widespread application.

In seeking meaningful examples for which to apply the shape synthesis developed in this thesis, namely its application in Chapters 4 and 5, we chose the problem of designing **enhanced-directivity low-profile DRAs** since relatively little has been published by others on the specific topic. Authors do not always agree on what is meant by the terms "miniaturized", "compact" and "low-profile" with reference to antennas. For instance, some call reflectarray antennas low-profile

[15] The 3D printing of both dielectric and metal objects has been hailed as the automated manufacturing route of the future in all spheres of engineering.

because the reflecting meta-surface is flat compared to the solid paraboloidal reflector (or ellipsoidal/hyperboloidal sub-reflector) it emulates. However, the antenna as a whole is not low-profile because a feed radiator is needed at some focal point. Similar comments apply to transmitarray antennas. We use the criterion in [ESSE 96] that considers a DRA to be a low-profile antenna if the ratio of its largest horizontal dimension (L) to its largest vertical dimension (H) is such that $L/H > 6$, without having to use relative permittivities larger[16] than about 15. Examples of low-profile DRA designs are those in [ESSE 96], [PAN 16], [WANG 22], [ZHOU 22] and [LIU 23], as well as Section 6.3 of [PETO 07]. Following the lead provided in papers reporting "enhanced-directivity" or "high-gain" DRA designs, we consider enhanced-directivity DRAs to be those whose directivities are larger than 6dBi. The review in [WANG 22] identifies (from the almost thirty references quoted there) the following approaches to enhanced-directivity DRA design : the use of a small array of low-directivity DRA elements; the use of hybrid DRAs with conducting structures; engraving of the walls of the DRA with grooves or other perturbations; the use of stacked dielectric layers; the use of higher-order natural modes; the use of combinations of the afore-mentioned approaches. However, such enhanced-directivity DRAs are usually not low-profile ones according to the above-mentioned criterion, although some are (e.g. [PAN 16] [WANG 22]). Values for the directivity reported[17] as being enhanced are typically below 12 dBi.

2.4 DIELECTRIC RESONATOR ANTENNA FULL-WAVE ANALYSIS: *DRIVEN PROBLEM*

In the language of rigorous electromagnetic modelling, a DRA consists of a dielectric object, usually in the presence a large conducting object ("groundplane") and perhaps a small conducting object that forms the feed mechanism of the DRA, plus some impressed source (located somewhere on the feed mechanism). It is well-known that the integral equation or differential equation models for the performance analysis of a DRA do not have analytical solutions except for certain idealized situations (e.g. sphere; hemisphere on groundplane). The methods of computational electromagnetics (CEM) can fortunately be used to find solutions to the above-mentioned models, the method of moments (MM) in the case of integral equation models and the

[16] Materials with relative permittivities larger than 38 are heavy, and at present do not appear to be in development for 3D printing.
[17] We do not include here DRAs that are backed by some sort of cavity

finite element method (FEM) in the case of differential equation models. Thus, it is possible to calculate the performance of DRAs via the above **driven problem** models using the methods of CEM [PETE 97]. The commercial code "FEKO" [ALTA 21] will be used for MM full-wave analysis, and "HFSS" [ANSY 20] for essentially FEM-based full-wave analysis, of the driven problem models of DRAs obtained through the shape synthesis procedure developed in this thesis[18]. Such full-wave modelling is an essential part of shape synthesis. However, it should be realized that the above-mentioned codes, on their own, **do not allow one to perform the shape synthesis of any type of antenna**[19]. They are solely the CEM engines that form part of the overall tool[20] whose development here implements an extended shape synthesis approach.

If we were to use a volume integral equation (VIE) approach[21] [PETE 97] for the analysis of a DRA on an infinite PEC groundplane) the associated VIE would be discretized, using the MM, into a matrix equation of the form

$$[Z][J]=[V^{inc}] \tag{2.4-1}$$

Column vector [J] contains the coefficients describing the electric volume current density in the DRA, which is found as the solution to matrix equation (2.4-1). Column vector $[V^{inc}]$ is the excitation (or driving) term, that depends on the incident field generated by the known impressed (as opposed to induced) sources. Matrix $[Z]$ is the moment method matrix that is in essence the discretized form of the integral operator of the VIE. Once [J] has been found all the associated fields can be determined, for the DRA with the specified impressed sources. If a surface integral equation (SIE) model were to be used for the same driven problem, there would be two equivalent surface current densities (one electric and the other magnetic), on the surface of the DRA geometry, instead of a single volume electric current density.

[18] The use of two different CEM methods to solve the same problem is widely recommended to provide confirmation of the soundness of the modelling.
[19] But can be used for feature optimization based design.
[20] Described in Section 3.5.
[21] The VIE approach is computationally time-consuming, and in practice it is usual to utilize a surface integral equation (SIE) route. However, the intention here is not to reproduce mathematical detail (which is available elsewhere) but to elucidate some CEM aspects in as straightforward a manner as possible. The VIE route allows us to do this succinctly, and so it is used for purposes of explanation.

2.5 DIELECTRIC RESONATOR ANTENNA FULL-WAVE ANALYSIS: *EIGENVALUE PROBLEM*

2.5.1 Natural Modes (NMs)

Conventional DRA design has been very successful by viewing such antennas from the point of view of their natural modes (NMs). A natural mode of an object is one that can exist in the absence of sources (that is, with zero incident field). Its electromagnetic field satisfies Maxwell's equations, the physical continuity conditions dictated by the object, and the radiation condition. Its mathematical form is that of an **eigenvalue problem**. All physical objects have natural electromagnetic modes with which are associated resonant frequencies, being the only frequencies at which there can be (the particular) non-zero field distribution in the absence of sources. When designers talk of a DRA's "resonant modes", it is usually these NMs that are being referred to. They have been essential in the understanding, development and design of DRAs. Numerical calculation of the NMs of a DRA is computationally extremely burdensome [KAJF 83][KAJF 84] [LIU 04] and involves[22] the matrix equation

$$[Z][J]=[0] \tag{2.5-1}$$

The matrix $[Z]$ is a function of frequency ω. One searches for those frequencies for which[23] $\det[Z]=0$; these are the resonance frequencies of the NMs.

2.5.2 Characteristic Modes (CMs)

In this thesis we will not use NMs. Instead, we will use another type of mode, namely the characteristic modes[24] (CMs) of the DRAs. The preference for using CMs instead of NMs lies in their computational ease when applied to the specific problem of interest, particularly in the case of open dielectric resonators. CMs involve solving linear eigenvalue problems, making their computation more straightforward compared to NMs, which require solving non-linear eigenvalue

[22] The [Z] and [J] are those referred to in Section 2.4.

[23] This is known as a non-linear eigenvalue problem, and is computationally extremely time-consuming.

[24] Researchers have expressed interest in applying the CM concept in essentially two ways. The majority of antenna designers who have used CM analysis have done so in an indirect manner, utilizing the physically intuitive guidance that such CMs provide [DENG 19][DICA 18][KIM 19][BOYU 22]. A few have used CM analysis directly in antenna shape synthesis [ETHI 14][YANG 19][ALAK 21]. In this thesis, CM analysis is also used directly to automate antenna shaping.

problems and are computationally intensive. Additionally, other advantages of CMs over NMs have been highlighted in [ALRO 18], further reinforcing their suitability for the described application. CMs can be found for conducting objects, dielectric objects, and composite conducting/dielectric objects. If we wish to find the CMs of a dielectric object located on an infinite PEC groundplane, the VIE approach mentioned previously can be used[25]. The matrix $[Z]$ is separated into its real and imaginary parts as $[Z]=[R]+j[X]$. The CMs are the solutions of the generalised matrix eigenvalue problem[26] [HARR 72]

$$[X][J_n]=\lambda_n[R][J_n] \tag{2.5-2}$$

Quantity λ_n is the eigenvalue, and $[J_n]$ the eigencurrent column vector, of the nth CM at some specific frequency. Eigenvalue λ_n is zero at the resonance frequency of the nth CM; it has a large value away from the resonance frequency. The "order" of the CMs over a given frequency range is ascribed according to the value of $|\lambda_n|$; higher order modes have larger values of $|\lambda_n|$.

Once $[J_n]$ is known, the associated eigenfields $(\bar{E}_n, \bar{H}_n)$ of the nth CM at the specific frequency can be determined. It can be shown that the CM far-zone fields are orthogonal in the sense

$$\frac{1}{\eta_o}\iint_{S_\infty}\bar{E}_m\cdot\bar{E}_n^* dS=\frac{1}{\eta_o}\iint_{S_\infty}\bar{H}_m\cdot\bar{H}_n^* dS=\delta_{mn} \tag{2.5-3}$$

where $\eta_o=\sqrt{\mu_o/\varepsilon_o}$ and S_∞ is the "sphere-at-infinity" enclosing the object. The volume current density satisfies similar orthogonality properties [HARR 72]. Because of the above-mentioned orthogonality properties, it is possible, when an impressed source is indeed specified (so that we have a driven problem), to express the actual current density and fields of the driven problem as a linear combination of the CM eigencurrents and eigenfields of the DRA in the forms

$$\bar{J}_s(\bar{r})=\sum_{n=1}^{\infty}\alpha_n\bar{J}_n(\bar{r}) \tag{2.5-4}$$

[25] With a modified Green's function in the VIE accounting for the presence of the infinite PEC groundplane [ALRO 14a][WU 17].

[26] This is a linear eigenvalue problem, and far less taxing computationally than the non-linear eigenvalue problem needed to find the NMs.

$$\bar{E}(\bar{r}) = \sum_{n=1}^{\infty} \alpha_n \bar{E}_n(\bar{r}) \qquad (2.5\text{-}5)$$

$$\bar{H}(\bar{r}) = \sum_{n=1}^{\infty} \alpha_n \bar{H}_n(\bar{r}) \qquad (2.5\text{-}6)$$

where α_n is the so-called modal weighting coefficient of the nth mode. It enables one to measure "how much" of each of the characteristic modes is excited for a given excitation. It can be expressed (in this case of the VIE analysis) as [HARR 72]

$$\alpha_n = \frac{\left\langle \bar{J}_n, \bar{E}^{inc} \right\rangle}{1 + j\lambda_n} \qquad (2.5\text{-}7)$$

where $\bar{E}^{inc}$ is the incident field due to the impressed source, and $\left\langle \bar{J}_n, \bar{E}^{inc} \right\rangle$ is a quantity containing an integral over the DRA object. The quantity

$$MS_n = \left| \frac{1}{1 + j\lambda_n} \right| \qquad (2.5\text{-}8)$$

is called the modal significance factor. We note that we can view the modal weighting coefficient relationship as

$$|\alpha_n| = |\text{ Excitation Coefficient }| \times MS_n \qquad (2.5\text{-}9)$$

It is important to notice that at frequencies away from resonance the MS_n decreases and, as is evident from expression (2.5-9), the particular CM is not as easily excited for the same $\bar{E}^{inc}$. Once an impressed source has been specified, the resulting CM modal weighting coefficients can be relatively easily determined. The coupling between an impressed source and the NMs of the object is not at all straightforwardly calculated [PEAR 84][LAWR 10]. Indeed, the computation of such coupling factors does not appear to have been used in DRA design work, though much of this work has examined the field distributions of the NMs and (qualitatively) successfully devised ways to excite selected NMs.

In practice the use of an SIE approach [CHAN 77] is computationally significantly more efficient than using a VIE approach. This applies if one is using homogenous DRA structures, as is the case in this thesis. The MM formulation, and its use in finding the CMs of the DRA object, is somewhat more involved than the VIE route, but all the CM properties and their consequences, mentioned earlier in this section still apply. Specifically, the relationship of the form (2.5-9) still applies, although the excitation coefficient depends on both the incident electric and magnetic fields, and both kinds of equivalent current densities (that is, electric and magnetic) are required in the SIE formulation.

2.5.3 Sub-Structure Characteristic Modes

Sub-structure CMs were first proposed for PEC objects in [ETHI 12][ALRO 16], and then expanded to include dielectric objects in [ALRO 14b]. This is a convenient tool for investigating the CMs of a single object in the presence of another object. Consider the objects A and B in Fig.2.5-1. In the present context we would consider object A to be the DRA material, and object B to consist of conducting/dielectric material considered to be the platform on which the DRA proper is located. We would be interested in finding the set of CMs for object A in the presence of object B. These would be the sub-structure CMs of the DRA object, with properties similar to those of the conventional CMs listed in Section 2.5.2.

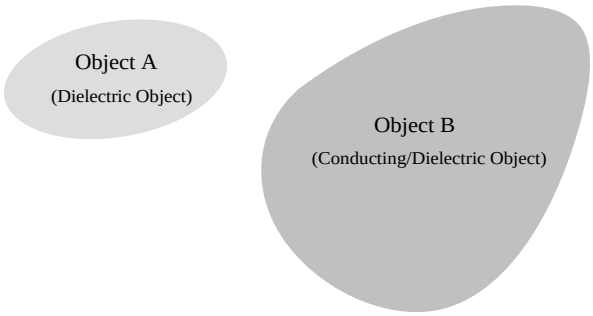

Figure 2.5-1: Sub-structure CMs with two material objects.

2.6 OPTIMIZATION ALGORITHMS

In this work we are not making any claim as to having contributed to the details of some new optimization algorithm. The thesis will use existing optimization algorithms[27], and their implementation in [MATLAB], as an available resource. The thesis contributions have to do solely with the shape synthesis of DRAs, and so we will simply use a particular existing optimization algorithm. It is always good to put one's choices in context though, and so we here very briefly review what optimization algorithms are extant.

Let us consider a multivariable real function $F_{obj}(a_1, a_2, ..., a_n, ..., a_N)$ whose independent variables $\{a_1, a_2, ..., a_n, ..., a_N\}$ can be viewed as a point in N-dimensional space. Optimization algorithms are numerical schemes that systematically adjust the optimization variables a_n, also referred to as the degrees of freedom (DoF) of the optimization, as they attempt to locate the N-dimensional point $\{a_1, a_2, ..., a_n, ..., a_N\}$ where F_{obj} achieves its minimum (or maximum[28]) value. Function F_{obj} is called the objective function for the optimization. Such optimization algorithms, of which there are many, can be classified into ones that are gradient based (that is, explicitly use derivative information on F_{obj} with respect to the independent variables), and those that do not (usually referred to as evolutionary algorithms). Different gradient-based algorithms use gradient information to navigate their way to the point at which F_{obj} is a maximum in distinct ways [BAND 69][BAND 88]. The principal optimization algorithm in the shape synthesis development in this work is an evolutionary one known as the genetic algorithm (GA) [GOLD 89]. Optimization algorithms are characterized as either performing optimization without constraints or with constraints. Often, when working with antennas, constraints do not fit neatly into a mathematical framework, and so unconstrained optimization algorithms are used with constraints incorporated into the objective functions.

[27] These optimization algorithms will, of course, be used in a different way in the new shaping algorithm than what has been done previously.

[28] In the present work it makes more sense to talk of maximization (we will always wish to maximize antenna directivity), and we will always define F_{obj} as a function to be maximized, although we in fact minimize $-F_{obj}$ to achieve this.

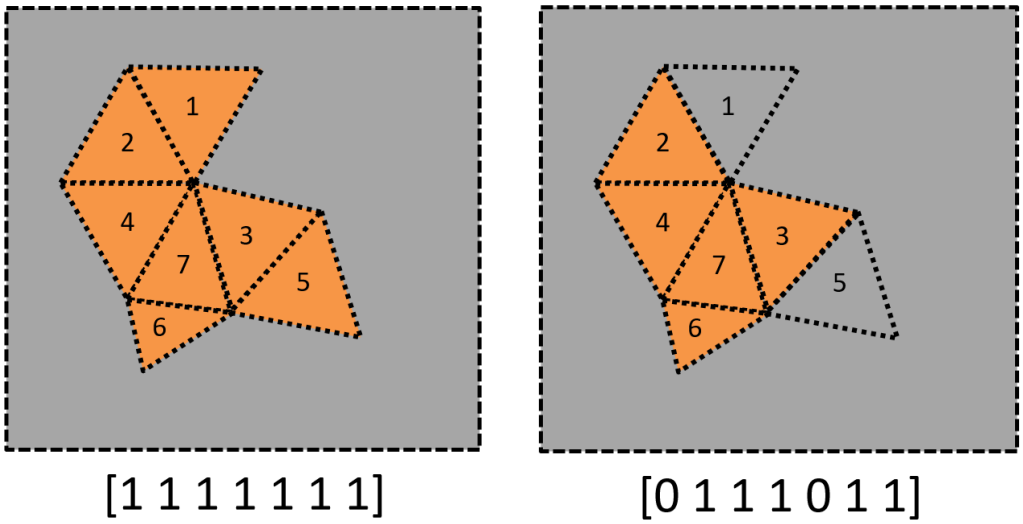

Figure 2.6-1: Planar conductor shapes described by the binary variables ("chromosomes") shown. In actual shape synthesis the binary variables will consist of many more bits in order to achieve the necessary geometrical resolution.

We outline the operation of the GA by describing its essence in connection with the shaping of a planar conducting shape[29] that we can imagine to be some fictitious conducting antenna. The conducting surface is shown in Fig.2.6-1 and has been divided into a mesh of 7 triangles[30]. Each triangle can be filled with conductor, as for all the triangles in Fig.2.6-1(left), or some triangles may be unfilled, as in Fig.2.6-1(right). We can associate a 1 or a 0 with each element, a 1 if it is filled with conductor and a 0 if it is not. In the terminology of the GA[31], we can define a chromosome that consists of a string of 7 bits, and map each chromosome bit to a different triangle in the meshed geometry. This is illustrated by the binary chromosomes [1 1 1 1 1 1 1] and [0 1 1 1 0 1 1] shown below each of the layouts in Fig.2.6-1. By altering the binary values of each bit a different conducting geometry can be defined. An F_{obj} is defined that is a function of the binary value of each bit constituting the chromosome. Because it is thus a function whose independent variables are the bits in the chromosome, F_{obj} is a function of the shape of the conductor. Function

[29] We do this so as to be able to refer to it when reviewing the shape synthesis of conducting antennas in Section 2.7. More will be said about the application of the GA to a volumetric dielectric object in Section 3.5.
[30] These need not be triangles. They could be rectangles.
[31] One advantage of the GA is that it can be used in binary form (as being described here, and will be used in the shaping process developed in this thesis), where the optimization variables are represented by the chromosomes under discussion, or they can be used with continuous variables. The need for the latter capability is mentioned in the second part of Section 3.5.2, and used in the post-shaping feed mechanism design step in Section 5.2.4 of Chapter 5.

F_{obj} must somehow translate the desired requirements of the shaping process into a quantitative expression, and so will depend on what performance it is we actually want to achieve. Continuing to purposefully think in terms of the GA being used with the shaping of conducting antennas, we realize that computational electromagnetics (CEM) would have to be used to evaluate the electromagnetic behaviour, and hence an objective function F_{obj}, no matter how it is defined for a specific problem, for each different conductor shape. The binary dependence of the shape makes it tricky to define a gradient even though an appropriate F_{obj} may be "easy" to compute. The fact that GA's do not use gradients of the objective function has made them suitable in certain conducting antenna shape synthesis problems.

All optimization algorithms, and hence the GA too, need a starting point. The GA therefore randomly generates a set of N_{pop} different chromosomes. This is the initial "population" of conductor shapes, each shape being a member of the population. N_{pop} is called the population size. Once such a population has been created, each member is ranked according to its F_{obj} value. In a structured way, the GA then selects[32] the best members (those with the lowest F_{obj} values) of the population, and discards the others. These "elite" population members are mated[33], and generate offspring that are subsequently integrated into a new population of size N_{cond}. The ranking, selection and mating process is then continually repeated. The goal is that a gradual increase in the value of F_{obj} will occur as the GA iterates from generation to generation – in other words that the chromosome that gives the maximum F_{obj} will be approached. As expected, the larger the value of N_{pop} the better the chances of F_{obj} actually reaching its physically possible maximum value. If we recall that (at least in the antenna context) full-wave CEM analysis is needed each time F_{obj} is evaluated for each population member, it is appreciated that there will

[32] Many methods of *selection* have been developed, and are available in the commercial GA software identified in Section 3.5.1.

[33] Using so-called mating operators, that include the operations of crossover, mutation and migration. The relative dominance of the afore-mentioned approaches can also be chosen by the user in the commercial GA software identified in Section 3.5.1. There are only rules-of-thumb (that is, no rigorous advice) on precisely how to set such parameters of the GA, as these are problem-dependent. In this work we have each time used a few trial runs with slightly different settings and observed which are best for the particular shape synthesis problem being pursued.

need to be some trade-off in selecting the value of N_{pop}, lest the whole process become unfeasibly computationally time-consuming. It is possible for the GA to stagnate when subsequent generations no longer differ much from previous ones (are not sufficiently 'genetically diverse'), and then so-called mutation operations are used to break out from this by infusing new genetic material into new generations. Once again, in common with all optimization algorithms, the GA must eventually be halted according to some criterion.

2.7 EXISTING WORK ON THE SHAPE SYNTHESIS OF ANTENNAS

As indicated in Section 1.1, traditional antenna design entails choosing some canonical radiator structure defined by a few key dimensions, and then adjusting these dimensions using an optimization algorithm that improves a performance-related objective function that is repeatedly evaluated via a computational electromagnetics (CEM) model of the structure. This approach has proved extremely effective in the development of wireless communications antenna technology to date, but it is limited in the sense that the "design space" is limited to a relatively small library of canonical or near-canonical shapes. As performance and placement requirements become more stringent, this approach to antenna design could eventually become an obstruction. As a result, unconventional antenna types have been developed that cleverly use the host platforms themselves, for example [DENG19]. The application of antenna shape synthesis, also known as inverse design or topology optimization in other fields, can expand the "design space", taking into account factors like occupancy and fabrication limits, platform presence, and much more.

The most widely-published antenna shape synthesis work uses what can be described as a discrete-pixelation approach. Some conductor starting shape is divided into pixels/segments as shown in Fig.2.6-1. The final shape is obtained by keeping or removing these pixels to maximize some objective function F_{obj} into which the design goals have been translated, in a manner dictated by some evolutionary optimization algorithm (e.g. GA). The most straightforward manner to define an F_{obj} in antenna work is to use some combination of the performance metrics such as those defined in Section 2.2. Reference [RAHM 99] is perhaps the seminal one on discrete-pixelation antenna shape synthesis. This approach has been used to shape synthesise low

directivity[34] microstrip antenna [JOHN 99a][JOHN 99b][THOR 05] bandwidth increases or miniaturization, for shaping conducting antennas for radiation efficiency maximization [LI 18], and wire antennas [YAMA 09]. All of these were for planar conducting structures. Fully three-dimensional shaping of thin-wire (as opposed to conducting surface) antennas is performed in [ALTS 02][LIND 99][CHOO 05], with some restrictions placed on the allowed occupied volume. These references all used the GA as the optimization method. [MIRH 16] used a binary particle swarm optimization algorithm, and [GOUD 17] binary differential evolution, in such discrete-pixelation based shaping, but for problems already satisfactorily tackled with the GA. Ways to accelerate discrete-pixelation based shaping of conducting antennas have been discussed in [CAPE 19].

Work has also been published on the discrete-pixelation shape synthesis of frequency selective surfaces (FSS) with specific passband or stopband performance in [OHIR 04], and for the shape synthesis of reflectarray elements in [AOKI 11][ETHI 14b]. In the latter reference, the elements are shaped in such a way that adjacent reflectarray elements, although not identical, can be selected to have a geometrical similarity that in the end endows the resulting reflectarray with improved aperture efficiency. The FSS and reflectarray work just referenced has been done for single-layer elements only. Also, the in-house CEM codes used in the above references did not rigorously accommodate substrate effects, and so the above references have fabricated the elements on very thin substrates that are bonded onto free-space foam. The use of shape synthesis for multi-layer transmitarray elements on realistic substrates has been reported in [ALJA 18][ALJA 21].

One alternative to the discrete-pixelisation approach, that we can call a continuous-pixelation method, exploits work that has been used in structural engineering. It has been used in the shape synthesis of conductiong antennas in order to be able to use gradient-based optimization algorithms (not possible with discrete-pixelation methods). This approach, in the electromagnetics realm, converts the variables defining the geometry from the binary ones (used in discrete-pixelation) into continuous ones using some so-called "material interpolation law" that can be quite complicated [NOMU 13][HASS 14][LIU 16][HASS 20] and is somewhat arbitrary. Furthermore, the

[34] The shaping of high-directivity reflector antenna surface geometries for directivity maximisation, or to provide contoured beams, has been done for many years [RAO 13, Vol.I] [RAHM 07], but is more appropriately classified as being feature optimization. It is at any rate not the type of antenna synthesis we have in mind in this thesis. The determination of the excitations of the elements in an array antenna consisting of discrete elements is an example of pattern synthesis, and not of shape synthesis.

disadvantage of doing this, is that the shaped antenna designs that arise unavoidably (and undesirably) consist of conducting regions whose conductivity values vary from one point to another. This is not what we want. Not only from a fabrication point of view but because we do not want designs with low-conductivity regions because this represents loss. Thus conducting regions of intermediate conductivity must be eliminated in some way, a process that is also somewhat arbitrary. This elimination has been attempted in a number of ways [JENS 11] [EREN 11] [HASS 20] but has been found to be problem-dependent.

Another route that does not use discrete-pixelisation is one using gradient based optimization to shape antennas whose geometry is defined in terms of splines [GRIF 06][TOIV 10][SALU 18] whose parameters are adjusted during the optimization process and so shapes the antenna, or uses neural network models of the geometry [NASE 21].

A discrete-pixelation method for the shape synthesis of single electrically-small antennas, in which the feed location need only be selected after the shaping has been performed, was first described in [ETHI 14a]. A related approach was later used in [YANG 19] for MIMO antennas, and has been termed a "shape-first, feed-next" approach by the latter authors. It relies on a characteristic mode analysis of the structure. This work applies to electrically small or intermediate-size antennas that are "single-mode" in the sense that only one characteristic mode completely describes the antenna's behaviour. If the antenna proper radiates in the presence of other objects (that need not be electrically small) the approach of [ETHI 14a] can still be used [ETHI 12], except that the sub-structure characteristic modes [ALRO 16] of the antenna proper (with the other objects in place) must be used. The shape-first feed-next approach has more recently been extended to fully 3D conducting surface antennas [ALAK 21]. Such shape-first feed-next shaping procedures extend the "design space" even further.

As far as this author is aware, the only shape synthesis work on DRAs (taken all the way to a specific complete antenna) has been that in [ALRO 20], which also adopted the "shape-first feed-next" route. However, the latter work did not consider the shaping of DRAs for directivity maximization or multiport-fed DRAs; the extension of the shape synthesis of DRAs to permit this (within the "shape-first feed-next" framework) is one of the goals of the present work.

2.8 CONCLUDING REMARKS

Some key conventional antenna performance requirements to which reference will be made in this thesis were defined/described in Section 2.2. The antenna type whose shape synthesis is the subject of this thesis, namely dielectric resonator antennas, was reviewed in Section 2.3, but only to the depth needed to place the work of the thesis in context. The way in which computational electromagnetics (CEM) will be used in the (driven and eigenvalue) analysis of the dielectric resonator antennas discussed in this thesis was discussed in Sections 2.4 and 2.5. On their own, such CEM methods do not permit shape synthesis of any kind. Optimization algorithms are also needed. These are classified, and in particular the GA broadly discussed in the conducting antenna shaping context, in Section 2.6. A review of the literature on existing shape synthesis methods for conducting antennas is the subject of Section 2.7. One conclusion that can be drawn from the literature that formed the basis of the known knowledge described in this chapter, is that no shape-first/feed-next synthesis procedures for the maximization of the directivity of multiport DRAs have been reported by others. This will be done here for the first time, in Chapters 4 and 5. Chapter 3, which follows next, develops the new shaping controller tool needed to achieve this, as well as various concepts and new mathematical expressions needed in the construction of this tool. Overall conclusions, the contributions of the thesis, and suggestions for possible future work, are the subject of Chapter 6.

CHAPTER 3: A SHAPE SYNTHESIS TOOL (AND ITS COMPONENTS) FOR DIELECTRIC RESONATOR ANTENNA

3.1 INTRODUCTORY REMARKS

In this chapter we describe a computational tool for the shape synthesis of multi-port dielectric resonator antennas (DRA) for maximization of **directivity-related performance metrics**; as far as we are aware this is the first time such a tool has become available.

A key aspect will be the ability to determine, for a given DRA shape, what (ideally) the largest attainable directivity is, without needing to specify the number and location of the feeding mechanisms. Sections 3.2 and 3.3 devise a way to do this through direct use of characteristic mode concepts.

Later in the thesis, shape synthesis will be performed for a beam-steerable antenna that, through scanning, must ensure coverage of some field of view according to a metric that quantifies such coverage in an average sense. This metric is defined in Section 3.4, and a means of calculating it provided.

In Section 3.5 we then proceed to a top-level[35] description of the shape synthesis procedure. This includes the selection of feed-mechanism locations (the antenna ports) and type in the post-shaping stage.

Current computational and fabrication limitations[36] that, at the time of the writing of this thesis, have acted as a barrier to wider implementation of shape synthesis procedure that are not inherent to the shape synthesis development, are discussed in Section 3.6.

Section 3.7 includes comments on the accuracy of the driven full-wave analysis to be used in the final designs, intended to establish confidence in the modelling.

Section 3.8 concludes the chapter.

[35] We use the term "top-level" because some details are specific to the objectives of particular shape syntheses, and will thus be described more thoroughly as needed in Chapters 4 and 5. This will be clarified in Section 3.5.
[36] We do not mean computational speed here, or access to computational facilities. A further footnote on this is given in Section 3.6.

3.2 DETERMINATION OF THE ATTAINABLE DIRECTIVITY IN TERMS OF CHARACTERISTIC MODE PROPERTIES - *QFA* METHOD[37]

If the CM modal weighting coefficients (α_n) of a radiating structure are known, then the far-zone radiated field[38] is

$$\bar{E}(\theta,\phi) = \sum_{n=1}^{\infty} \alpha_n \bar{E}_n(\theta,\phi) \tag{3.2-1}$$

where $\bar{E}_n(\theta,\phi)$ is the far-zone field of the n-th CM. Use of (2.2-8) and (2.2-9) thus allows the total radiated power to be written in terms of CM fields as

$$\begin{aligned} P_{\text{rad}} &= \frac{1}{2\eta_o} \int_0^{2\pi} \int_0^{\pi} \left|\bar{E}(\theta,\phi)\right|^2 \sin\theta \; d\theta \, d\phi \\ &= \frac{1}{2\eta_o} \int_0^{2\pi} \int_0^{\pi} \bar{E}(\theta,\phi) \cdot \bar{E}^*(\theta,\phi) \sin\theta \; d\theta \, d\phi \\ &= \frac{1}{2\eta_o} \int_0^{2\pi} \int_0^{\pi} \left(\sum_{n=1}^{\infty} \alpha_n \bar{E}_n(\theta,\phi) \right) \cdot \left(\sum_{m=1}^{\infty} \alpha_m \bar{E}_m(\theta,\phi) \right)^* \sin\theta \; d\theta \, d\phi \end{aligned} \tag{3.2-2}$$

The orthogonality property of the far-zone CM fields requires that[39] [HARR 72]

$$\frac{1}{2\eta_o} \int_0^{2\pi} \int_0^{\pi} \bar{E}_m(\theta,\phi) \cdot \bar{E}_n^*(\theta,\phi) \sin\theta \; d\theta \, d\phi = \delta_{mn} \tag{3.2-3}$$

If we multiply the two summations in equation (3.2-2) term by term, and enforce the orthogonality condition (3.2-3), we find that

$$\int_0^{2\pi} \int_0^{\pi} \left(\sum_{n=1}^{\infty} \alpha_n \bar{E}_n(\theta,\phi) \right) \left(\sum_{m=1}^{\infty} \alpha_m \bar{E}_m(\theta,\phi) \right)^* \sin\theta \; d\theta \, d\phi = 2\eta_o \sum_{n=1}^{\infty} \left|\alpha_n\right|^2 \tag{3.2-4}$$

---

[37] Use is made here of certain results related to the maximization of two quadratic forms (to be defined shortly). We will for convenience therefore refer to this as the quadratic form approach (QFA) of determining the maximum directivity. The reason for the qualifier "attainable" in the heading will be elaborated on in Section 3.3.

[38] In the case of DRAs, this is true as long as the impressed source feeding the DRA lies on or in the DRA material; otherwise (3.2-1) represents the scattered field only.

[39] It is important to remember that expression (3-3) involves the **integrated** dot product of the CM far-zone fields.

and hence expression (3.2-2) becomes

$$P_{rad} = \sum_{n=1}^{\infty} |\alpha_n|^2 \tag{3.2-5}$$

If (3.2-1) and (3.2-5) are inserted into (2.2-10) the expression for the total directivity[40] of the radiator is given by[41]

$$D(\theta,\phi) = \frac{2\pi}{\eta_o} \frac{\left| \sum_{n=1}^{\infty} \alpha_n \bar{E}_n(\theta,\phi) \right|^2}{\sum_{n=1}^{\infty} |\alpha_n|^2} \tag{3.2-6}$$

If there are only N_{CM} of the CMs with significant modal weighting coefficients, then (3.2-6) reads

$$D(N_{CM},\theta,\phi) = \frac{2\pi}{\eta_o} \frac{\left| \sum_{n=1}^{N_{CM}} \alpha_n \bar{E}_n(\theta,\phi) \right|^2}{\sum_{n=1}^{\infty} |\alpha_n|^2} \tag{3.2-7}$$

The partial directivity $D_p(\theta,\phi)$, with respect to some particular polarization $\hat{p}$ can similarly be written

$$D_p(N_{CM},\theta,\phi) = \frac{2\pi}{\eta_o} \frac{\left| \sum_{n=1}^{N_{CM}} \alpha_n \bar{E}(\theta,\phi) \cdot \hat{p} \right|^2}{\sum_{n=1}^{\infty} |\alpha_n|^2} \tag{3.2-8}$$

with $\hat{p} = \hat{\theta}$ or $\hat{p} = \hat{\phi}$, for example. In the shape synthesis process we wish to determine what set of modal weighting coefficients[42] $[\mathcal{W}] = \left[\alpha_1 \quad \alpha_2 \quad \cdot \quad \cdot \quad \alpha_{N_{CM}} \right]^T$ will give us the largest directivity. In order to do this, we use the procedure described in [CHEN 71] to determine the

[40] As opposed to partial directivity.

[41] The absence of a subscript on the directivity symbol will **always** mean we are referring to the total directivity.

[42] Symbol $[\mathcal{W}]$ will represent a different quantity than symbol $[W]$. Quantity $[\mathcal{W}]$ is a column vector of modal weighting coefficients, as indicated. Quantity $[W] = \left[w_1, w_2, ..., w_{N_p} \right]^T$ will represent a column vector of port weights, with N_p the number of ports. The latter weights, and what we mean by a port in the present context, will be defined in Section 3.5.2.

excitations needed to obtain maximum directivity for arrays of discrete (conducting) antenna elements. The difference here is that, instead of a set of discrete elements, we have a set of CMs with different modal weighting coefficients. Paralleling [CHEN 71], and using some algebra, we can write expression (3.2-8) as the ratio of two quadratic forms[43]

$$D(N_{CM},\theta,\phi)=\frac{2\pi}{\eta_o}\frac{[\mathcal{W}]^H[\mathrm{A}(\theta,\phi)][\mathcal{W}]}{[\mathcal{W}]^H[\mathrm{B}][\mathcal{W}]} \qquad (3.2\text{-}9)$$

The excitation vector $[\mathcal{W}]=\begin{bmatrix}\alpha_1 & \alpha_2 & \cdot & \cdot & \alpha_{N_{CM}}\end{bmatrix}^T$ of modal weighting coefficients replaces the excitations of the discrete array elements used in [CHEN 71]. Due to the orthogonality properties of the CMs, $[B]$ is an $N_{CM}\times N_{CM}$ identity matrix $[B]=\mathrm{diag}\{1,1,...,1\}$. The elements of the $N_{CM}\times N_{CM}$ matrix $[A(\theta,\phi)]$ are, for direction (θ,ϕ), given in terms of the individual CM fields by $A_{mn}=\bar{E}_m^*(\theta,\phi)\cdot\bar{E}_n(\theta,\phi)$.

Next, once again paralleling [CHEN 71], but in our case using CMs, consider the eigenvalue problem (this is not the eigenproblem that supplies the CMs)

$$[\mathrm{A}(\theta_i,\phi_j)]\,[\mathcal{W}(\theta_i,\phi_j)]=\chi(\theta_i,\phi_j)\,[B][\mathcal{W}(\theta_i,\phi_j)] \qquad (3.2\text{-}10)$$

This matrix eigenvalue problem provides N_{CM} eigenvalues $\chi(\theta_i,\phi_j)$ for **each** direction (θ_i,ϕ_j); these are not the CM eigenvalues λ_n mentioned in Section 2.5.2. If, for specific direction (θ_i,ϕ_j), the largest eigenvalue is selected, then the eigenvector $[\mathcal{W}(\theta_i,\phi_j)]$ associated with this eigenvalue will, when inserted into (3-2-8), give[44] us the largest directivity $D^{\max}(N_{CM},\theta_i,\phi_j)$ possible in direction (θ_i,ϕ_j) for the dielectric structure shape with the given CM content.

Similar comments to those above can be made for the partial directivity $D_p(N_{CM},\theta,\phi)$, but with

$$A_{mn}=[\bar{E}_m^*(\theta,\phi)\cdot\hat{p}]\cdot[\bar{E}_n^*(\theta,\phi)\cdot\hat{p}]=E_{mp}^*(\theta,\phi)E_{np}(\theta,\phi) \qquad (3.2\text{-}11)$$

[43] Superscript "T" denotes the transpose operation, whereas "H" is the complex conjugate of the transpose.
[44] This is a known mathematical result related to the fact that we have expressed the quantity (directivity in our case) as the ratio of two quadratic forms.

Expression (3.2-6) confirms that there is in fact no theoretical limit to the directivity of **any** antenna [RIBL 48]. The number of CMs in (3.2-6) must be kept to a value that ensures the largest directivity we predict[45] is a "normal-directivity" and not a "super-directivity". The very high-order CMs are difficult to excite, and (fortunately) we will not wish to excite them; but then they should not be included when using the above-mentioned "largest directivity" estimates when performing shape synthesis. In other words, when we use expression (3.2-8) in the shape synthesis process to be described in Section 3.5 (and used in Chapters 4 and 5) we wish to avoid super-directivity, and some way of determining N_{CM} so as to ensure this must be found. This is described in the section that follows, after one additional comment.

The $[\mathcal{W}(\theta_i, \phi_j)]$ found using the QFA method just described could have been determined using any optimization algorithm that is able to maximize general multi-variable nonlinear functions, in this case the latter function being the expression for the directivity in (3.2-8). Before conceiving the QFA method, the author in fact did this using both a genetic algorithm and a gradient-based algorithm the Matlab Optimization Toolbox [MATLAB]. However, use of the QFA is more than three orders of magnitude faster, a few seconds compared to several minutes. As will be seen in Section 3.5, this "sub-optimization" needs to be performed several hundred times during each iteration of the shape synthesis process, and so the QFA method is a great advantage[46].

As mentioned above, this is an adaptation of a method used in [CHEN 71] in a different (albeit antenna) context. Such methods have been used by a number of other authors [LO 66][HANS 82][SANZ 71] as well, in order to determine the excitation of elements in a conventional array antenna subject to sidelobe level (SLL) constraints. Thus, we could adapt our CM-based QFA method to include SLL constraints, but this has not been done as it would probably only be of interest if electrically larger DRAs than those used here were to be utilized, so as to allow some degrees-of-freedom to be "spent" on SLL control.

[45] And which will be used in the shape synthesis applied in Chapters 4 and 5. What is meant by "normal-directivity" is discussed in Section 3.3.

[46] It has been said that 'as computers become more powerful, the efficiency of algorithms becomes more important, not less' [TREF 11].

3.3 DETERMINATION OF THE NUMBER (N_{CM}) OF CHARACTERSITIC MODES NECESSARY TO AVOID SUPER-DIRECTIVITY

Consider a DRA[47] that lies on an infinite groundplane, as shown in Fig.3.3-1. As noted previously, if we determine the CMs for this DRA, and use[48] different values of N_{CM} in (3.2-7), different largest possible directivity values would be obtained for the same DRA. If an infinite number of CMs is used, there will in fact be no theoretical limit to the directivity of any antenna. We propose a method to decide on the value of N_{CM} needed to ensure a "normal-directivity" is being computed.

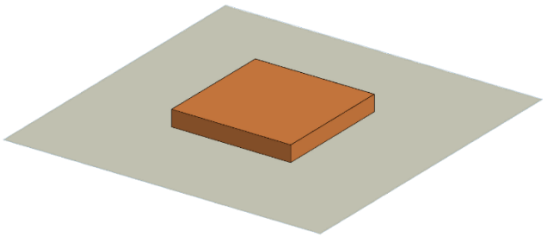

Figure 3.3-1: DRA on an infinite groundplane.

Harrington's work [HARR 58] on the maximum directivity of some material structure being used as an antenna maintains that the maximum 'normal-directivity' the structure can provide is

$$D_{\max}^{Harr} \approx (k_o a)^2 + 2k_o a \qquad (3.3\text{-}1)$$

where k_o is the free space wavenumber, and a is the radius of the smallest enclosing sphere of the antenna. This, of course, does not tell us in which direction this maximum directivity occurs, the shape of the antenna, or how to feed the structure to achieve it. Nevertheless, if we know a, then (3.3-1) gives us an estimate of the largest normal directivity possible.

In the case of a DRA located on an infinite groundplane, the radius a of the minimum sphere can be determined by using the geometry shown in Fig.3.3-2. Welzl's algorithm [WELZ 91] is used to compute the exact minimum bounding sphere radius given the coordinates of the DRA shape.

[47] This is not a shape synthesized DRA. It is merely being used here for explanatory purposes.
[48] We assume here that these could be correctly excited in some way, even though this may be difficult in practice.

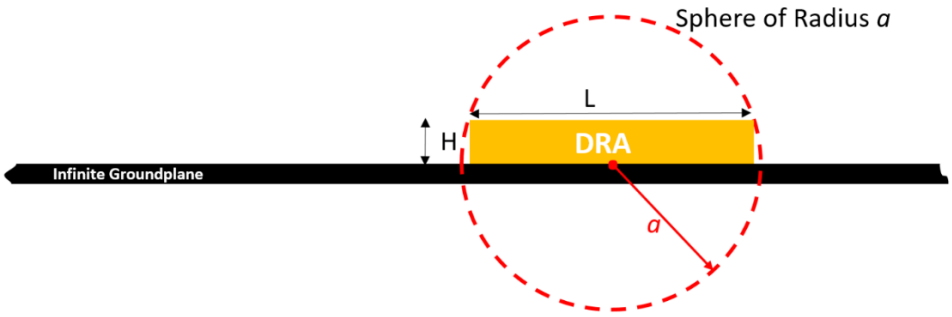

Figure 3.3-2: Geometry used in calculating the minimum enclosing sphere radius.

In order to illustrate the use of the limit in (3.3-1) a low value of N_{CM} (usually $N_{CM}=1$) will first be selected, namely a value which we know will not cause us to stray into a super-directivity situation. Then we evaluate $D^{\max}(N_{CM},\theta_i,\phi_j)$ in 'all directions' over the radiation sphere using the QFA approach and find the direction (θ,ϕ) in which it is largest, for the given N_{CM}. If $D^{\max}(N_{CM},\theta_i,\phi_j) < D_{\max}^{Harr}$ then we increase N_{CM} by one and repeat the above until we get $D^{\max}(N_{CM},\theta_i,\phi_j) \geq D_{\max}^{Harr}$. The previous value of N_{CM}, as shown in Fig.3.3-3 is the value that is used in computations during the shape synthesis process[49]. It will be necessary to calculate *a* for each different DRA shape that arises during such shaping, but this is possible because we know the coordinates of each 'block' in such DRA objects and hence are able to determine the minimum *a*. When too few CMs are considered, the full electromagnetic behavior of the structure is not properly captured, resulting in the observed negative $D^{\max}$ values.

The term "attainable" directivity was used in the heading of Section 3.2. By this we will always mean the largest directivity of some DRA shape in a given direction, attained with the modal weighting coefficient vector $[\mathcal{W}]$ of the CMs of the said shape obtained using the QFA method with an N_{CM} for the shape determined as described above. As will be noted in Section 3.5.2, this can be attained only if the actual feed mechanism is such that the $[\mathcal{W}]$ is exactly achieved, which

[49] In the QFA computations used in each step of the shaping process described in Section 3.5.

will not be precisely so in practice. We will us the symbol D_a to distinguish an attainable directivity from an actual directivity D.

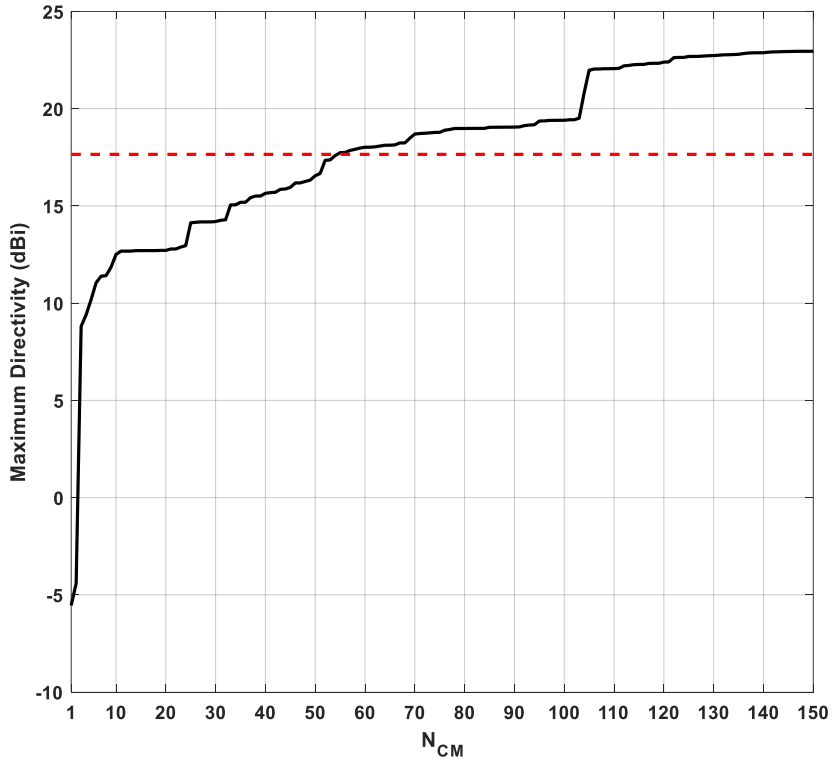

Figure 3.3-3: Maximum achievable directivity for different N_{CM} values. The dashed red line indicates the limit determined using expression (3.3-1).

3.4 QUANTIFYING THE SPHERICAL COVERAGE OF A STEERED-BEAM ANTENNA

As wireless systems begin to utilize higher frequencies (up to 90 GHz is already planned), the associated antennas will apparently need to have directional beams that can be steered [ZHAO 19]. Unusually, this is so for not only (macro and micro) base-station antennas but even for user equipment such as mobile devices. The purpose of scanning is to compensate for the increased "free space loss" at higher frequencies which necessitate the utilization of antennas with higher directivities. Higher directivities correspond to narrower beamwidths, requiring the ability to steer the beams effectively to achieve optimal communication performance. In a mobile wireless environment that is randomly changing, a large range of scanning angles is desired. This range of solid angles that the antenna on the user equipment is able to cover through scanning is referred to

as the **sphe5rical coverage** (say S_{cov}) of the antenna. According to the third-generation partnership project (3GPP), the spherical coverage of a system is characterized by the so-called cumulative distribution function (CDF) of the effective isotropic radiated power (EIRP) of the scanning antenna [ZHAO 19]. In Chapter 5, we will use shape synthesis for such a steered-beam DRA, and so need to know how to compute the above-mentioned CDF. Although this CDF has been defined, we have not found precise quantitative details there (or elsewhere) of how to compute this metric once we know the radiated fields of a given antenna for its multitude of scan-angle settings. This is therefore developed here.

We consider some steerable antenna, whose gain pattern is governed by some excitation vector set by a beamforming network (BFN). If we select any direction (θ,ϕ), this excitation vector can be adjusted to place as large a gain value in this direction as possible[50]. How high a gain value it is able to steer in this direction will be dependent on the level of complexity of the BFN[51]. In fact, it may not even be able to steer a pattern peak to all the directions over S_{cov}. It may have to be accepted that the gain in the direction is simply maximized, with the actual peak value of the steered gain pattern pointing in some other nearby direction. A means is required to determine whether the said steered beam antenna is nevertheless suitable, even though it is not able to perform "classical scanning".

The maximum gain values that the BFN is able to achieve in the set of directions (θ,ϕ) over the spherical coverage area S_{cov} can be described by the maximum gain function $G_{\text{steered}}(\theta,\phi)$. It should be noted that $G_{\text{steered}}(\theta,\phi)$ is **not** a gain pattern of any antenna, but represents the set of maximum gain values a particular antenna is able to achieve in each direction (θ,ϕ) through steering. We will for convenience refer to $G_{\text{steered}}(\theta,\phi)$ as the steered gain pattern.

[50] Each new excitation vector results in the antenna having a different radiation pattern. This is so for all electronically steered antennas.

[51] In an electronically scanned array antenna of some radar it must usually be possible to point the pattern peak with sufficient precision to all directions within the field-of-view of the radar, with a sufficiently high gain value in all such directions. For later convenience we will call this "classical" steering. In the wireless communications scenario, the complexity of the BFN of the antenna system on the user equipment may not have sufficient complexity to allow this. However, as long as the coverage, measured in the statistical sense to be described, is achieved, the wireless system requirements for reliable communication will be satisfied.

Using the EIRP definition from Section 2.2.5, the steered effective isotropically radiated power can similarly be defined by

$$\xi_{\text{steered}}(\theta,\phi) = P_{in}\, G_{\text{steered}}(\theta,\phi) \tag{3.4-1}$$

In theory, the range of ξ_{steered} values is $0 \le \xi_{\text{steered}} < \infty$. In practice we will have $\xi_{\text{steered}}^{\min} \le \xi_{\text{steered}} < \xi_{\text{steered}}^{\max}$, say. If $\mathcal{P}(\xi_{\text{steered}})$ is a properly defined probability density function for the steered effective isotropic radiated power, taken over all directions within S_{cov}, then the cumulative distribution function (CDF) of the EIRP can be defined as

$$CDF(\xi_{th}) = \int_{0}^{\xi_{th}} \mathcal{P}(\xi_{\text{steered}})\, d\xi_{\text{steered}} = \int_{\xi_{\text{steered}}^{\min}}^{\xi_{th}} \mathcal{P}(\xi_{\text{steered}})\, d\xi_{\text{steered}} \tag{3.4-2}$$

This gives the probability, when observing over all directions, that $\xi_{\text{steered}} < \xi_{th}$, quantity ξ_{th} typically representing some threshold value arising from the specifications of some wireless communication system.

In practice, in order to calculate the CDF, the steered effective isotropic radiated power is sampled in a finite number of directions (θ_s,ϕ_s), $s = 1, 2, ..., N_s$. In other words, we will have a set of samples $\xi_{\text{steered}}(\theta_s,\phi_s)$. The CDF of the EIRP is then approximated for any value of ξ_{th} by

$$CDF(\xi_{th}) \approx \frac{\text{No. of directions in which } \xi_{\text{steered}} < \xi_{th}}{N_s} \tag{3.4-3}$$

This gives the probability that the steered EIRP will be greater than ξ_{th}. Fig.3.4-1 shows important parameters on a typical plot of the CDF of the steered EIRP. Quantity $\xi_{\text{steered}}^{\min}$ represents the minimum EIRP value that the antenna system achieves when steered to directions over S_{cov}. Quantity $\xi_{\text{steered}}^{\max}$ represents the maximum EIRP value the antenna system can achieve when steered to directions over S_{cov}. They are a measure of the beam-steering capability of the antenna system of the user equipment. The ideal CDF curve would be a vertical straight line at $\xi_{\text{steered}}^{\max}$ and corresponds to "classical" steering. Quantity $\xi_{\text{steered}}^{0.5}$ will be used to denote the value larger than which the steered EIRP is over 50% of the coverage area (that is, a CDF of 50%). According to

3GPP requirements mobile handsets, for example, have to satisfy both a $\xi^{\max}_{\text{steered}}$ and $\xi^{0.5}_{\text{steered}}$ requirement. The difference $\xi^{diff}_{\text{steered}}$, between $\xi^{\max}_{\text{steered}}$ and $\xi^{0.5}_{\text{steered}}$, is important as it 'determines' the profile of the CDF curve.

We would have $\xi^{diff}_{\text{steered}} = 0$ for an antenna that is able to perform "classical" steering but this would typically not be practical for user equipment antennas due to limitations on the complexity of the BFN. The antenna system of the user equipment is said to be able to 'transmit stable power through a large scanning angle' when $\xi^{\max}_{\text{steered}}$ is high enough and $\xi^{diff}_{\text{steered}}$ small [ZHAO19].

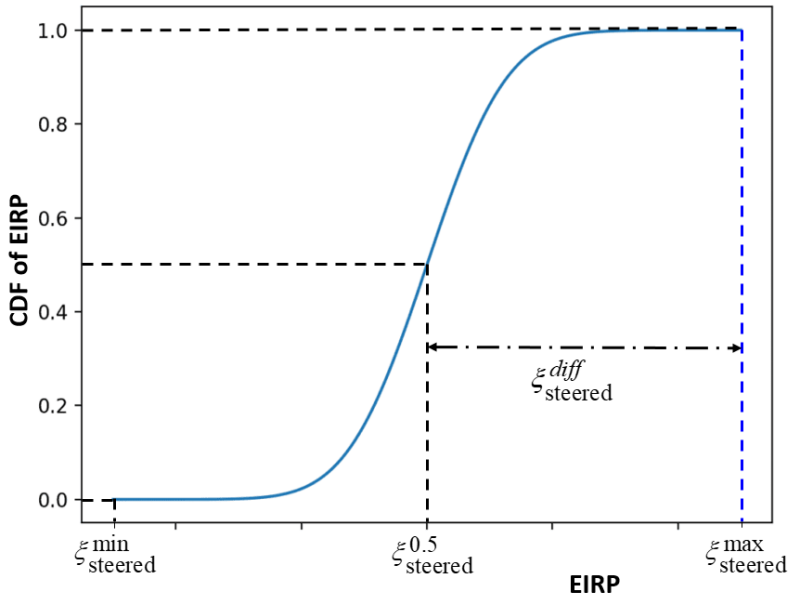

Figure 3.4-1: Illustrative curve of the CDF of the EIRP of some steered-beam antenna.

3.5 EXTENDED SHAPE SYNTHESIS PROCESS FOR MULTI-PORT DIELECTRIC RESONATOR ANTENNAS

3.5.1 Description of the Shape Synthesis Process

The flowchart in Fig.3.5-1 outlines the shape synthesis process. We have referred to this as an "extended" shape synthesis process in deference to the work in [ALRO 20]. Some aspects of the shaping procedure discussed in that reference are similar to that described here[52], but the whole process has been extended in the present work to more complex shape synthesis problems (e.g. directivity maximization, the use of multiple ports, and steered-beam applications).

[52] The principal author of [ALRO 20] is thanked for providing advice on the topic.

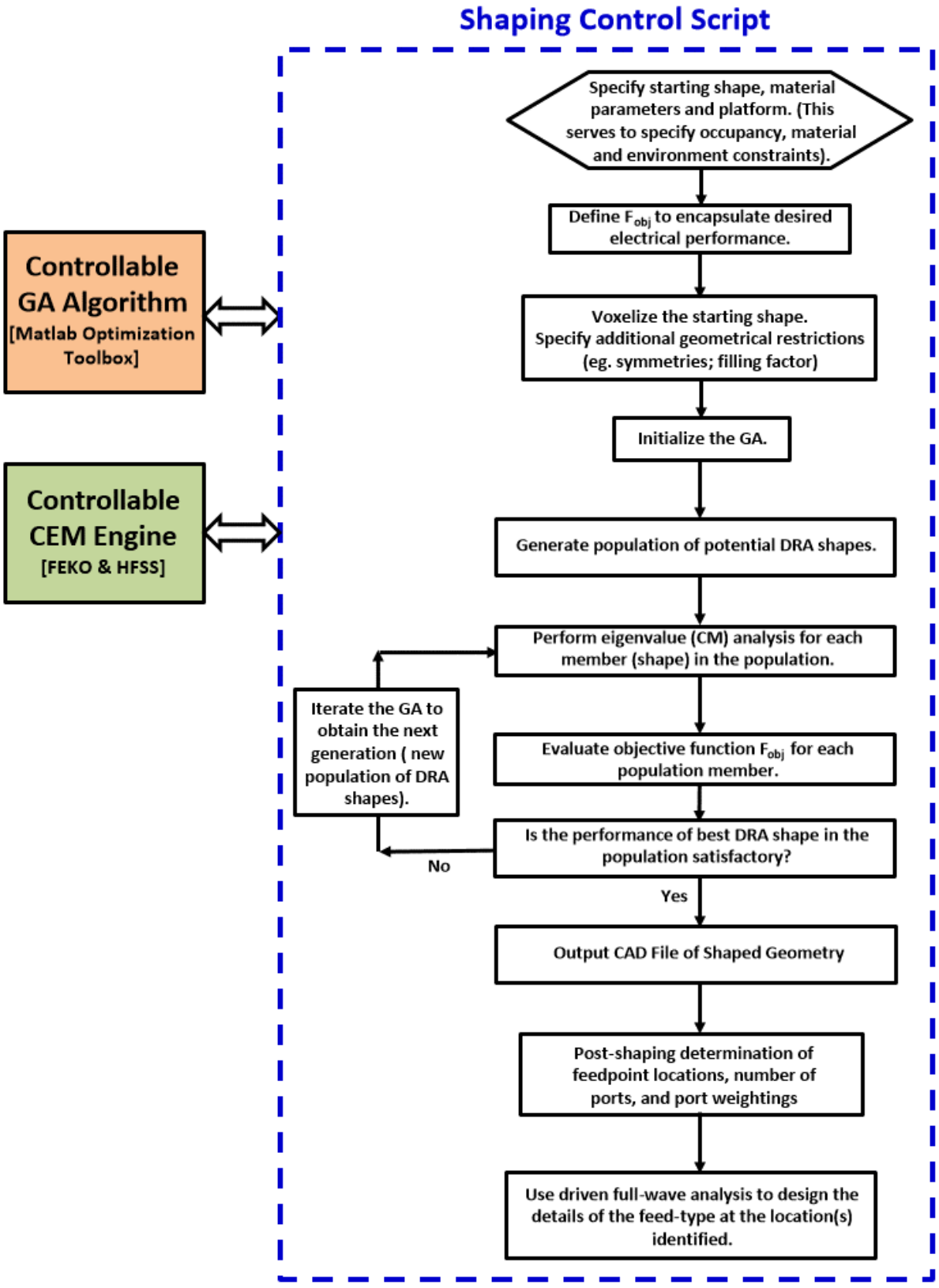

Figure 3.5-1: Flowchart of the extended shape synthesis process.

An unshaped piece of dielectric material is chosen as the starting shape. Its selection criteria would include the design constraints specific to the application, the space allowed on, the location permitted for, the antenna on the platform[53], and other considerations such as material cost that would dictate the value of the relative permittivity. The goal is to shape synthesize the dielectric object into a multiport dielectric resonator antenna (DRA) capable of providing some directivity-maximized pattern performance (either fixed-beam or steered-beam). The shaping procedure takes the dielectric "starting shape", and through automated three-dimensional geometry shaping arrives at a DRA that has some desired performance. The shape optimization proceeds without pre-determined feed-point location(s); this is possible because of the use of CMs in the shaping process. As the genetic algorithm (GA) used for the shaping proceeds, we at each iteration have a population of DRA shapes that must be ranked as to their suitability. In the present case these potential DRA shapes are ranked - in other words an objective function is evaluated for each - to favor the eventual goal of maximizing the fixed-beam directivity in some direction (Chapter 4), or to maximize the spherical coverage performance in the steered-beam case (Chapter 5).

We have used the code FEKO [ALTA 21] as the controllable engine for the full-wave electromagnetic simulation of the **eigenvalue** (CM determination) problem[54]. The **driven** full-wave problem[55] has been done using either code FEKO or HFSS [ANSY 21]. Thus, the latter codes are the "controllable CEM engine(s)" shown in the flowchart. There is an advantage in being able to use a commercially available code in that the shape synthesis can benefit from on-going upgrades[56] to such codes. FEKO in particular allows the user access[57] to geometry resource files that allow one to develop scripts that remove or replace the shaping blocks (defined in what follows), thus allowing the shaping tool to control the geometry of the DRA.

[53] Although we refer to a "platform" here, in this thesis we will only consider the shaping of DRAs located on an infinitely large planar groundplane. The reason for this is provided in Section 3.6. It will argue that, if the scope of the computational electromagnetics tool (as regards CM capabilities) were to become available, the work of this thesis would carry over seamlessly to the case of the shape synthesis of DRAs on a finite platform.
[54] Already mentioned in Section 2.5.
[55] Previously mentioned in Section 2.4.
[56] Some upgrades that would be highly desirable are mentioned in Section 3.6.
[57] This is not the case with all commercial CEM codes we have investigated. Such a capability is needed in order to implement the shape synthesis developed here.

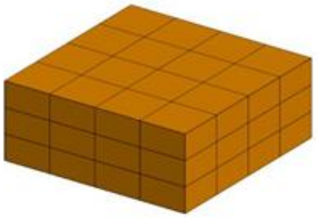

`[1,1,1,1,1,1,1,1,1,1,1,1,1,1,1,1,1,1,1,1,1,1,1,1,1,1,1,1,1,1,1,1,1,1,1,1,1,1,1,1,1,1,1,1,1,1,1,1]`

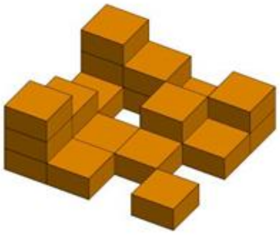

`[1,1,0,1,1,1,1,0,1,0,1,1,1,1,1,1,1,0,0,0,0,1,0,0,1,0,0,0,1,0,1,1,0,0,0,0,0,0,0,0,0,0,0,0,1,0,0,1]`

Figure 3.5-2: Starting shape (top) with all shaping blocks ("voxels") present, and (b). altered starting shape (bottom) with some shaping blocks removed by the shaping process. The two shapes are completely described by the binary variables ("chromosomes") shown below each shape.

We have implemented the procedure by developing a shaping control script in MATLAB that is able to communicate with FEKO resource files, as well as run the GA optimization algorithm also available commercially as part of the [MATLAB] optimization toolbox (thus supplying the "controllable GA algorithm" shown in the flowchart of Fig.3.5-1. The developed shaping script[58] dictates which parts of the starting geometry may be changed[59], what symmetries must be enforced, and what the filling factor[60] constraint there might be, during shaping. When the GA optimization algorithm has, from one iteration to the next, altered the geometry, the shaping control script makes

---

[58] The most burdensome computational steps have been parallelized. The computational experiments performed in this research have been done using the high performance computational (HPC) facilities made available as a grant from Compute Canada (now called the Digital Alliance of Canada) with the following features: Intel(R) Xeon(R) CPU E5-2683 v4 @ 2.10GHz, 2 physical CPUs with a total of 32 processors. A parallelized genetic algorithm (GA) is used in the main shaping procedure, with up to 12 shapes (and hence full-wave analyses) being processed in parallel.

[59] Portions of the starting shape may, for reasons that might arise in some specific design situation, be declared out of bounds to shaping.

[60] The filling factor can be used to ensure that a certain number of shaping blocks must be removed, in order for the final shaped DRA to have a mass lower than a specific value; there is of course always a price to pay in terms of performance.

it possible to send this information back to FEKO as a geometry file[61], along with specification of the frequency, mesh density and required CM output, have it generate a new mesh[62] and MM-matrix for an SIE analysis, and perform the CM full-wave analysis from which the objective functions, that allow the optimization algorithm to take its next decision, are evaluated. A different value of N_{CM} is determined for each shape to avoid super-directivity. The shaping control script permits the description of objective functions[63] as desired by the user directly in the said script. The objective functions are not simple functions; they perform considerable sorting of solutions during the shaping process, and all utilize the sub-procedures developed in Sections 3.2 and 3.3. We refer to such sorting operations as a particular "recipe" that is used by the shaping controller. The shaping controller script also monitors errors (e.g. signaling inaccurate CM computation if the MM mesh is not sufficiently dense) flagged by the CEM engine.

Shape synthesis permits one to enforce many constraints[64]. The selection of the starting shape already limits the physical space (which may be irregular) that the DRA may occupy and dictates the relative permittivity of the material to be used. One cannot predict ahead of time precisely what sort of requirements and scenarios might arise in future systems, and so flexibility in this regard is desirable. As an illustration of a further non-electrical constraint, we recall the filling factor mentioned earlier.

3.5.2 Feed Mechanism Location Selection & Detailed Specification

Once the shape of the DRA has been determined by the shape synthesis process, the CM solver outputs, for each CM, the distribution of the normal component of the electric field and tangential component of the magnetic field over the region directly below the DRA, namely $E_z^{(n)}(x, y, 0^+)$ and $H_x^{(n)}(x, y, 0^+)$ and $H_y^{(n)}(x, y, 0^+)$. This is used to determine the feed mechanism locations, in other words the locations of the ports at which the shaped DRA is actually excited. The advantage

[61] This step is performed through the running of a *Lua* script editor from MATLAB. *Lua* is a programming language embedded in the FEKO interface and available to FEKO users.

[62] This mesh is unrelated to the "building blocks" referred to above.

[63] As noted previously, the selection of an objective function is problem-dependent, and thus these will be discussed in Chapters 4 and 5, when the shaping control script is applied to specific DRA shape synthesis problems.

[64] Recall that the "optimum" shape is that which provides some desired performance **subject to the required constraints**, some of which may be non-electrical in nature.

of the post-shaping selection of these ports is this: The shaped DRA has the potential to supply the best attainable[65] directivity-related performance for an antenna subject to the constraints imposed by the size and material properties allowed for the starting shape, and its location on the platform. If the significant CMs could be excited with the required modal weighting coefficients $\{\alpha_n, n=1,2,....\}$ then this attainable directivity-related performance could be achieved. In practice this may require several ports that must be appropriately excited, in other words must be located and excitation-weighted so that the correct $\{\alpha_n, n=1,2,....\}$ pertain. However, there will usually be limitations on the number of physical ports a designer is willing to accommodate, and thus the actual directivity-related performance might fall short of the attainable one. The designer is able to take decisions by examining (for different numbers of ports) how close the actual performance is to the attainable performance, in the knowledge that the best design (subject to stated constraints) is being worked with.

The selection of the port locations depends on the type of feed mechanism desired by the designer (the user of the shape synthesis tool), such as coaxial probes, slots and so on. How this is done is best explained by example, and so will be considered in Chapters 4 and 5. Here we suppose we have $i=1,2,....,N_p$ ports whose locations $(x_i, y_i, 0)$ have been selected. If we terminate all ports except the *i*-th one, in the reference impedance, and excite the *i*-th port, we can compute the far-zone field $\bar{E}_i(\theta,\phi)$ using the driven full-wave model; note that this should not be confused with a CM field even though a similar notation is used. We are able to determine $\bar{E}_i(\theta,\phi)$ when each of the N_p ports is excited thus. If we were to now excite all the ports, each with a complex weight w_i, the total directivity[66] could be determined as

$$D(\theta_s,\phi_s)=\frac{2\pi}{\eta_o}\frac{\left|\sum_{i=1}^{N_p}\mathrm{w}_i\,\bar{E}_i(\theta_s,\phi_s)\right|^2}{P_{rad}}=\frac{2\pi}{\eta_o}\frac{\left|\sum_{i=1}^{N_p}\mathrm{w}_i\,\bar{E}_i(\theta_s,\phi_s)\right|^2}{\int_0^{2\pi}\int_0^{\pi}\left|\sum_{i=1}^{N_p}\mathrm{w}_i\,\bar{E}_i(\theta_s,\phi_s)\right|^2\sin\theta\;d\theta\,d\phi} \qquad (3.5\text{-}1)$$

[65] Recall that what we mean by "attainable" has been defined in Section 3.3.
[66] And similarly any partial directivity, *mutatis mutandi*.

Similar to what was done in Section 3.2 (but here, not using the CM fields), we can write the above expression in matrix form

$$D(\theta,\phi)=\frac{2\pi}{\eta_o}\frac{[\mathrm{W}]^H[\mathrm{A}(\theta,\phi)][\mathrm{W}]}{[\mathrm{W}]^H[\mathrm{B}][\mathrm{W}]} \tag{3.5-2}$$

The excitation[67] vector is $[W]=\begin{bmatrix}\mathrm{w}_1 & \mathrm{w}_2 & \cdot & \cdot & \mathrm{w}_{N_p}\end{bmatrix}^T$. The elements of the $N_p\times N_p$ matrix $[\mathrm{A}(\theta,\phi)]$ are, for direction (θ,ϕ), given by[68] $A_{ij}=\bar{E}_i^*(\theta,\phi)\cdot\bar{E}_j(\theta,\phi)$. The elements of $[\mathrm{B}]$ are given by[69]

$$\begin{aligned} b_{mn} &= \frac{1}{4\pi}\int_0^{2\pi}\int_0^{\pi}\bar{E}_m^*(\theta,\phi)\bar{E}_n(\theta,\phi)\sin\theta\; d\theta\, d\phi \\ &\approx \frac{1}{4\pi}\sum_{m=1}^{N_\phi}\sum_{n=1}^{N_\theta}\bar{E}_m^*(\theta,\phi)\bar{E}_n(\theta,\phi)\sin\theta_n\;\Delta\theta\,\Delta\phi \\ &= \frac{1}{4\pi}\sum_{m=1}^{N_\phi}\sum_{n=1}^{N_\theta}\left\{E_{m\theta}^*(\theta,\phi)E_{n\theta}(\theta,\phi)+E_{m\phi}^*(\theta,\phi)E_{n\phi}(\theta,\phi)\right\}\sin\theta_n\;\Delta\theta\,\Delta\phi \end{aligned} \tag{3.5-3}$$

with N_θ (N_ϕ) the number of samples taken along the $\theta-$direction ($\phi-$direction), respectively. The QFA procedure, using $[\mathrm{A}(\theta,\phi)]$ and $[\mathrm{B}]$ as defined immediately above (and not as was done in Section 3.2), can now be used to find the port weight vector $[W]$ that maximizes $D(\theta,\phi)$. In (3.5-3) we use $N_\theta=19$ and $N_\phi=37$, so that $\Delta\theta=5^\circ$ and $\Delta\phi=10^\circ$; these were checked to ensure that smaller angle increments were not needed, and by using the (more lengthy) approach but accurate spherical-wave-expansion based expression in [DICH 97].

The above QFA-based approach inherently assumes that the elements of $[W]$ are such that $0\le|\mathrm{w}_i|\le 1$ and $0^\circ\le\angle\mathrm{w}_i<360^\circ$. This is acceptable in the case of a fixed-beam antenna. In the case of a steered-beam antenna, that requires electronically adjustable phase shifters, it is still true

[67] Note that this is **not** the vector $[\mathcal{W}]$ of modal excitation coefficients defined in Section 3.2, but the weights some beamforming network would place on the antenna ports.

[68] At the risk of being repetitive, we remark once more that the far-zone fields here are **not** those of the CMs.

[69] [B] does not reduce to the identity matrix in this case, because the fields $\bar{E}_i(\theta,\phi)$ are not orthogonal over the sphere at infinity, unlike when they were the fields $\bar{E}_n(\theta,\phi)$ of the individual CMs.

in practice (at the time of the writing of this thesis) that a complete and continuous set of phase values $\angle w_i$ will usually not be available from any beamforming network (BFN). We should note that wireless applications are spurring the development of phase shifters at mm-wave frequencies (e.g. compact 6-bit phase shifter for 90 – 96 GHz in [DENG 22]), and that digital beamforming will eventually widen the set of phases that can be provided by a BFN. Nevertheless, in Chapter 5 we will, for comparison purposes, wish to find the $[W]$ subject to only a discrete set of phases being possible. This cannot be done using the rapid QFA approach, but can be done using numerical optimization via the GA used in a so-called mixed-integer approach [DEEP 09]. A mixed-integer optimization problem is one where some of the degrees-of-freedom are constrained to be integer values, and the remainder are real. Although numerical optimization is much slower than the QFA approach, fortunately at this stage of the shape synthesis based design (the post-shaping stage) determination of the $[W^{(s)}]$, namely a $[W]$ for each of the $s = 1, 2, ..., N_s$ directions, needs only be done once[70] for each *s*, and for only N_p variables, with N_p a relatively small value (e.g. 4, 6 or 8).

We describe the procedure in the case of $N_p = 4$, and a 6-bit phase shifter. For such a phase shifter the phases of the weights can only take on one of 64 values in the set $\{0^o, 5.6^o, 11.2^o, ..., 360^o\}$. This is mapped to the set of integers $\{1,2,3,.....,64\}$, as illustrated in Fig.3.5-3. The first four optimization variables $\{a_1,a_2,a_3,a_4\}$ represent the phases of the four weights, and each can only be an integer whose value lies between 1 to 64. The second four variables $\{a_5,a_6,a_7,a_8\}$ represent the magnitudes of the four weights, and can have any value between 0 and 1. The optimization procedure is as flowcharted in Fig.3.5-4.

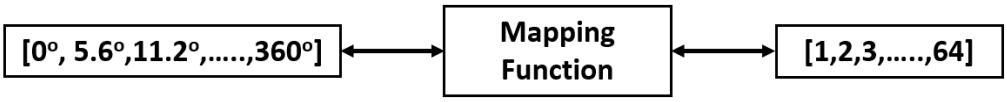

Figure 3.5-3: Mapping between actual phases of the weights, and their integer representation.

[70] Unlike the situation during shaping, where such an optimization is needed hundreds of times, and so the speed of the QFA is crucial.

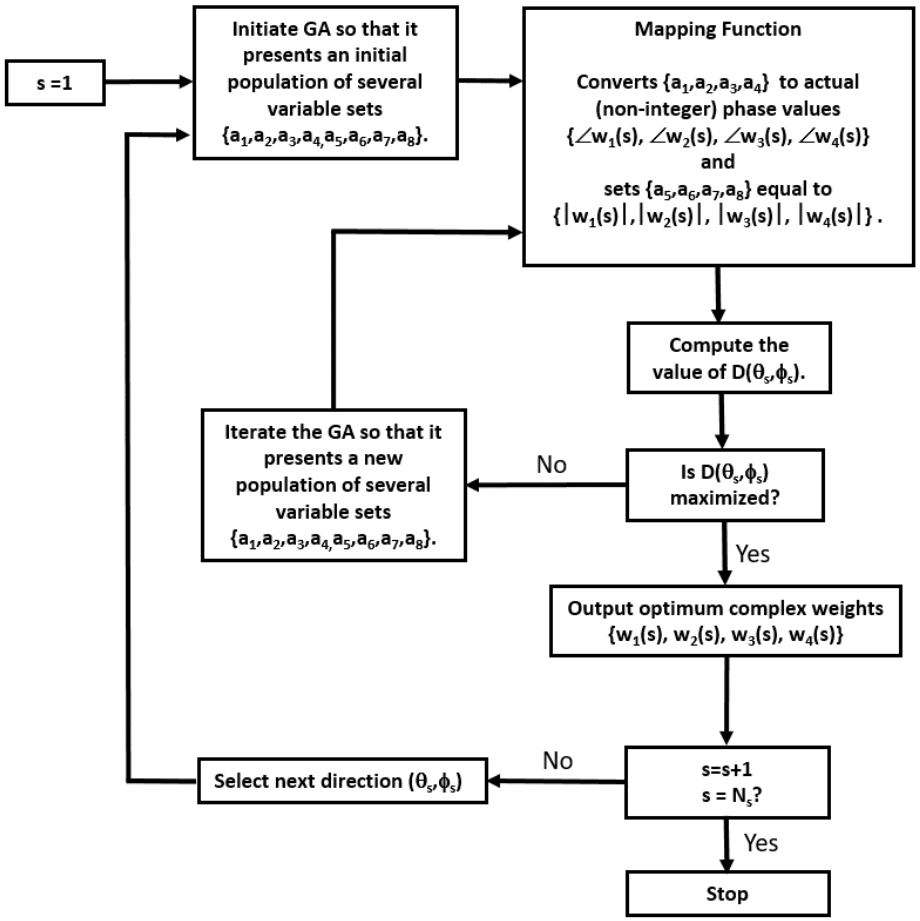

Figure 3.5-4: Procedure for the post-shaping determination of the port weights for each of the N_s directions in the case of a 6-bit phase shifter.

3.6 LIMITATIONS DICTATED BY CURRENT COMPUTATIONAL CAPABILITIES[71] AND FABRICATION METHODS

"A bad workman always blames his tools".

13th century English proverb.

3.6.1 Preliminary Remarks

It has been said that research should always be forward-looking, and should be done with the anticipation that the range of capabilities of computational tools and fabrication facilities will steadily improve. In what follows, we attempt to elaborate on how the present state of the specific computational tools needed, limit what is possible right now. However, the DRA shaping processes developed in this thesis have been done in such a way that, when the predicted improvements described below occur in the future, the shaping processes will be applicable, with only minor changes, to an even wider range of problems than is possible at the present time. It is not a case of the situation identified in the proverb quoted above!

3.6.2 Tracking of the Characteristic Modes of Dielectric Objects

It is an enormous undertaking to develop codes for computational electromagnetics that can accommodate scattering objects of general shape. Thus, we have relied on the use of the commercial codes mentioned in Section 2.4, 2.5, and 3.5 as the CEM engines in the DRA shape synthesis tool developed in this thesis. In particular, the CEM engine FEKO has been used to perform CM analysis of the DRA shapes during the shaping process. One issue that arises whenever one uses CEM to find modes of any kind[72] (namely, one must solve a numerical eigenvalue problem) is the so-called tracking problem. In the CM context, whenever we specify a new frequency, and then compute the CM eigenvalues of the DRA object at this new frequency, we obtain a set of discrete eigenvalues at each frequency, as illustrated in Fig.3.6-1. The tracking problem is one of deciding "how to connect the dots" and form curves that represent the eigenvalues of the CMs over frequency. The problem is that such curves can cross each other; the curves for CM#*n* will not always be above that for CM#*m*. Thus, it is not always straightforward

[71] We do not here mean computational speed, but inherent limitations on the capabilities of existing versions of the commercial CEM engines.
[72] Not only CMs.

to link the CM mode numbering of the results from the previous and new frequency, and so forth. In the case of the CMs of PEC objects such tracking algorithms [CAPE 11][LUDI 14][RAIN 12] appear to be mature in the commercial CEM codes. However, this is not the case when it comes to the CMs of dielectric objects [ALRO 17]. This has limited the work here to selecting a centre-frequency and performing all shaping at this frequency. Correct tracking would allow the shape synthesis procedure to be used with the objective functions defined at several frequencies over a specified frequency band rather than a single centre-frequency. Improvements have only relatively recently been proposed in the research literature [GUST 22b].

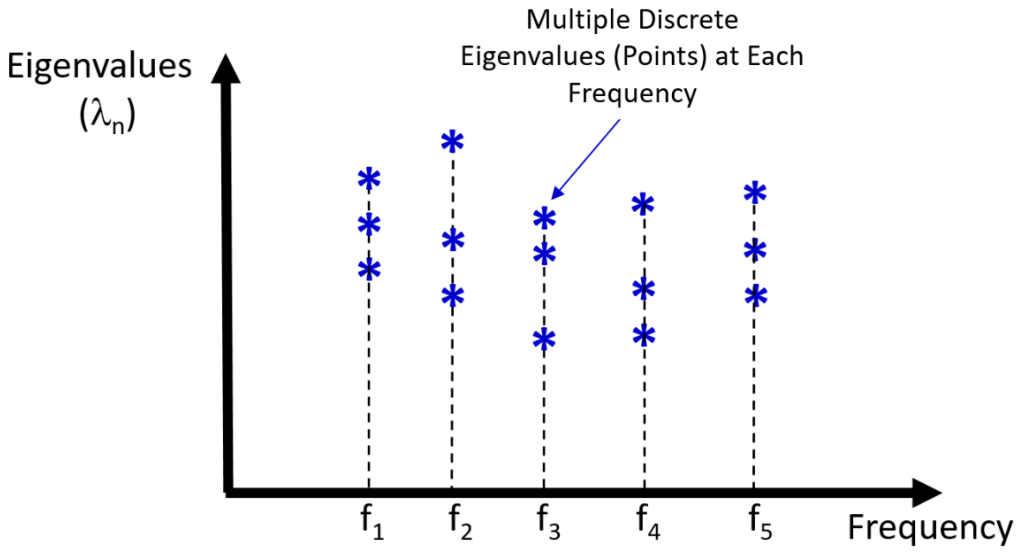

Figure 3.6-1: Discrete eigenvalues output by a numerical matrix eigenvalue solver.

3.6.3 Sub-Structure Characteristic Modes of Composite PEC/Dielectric Objects

Sub-structure CMs were described in Section 2.5.3. The ability to compute such CMs would allow the shaping process developed in this thesis to be used for DRAs on finite PEC groundplanes or even mode complex platforms, as depicted in Fig.3.6-2 and Fig.3.6-3, respectively. Unfortunately, no sub-structure computation ability is available with the commercial CEM codes. Thus, although we refer to a "platform" at various times in the thesis, we have only been able to use an infinite PEC groundplane in the thesis[73], as portrayed in Fig.3.6-4. Furthermore, a sub-

[73] This refers to the CM computation (the eigenvalue problem) only. This means that the finiteness of the "platform" cannot at present be accounted for during the shaping process. The driven problem model, used for determining the actual performance of the DRA, with its feed mechanisms, after shaping, does use a finite groundplane, as will be seen in Chapters 4 and 5.

structure CM capability that permits the computation of the sub-structure CMs of the dielectric object on a finite groundplane with a substrate (as depicted in Fig.3.6-5) would permit the shape synthesis of DRAs with proximity feed mechanisms as well, and not only those using probe or slot feeds[74].

Figure 3.6-2: Situation for CM computation for a dielectric object located on a finite groundplane.

Figure 3.6-3: Situation for CM computation for a dielectric object in the presence of another object, both located on a groundplane.

Figure 3.6-4: Situation for CM computation for a dielectric object located on an infinite groundplane.

Figure 3.6-5: Situation for CM computation for a dielectric object located on a substrate above a groundplane.

[74] Material losses can also not yet be included when performing CM (eigenvalue problem) analysis using the commercial CEM engines, and so loss minimization cannot yet be included as part of the shape synthesis process. Suggestions for doing so have only relatively recently been proposed in the research literature [GUST 22a][GUST 22b][KUOS 22], but have not yet found their way into commercial CEM engines. However, loss in the dielectric material can already be included in the driven problem analysis in commercial CEM engines.

3.6.4 Fabrication (3D Printing) of Dielectric Objects with Internal Voids, and Overhangs

One assumption made at the start of this work was that 3D printing had reached the point where any complex dielectric shape could be printed. However, using 3D printing materials[75] with relative permittivity values greater than 10, and with small loss tangents, it has not been possible to have objects with internal voids and overhangs (as are those in fact obtruded by the shaping process[76]) correctly printed. Several attempts by commercial 3D printing facilities failed to do this[77]. Indeed, it appears that for complex dielectric geometries "highly customized 3D printers(s)" with high temperature nozzles and heated beds are needed [HEHE 23]. As a consequence, it has (at the time of writing of this thesis) not yet been possible to fabricate the shape synthesized DRAs discussed in Chapters 4 and 5 due to their geometrical complexity. As an alternative, we had a dielectric object, that is of irregular shape, but has no voids or overhangs, fabricated using the preferred material. It is the object shown in Fig.3.6-6, and will be discussed in Section 3.7. Many geometries produced by the shape synthesis process contain so-called "non-manifold" geometrical features, of the type illustrated in Fig.3.6-7. In practice such tenuous connections between blocks of material would have to be thickened up prior to fabrication[78].

[75] Specifically being developed for RF applications.

[76] It would be relatively easy to forbid the presence of voids and overhangs in the shaping procedure, but this would stunt the directivity-maximized performance that is the goal of the shape synthesis.

[77] One suggestion was that a 3D printing machine is needed that is able to take the material to a higher temperature. It is not a fault of the material.

[78] For driven full-wave modelling, such non-manifold features also need to be "fixed" to enable the object surface to be correctly meshed so as to apply some CEM method. In the cases discussed in this thesis, the author had to fix these manually, as automated fixing is not yet available in even advanced commercial codes such as HFSS. We note that the software *Space Claim* (www.ansys.com/products/3d-design/ansys-spaceclaim), which is marketed by Ansys Inc. that also supplies HFSS, is not applicable for the issue just described.

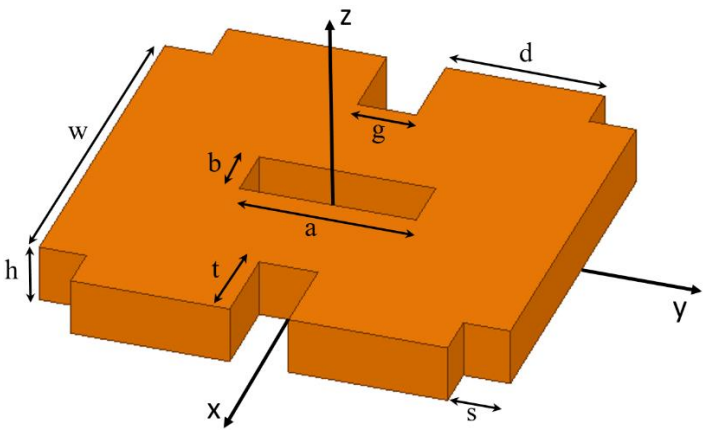

Figure 3.6-6: Irregular DRA used to provide experimental verification of the full-wave driven problem model used in this thesis. The dimensions are a = 30mm, b = 10mm, d = 27mm, h = 10mm, g = 10mm, w = 64mm, s = 8mm and t = 8mm.

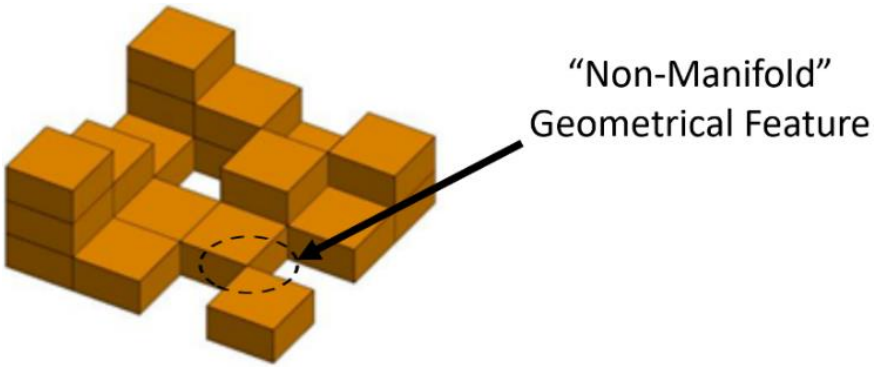

Figure 3.6-7: Shaped "DRA" showing non-manifold feature occurrence.

3.6.5 Inhomogeneous Dielectric Objects

We noted in Section 2.5 that the use of a volume-integral-equation (VIE) model of the DRA would allow one to shape synthesize inhomogeneous[79] DRAs. However, as it currently stands, the computational burden of existing VIE formulations prevents its use in shape synthesis even when high-performance computational facilities are available. Fortunately, research on computationally accelerating the VIE approach has recently been reported in the research literature [CHEN 19][PHIL 21]; it is probable that such improvements will be incorporated in commercial CEM codes over the next few years.

[79] Such DRAs have been shown to provide increased bandwidth.

3.7 EXPERIMENTAL VALIDATION OF THE DRIVEN COMPUTATIONAL ELECTROMAGNETICS MODEL OF MULTI-PORT DIELECTRIC RESONATOR ANTENNAS

For reasons noted in Section 3.6.4, the goal in this section is to validate the full-wave driven CEM model used, so that the shape synthesis outcomes of Chapter 4 and Chapter 5 can be accepted with confidence. The validation object in Fig.3.6-6 was fabricated using the preferred material[80], as shown in Fig.3.7-1; the imperfections (flaking) for even this relatively simple irregular shape can be seen. Four port locations were selected in a fairly arbitrary manner, albeit symmetrically positioned on the quadrantally symmetric geometry to aid in validating the computed results, as diagrammed in Fig.3.7-2 (a). At these locations, identical coax-fed feed probes, as individually sketched in Fig.3.7-2 (b), were inserted. The actual probes are shown in Fig.3.7-3. The complete structure (selected simply to have an irregular shape, and not designed to have specific antenna properties) was modelled, along with the coaxially-fed probes, as a driven full-wave problem using HFSS, with a finite-sized groundplane of dimension d = 150mm per side. As this is simply being done for validation purposes, the probe heights were not optimized in any way. The frequency range for the experimental validation work was selected so that, in light of the current fabrication difficulties mentioned in Section 3.6.4, we could fabricate a fairly (physically) large irregular object in the hope of easing the fabrication difficulties.

Fig.3.7-4 compares the computed and measured values of $|S_{11}|$. The two sets of results are similar; one reason for the differences is that the material appeared brittle during the drilling of the holes for the probes, as can be seen in Fig.3.7-1, and as a result the probes did not fit snugly into the validation shape.

Radiation pattern measurements were carried out in a far-field antenna test chamber using a mounting jig shown in Fig.3.7-5. The computed and measured far-field plots (in dB), purposefully showing different field components, pattern cuts, and frequencies, are those in Fig.3.7-6 and Fig.3.7-7. The agreement is acceptable (given the inevitable influence of the mounting jig and mis-alignments) for validation purposes, when compared to the type of comparisons typical of published DRA work reviewed in Section 2.3.

[80] Preperm® ABS1200, with $\varepsilon_r = 12$ and $\tan\delta = 0.0029$ [www.preperm.com]

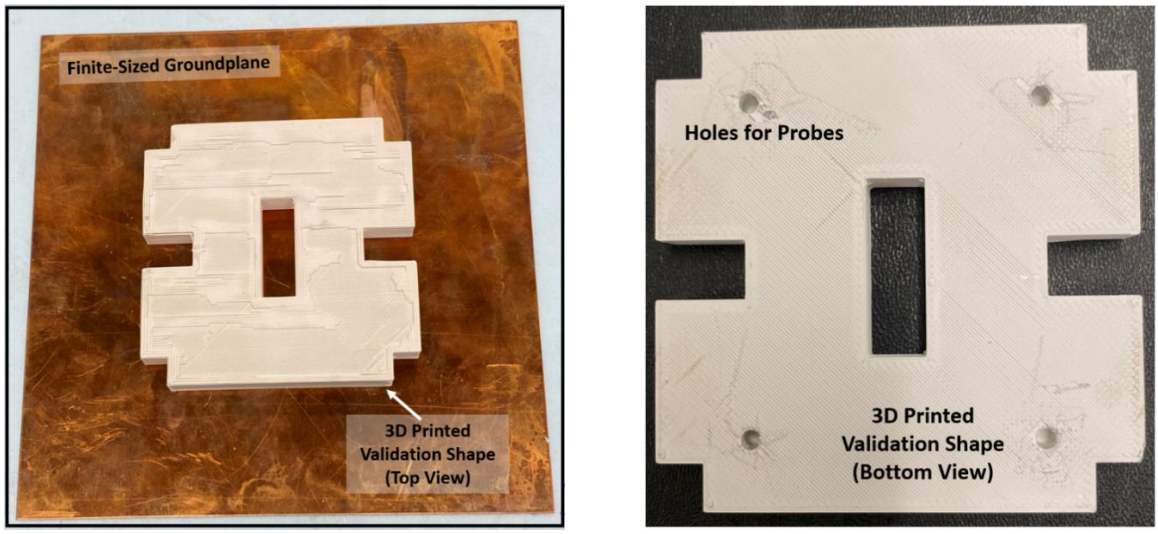

Figure 3.7-1: Fabricated irregular DRA shape top view on the finite-sized groundplane (left), and bottom view showing the holes for the four probes (right).

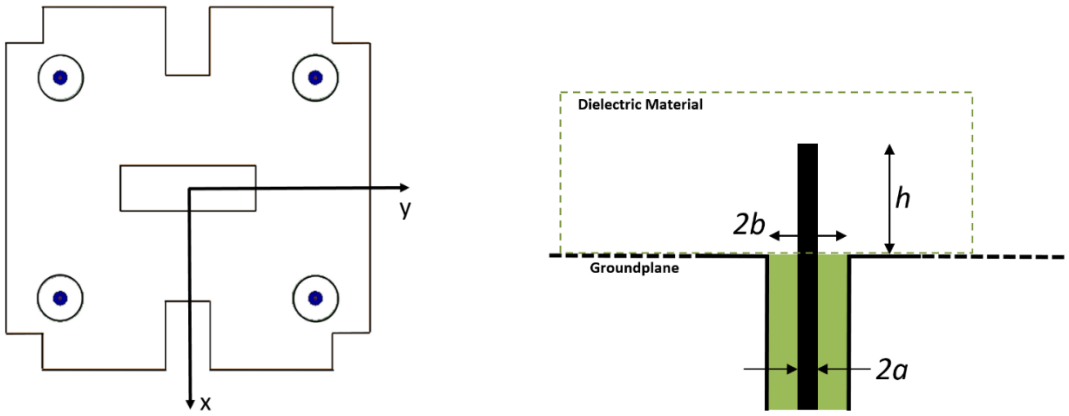

(a) **(b)**

Figure 3.7-2: (a). Feed port locations, and coaxial probe cross-sections (shown with correct relative scale) of the irregular DRA in Fig.3.7-1, and (b). Dimensions of the coaxial probes located at each of the ports : 2a = 3mm, 2b = 9.78mm and h = 6.14mm.

Figure 3.7-3: Top view of finite-sized groundplane (left), with DRA removed, showing the four probes, and bottom view (right) showing the four coaxial connectors.

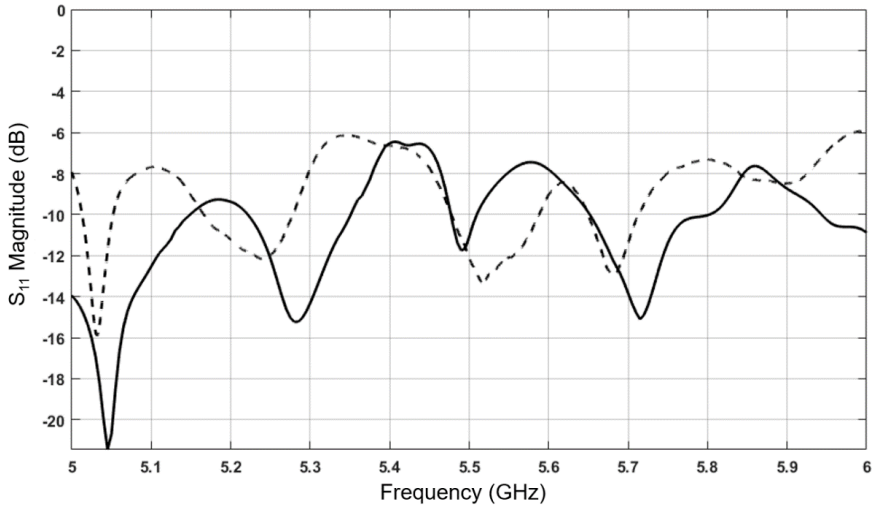

Figure 3.7-4: Comparison of the computed and measured magnitude of S_{11} of the DRA geometry in Fig.3.7-3, on a groundplane of dimensions *d* = 150mm per side, fed by four probes.

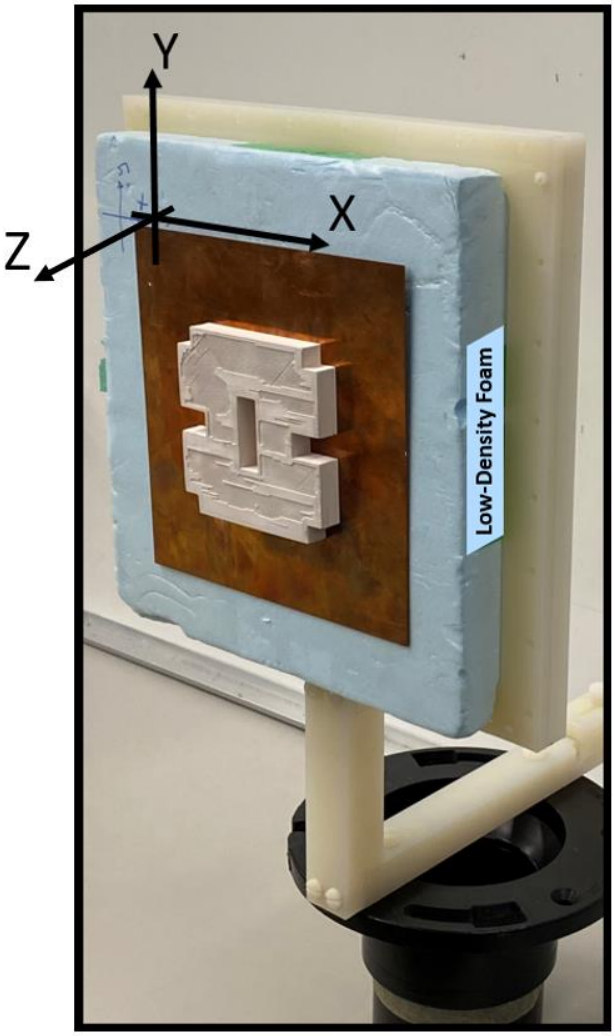

Figure 3.7-5: Photo of the four-probe-fed irregular DRA structure in the jig used to measure the far-zone fields in the far-field anechoic chamber.

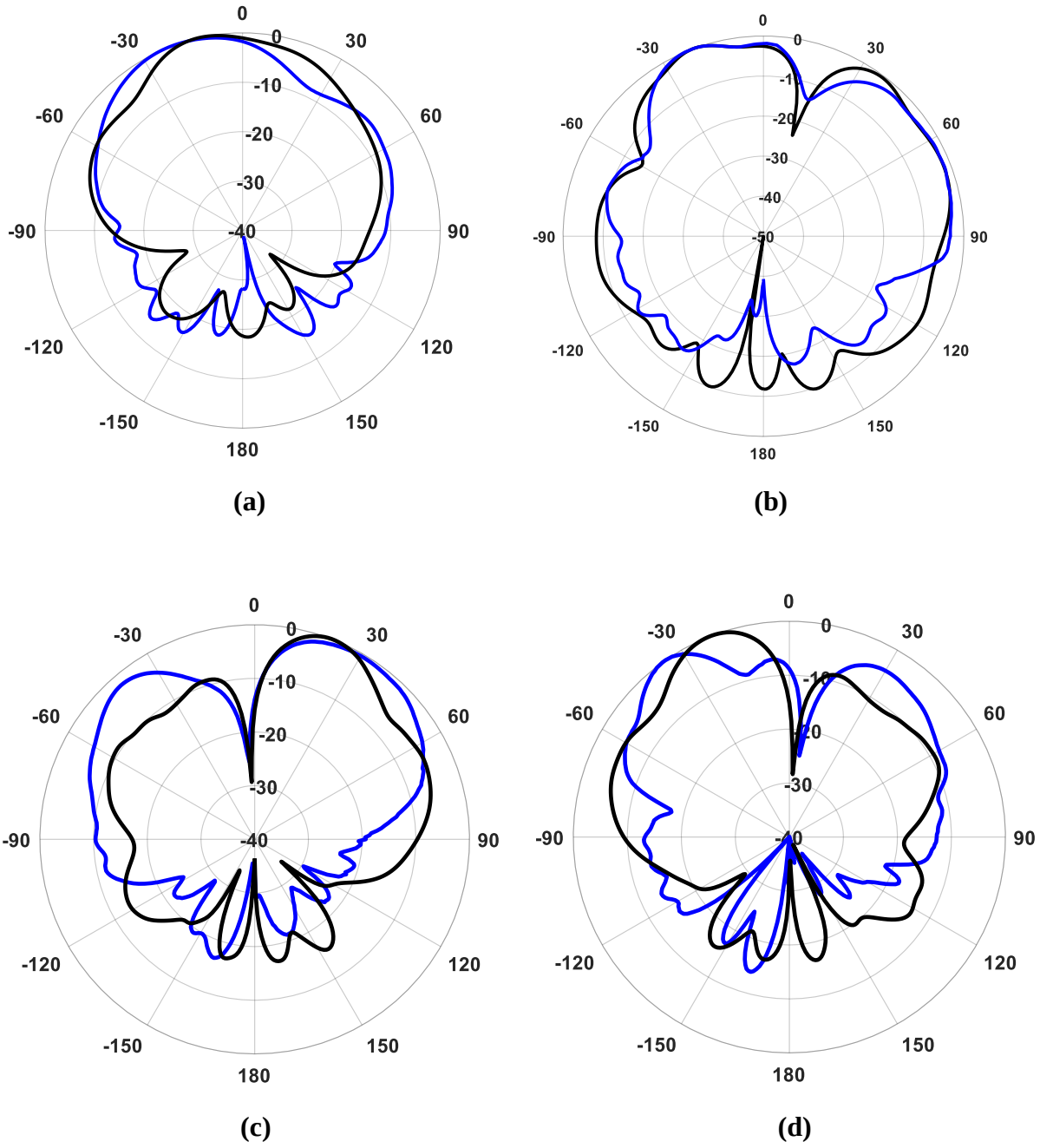

Figure 3.7-6: Computed (black line) and measured (blue line) normalized radiated field component magnitudes, showing (a). E_ϕ in xz-plane and (b). E_ϕ in yz-plane at 4.5 GHz, as well as (c). E_θ in xz-plane and (d) E_θ in yz-plane at 5.3 GHz.

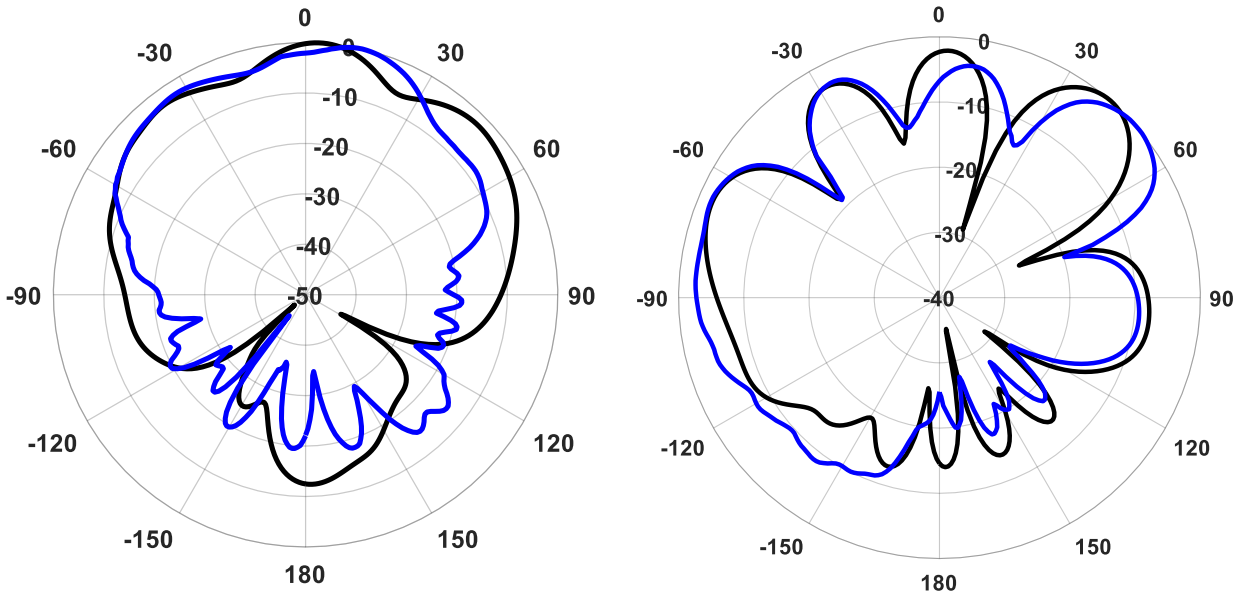

Figure 3.7-7: Computed (black line) and measured (blue line) normalized radiated field component magnitudes, showing (a). E_ϕ in xz-plane and (b). E_θ in xz-plane at 6 GHz.

3.8 CONCLUSIONS

In this chapter, we developed a computational tool for the shape synthesis of multi-port dielectric resonator antennas (DRA) for maximization of directivity-related performance metrics; as far as we are aware this is the first time such a tool has become available. In order to be able to perform such a shape synthesis without having to specify details of the feed mechanism(s) prior to shaping, the approach utilizes characteristic mode analysis. The quadratic form approach, along with a means of limiting the number of characteristic modes to ensure it is the "normal directivity" of the shape synthesized DRA that has been maximized (and super-directivity not misleadingly used), enables the shapes produced by the shaping controller at each iteration to be very rapidly performance-ranked without such feeding particulars. The shape synthesis procedure produces a DRA with the highest attainable directivity-related performance, the word "attainable" implying that it is an upper (non-super-directive) bound, that could be attained if a sufficiently complex feeding system were to be used. In practice there will be limits on the complexity of such feeding systems, but the computational approach permits one to determine where, and at how many points, to feed the shaped DRA, in the post-shaping phase. This allows one to examine the trade-offs of

the nearness to the attainable performance to the actual performance versus the feed system complexity. The shaping tool will next be used, with problem-specific objective functions defined in each case, to perform actual shape synthesis of DRAs in Chapters 4 and 5. Although, as stated in Chapter 1, the use of DRAs is intended for millimeter-wave frequencies, all the shape syntheses will be done at 6 GHz. The theorem of similitude [SINC 48] assures us that the shaped DRA can in principle be scaled for operation at higher frequencies.

CHAPTER 4: SHAPE SYNTHESIS OF MULTIPORT FIXED-BEAM DIELECTRIC RESONATOR ANTENNAS

4.1 INTRODUCTORY COMMENTS

Chapter 3 derived, constructed and implemented the extended shape synthesis procedure for directivity-optimized DRAs. The goal in this chapter is to use this implementation for the design of fixed-beam DRAs using shape synthesis. Section 4.2 considers the case of a DRA with a fixed broadside main lobe. We will utilize this case not only to validate the shape synthesis process, but also to demonstrate how the selection of feed ports can be done using information generated by this process, show how one or more feed mechanisms can be implemented, and to provide comments of a general nature on the shape synthesis components that can be easily understood from the outcomes of the procedure. Section 4.3 repeats these steps but for an off-broadside main lobe, and demonstrates the polarization control that is afforded by the shape synthesis route to the design of DRAs. Concluding remarks are given in Section 4.4.

4.2 SHAPE SYNTHESIS OF A DRA FOR MAXIMUM BROADSIDE DIRECTIVITY

4.2.1 Preliminary Comments

In order to have a theme, the starting shapes of all the examples of the application of the shaping script have been selected so that they fit the low-profile criterion of Section 2.5. Since the shaping does not add material to the starting shape (it only removes material) the resulting shaped DRA will be too. Thus we are shape synthesizing low-profile enhanced-directivity DRAs. We have furthermore attempted to present a consistent set of examples that serve to highlight the steps in the shaping process, sifted out from a much larger set that was used in refining the shaping procedure. We begin with the case of a fixed-beam maximum broadside directivity DRA, in the present section. Considerable detail will be provided since this will help to elucidate the shaping procedure described in broader terms in Section 3.5. Later examples can then be offered with less detail.

4.2.2 Construction of a Suitable Objective Function

The goal is to achieve as high a directivity as we are able using a given dielectric object size (starting shape) and relative permittivity value. It would thus seem logical that the objective function in question be defined in an obvious way in terms of attainable directivity as[81]

$$F_{obj} = D(N_{CM}, \theta_s, \phi_s)\big|_{\theta_s=0^\circ, \phi_s=0^\circ} = D(N_{CM}, 0, 0) \tag{4.2-1}$$

We know from comments in Section 2.5.2 that the lower order CMs are the ones most easily excited by actual feed mechanisms whereas those of higher-order are difficult to excite in practice. The problem with using (4.2-1) as the objective function is that it is able to exploit all N_{CM} modes[82], whereas we wish to penalize the higher-order CMs for the reasons just mentioned, yet at the same time including a sufficient number of CMs in the directivity expression for physical correctness. It was noted in Section 3.5.2 that once we have obtained a shaped DRA it is necessary to locate physical feed mechanisms that will define the port locations of the actual antenna. We do not want to simply assume that, using a feed mechanism of limited complexity, it will be possible to correctly excite all N_{CM} of the CMs needed to be included for an accurate but non-super-directive electromagnetic description of the DRA radiation process. We want to have a radiating structure shape for which the lowest-order CMs of the structure are the principal contributors to the desired directivity performance. In order to ensure that such DRA shapes are favoured during shaping (thus offering additional "mode control"), we have devised a modified objective function. This is done by first defining an additional quantity

$$F_\alpha(N_{CM}, N_\alpha) = \frac{\sum_{n=1}^{N_\alpha} |\alpha_n|^2}{\sum_{n=1}^{N_{CM}} |\alpha_n|^2} \tag{4.2-2}$$

Quantity N_α is the number of lowest-order CMs that we wish to be dominant in achieving the desired directivity maximization. $F_\alpha(N_{CM}, N_\alpha)$ is the ratio of the power in the first N_α modes

[81] As noted in Section 2.6, it makes more sense to talk of maximization of F_{obj}, even though we minimize $-F_{obj}$.

[82] The quantity N_{CM} has been discussed in Section 3.3.

to the total radiated power, with $0 < F_\alpha \leq 1$. A DRA shape with more power in the lower-order CMs will thus have a larger value of $F_\alpha(N_{CM}, N_\alpha)$. The objective function is therefore defined as

$$F_{obj} = F_\alpha(N_{CM}, N_\alpha)\, D(N_{CM}, \theta_s, \phi_s)\big|_{\theta_s=0^\circ, \phi_s=0^\circ} = F_\alpha(N_{CM}, N_\alpha)\, D(N_{CM}, 0, 0) \qquad (4.2\text{-}3)$$

We will demonstrate below that this indeed offers "mode control" while also trying to maximize the specified directivity. The objective function in (4.2-1) can be recovered by simply setting $N_\alpha = N_{CM}$.

4.2.3 Shaping Recipe

In the flowchart of Fig.3.5-1, one of the steps is "evaluate the objective function F_{obj} for each population member". In order to do this we require a set of CM weighting coefficients $[\mathcal{W}] = \begin{bmatrix} \alpha_1 & \alpha_2 & \cdot & \cdot & \alpha_{N_{CM}} \end{bmatrix}^T$. Thus for each shape in the current population we determine $[\mathcal{W}]$ via a sub-optimization using the QFA approach devised in Section 3.2, namely by maximizing attainable directivity

$$D(N_{CM}, \theta_s, \phi_s) = \frac{2\pi}{\eta_o} \frac{[\mathcal{W}]^H [\mathrm{A}(\theta_s, \phi_s)][\mathcal{W}]}{[\mathcal{W}]^H [\mathrm{B}][\mathcal{W}]} \qquad (4.2\text{-}4)$$

This $[\mathcal{W}]$ is used, for each different shape in the population, to evaluate F_{obj} for that particular shape.

4.2.4 Dielectric Block Starting Shape

The starting shape for this example is a rectangular dielectric block with a dielectric constant[83] of 12, and dimensions of $1.5\lambda_o \times 1.5\lambda_o \times 0.2\lambda_o$, where λ_o is the free space wavelength at 6 GHz. The starting shape dimensions set the volume constraints for the antenna design. As noted in Section 3.6.3, the dielectric block is located on an infinite groundplane. The goal, subject to these volume and material constraints, is to shape the dielectric block into a DRA with as high a total[84]

[83] The material corresponds to Preperm™ ABS1200 thermoplastic used in 3D printing.
[84] Cases involving partial directivity, illustrating polarization control, will be discussed in Section 4.3.

broadside directivity, in other words the $(\theta_s, \phi_s) = (0^\circ, 0^\circ)$ direction, at 6 GHz as possible. The feed-ports must eventually also reside within the allotted space; this aspect is dealt with in Section 4.2.8.

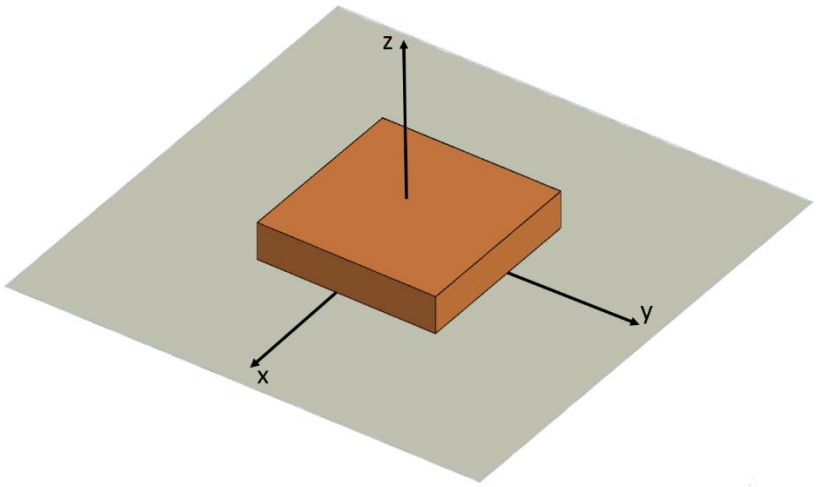

Figure 4.2-1: The starting rectangular DRA shape with dimensions $1.5\lambda_o \times 1.5\lambda_o \times 0.2\lambda_o$ at 6GHz.

In order to facilitate various comments later in this discussion we show, in Fig.4.2-2, the twenty most significant[85] CMs of the starting shape before any shape synthesis has been performed. We notice that the lowest-order CM that actually has its pattern maximum in the broadside direction is CM#12; we would prefer this to occur for a CM of lower order. Section 4.2.6 will demonstrate that the shape synthesis process allows us to do just that.

[85] Recall that by referring to these as the "most significant" we do not mean that these CMs are the ones that are able to most significantly contribute to achieving a high total directivity in the broadside direction. The "significance" of a CM has been defined in Section 2.5.2.

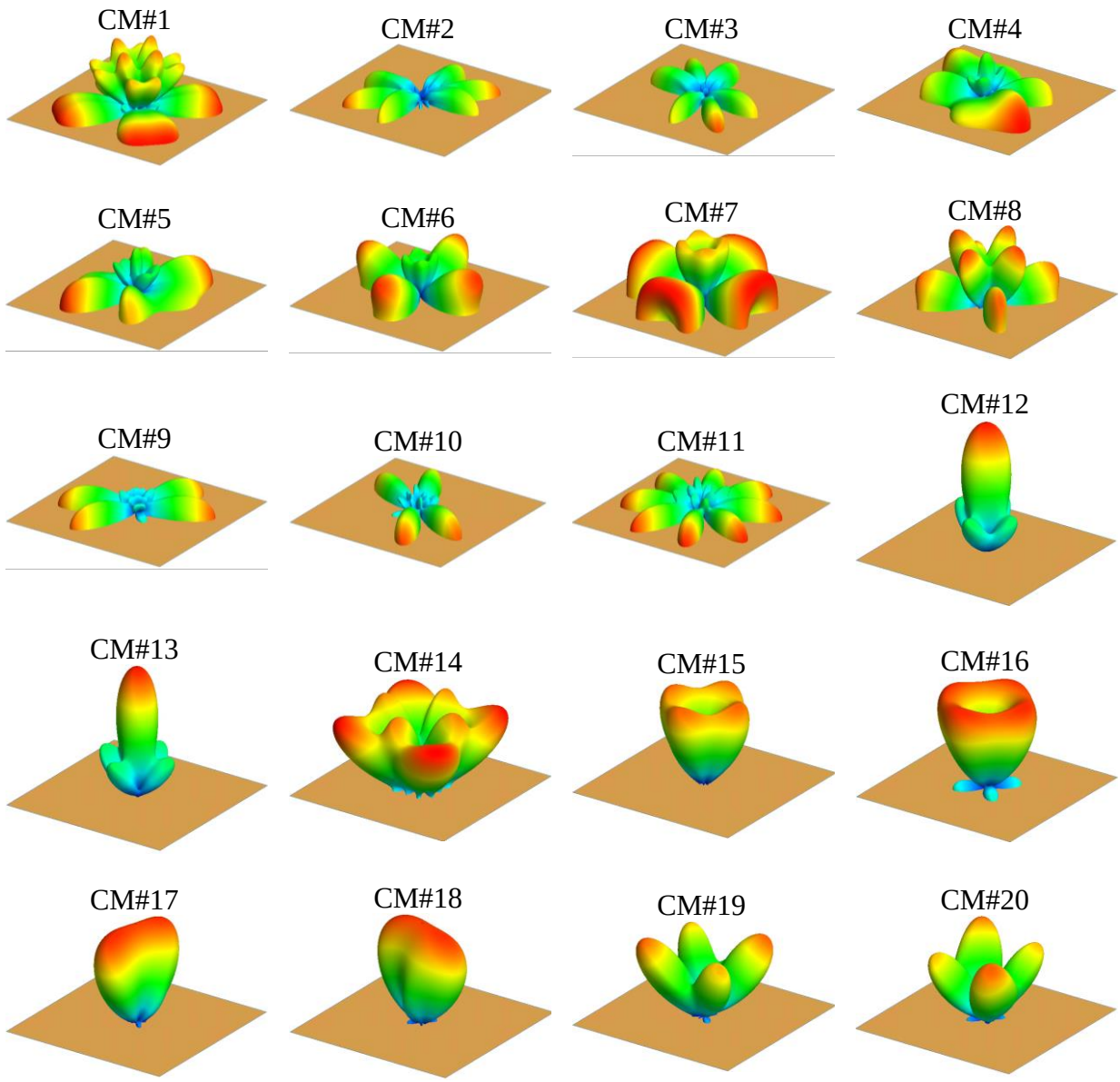

Figure 4.2-2: Computed total far-zone field patterns (at 6 GHz) of the 20 most significant CMs of the unshaped DRA starting shape shown in Fig.4.2-1.

4.2.5 Parameter Settings for the Shaping Process

The starting shape is shown again in Fig.4.2.3, divided into four quadrants, with quadrantal symmetry assumed[86]. This provides the bonus of reducing the number of degrees of freedom (DoF)

[86] There is little reason to expect that a DRA with optimized *broadside* directivity would not be quadrantally symmetric when the starting shape is a square (also quadrantally symmetric).

in the shaping process. Each quadrant consists of 100 smaller blocks, each smaller block having dimensions $0.15\lambda_o \times 0.15\lambda_o \times 0.05\lambda_o$. The number of smaller blocks determines the DoF (100 in this case) available to the GA[87] when performing its shaping operation.

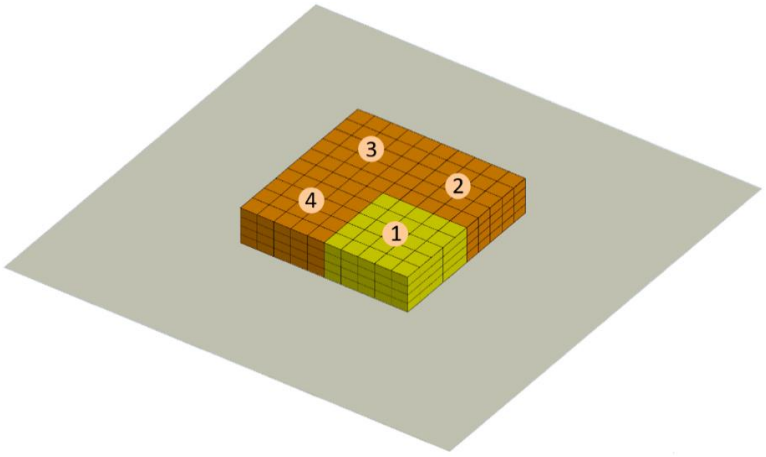

Figure 4.2-3: Starting shape divided into 100 smaller blocks of size $0.15\lambda_o \times 0.15\lambda_o \times 0.05\lambda_o$ on each of the four symmetrical quadrants (numbered 1 through 4). The light-coloured blocks are only intended to clarify the symmetry.

4.2.6 Shaping Outcome for the Case $N_\alpha = N_{CM}$

The initial shaping is done with $N_\alpha = N_{CM}$, and so there is little "restraint" on the CMs that can be utilized to contribute to the directivity maximization. The undesirable consequence is that the $|\alpha_n|$ are as shown[88] in Fig.4.2-4 (a). Several higher-order CMs would need to be relatively strongly excited to obtain the broadside directivity offered, which from Fig.4.2-5 is seen to be 14.6 dBi.

[87] The GA optimization options presented in Appendix I were selected based on numerous trial runs and observations of convergence success for the class of problem under study.

[88] The reader can ignore Fig.4.2-4 (b) at this stage.

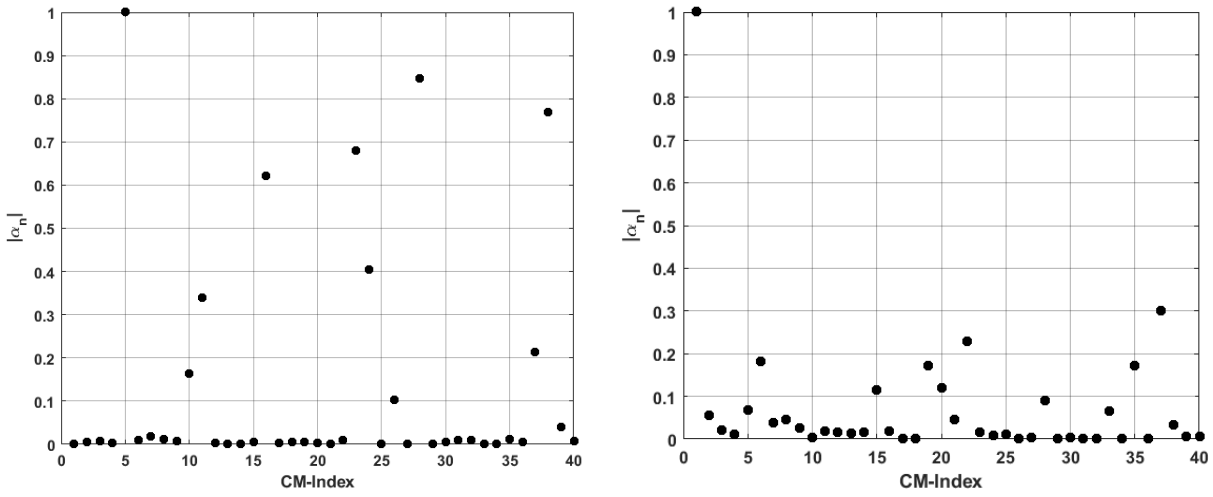

(a) **(b)**

Figure 4.2-4: Modal weighting coefficient magnitudes for achieving the attainable ideal available directivity (at 6 GHz) for DRAs shape synthesized (a). with all $N_\alpha = N_{CM} = 40$, and (b). with $N_\alpha = 1$.

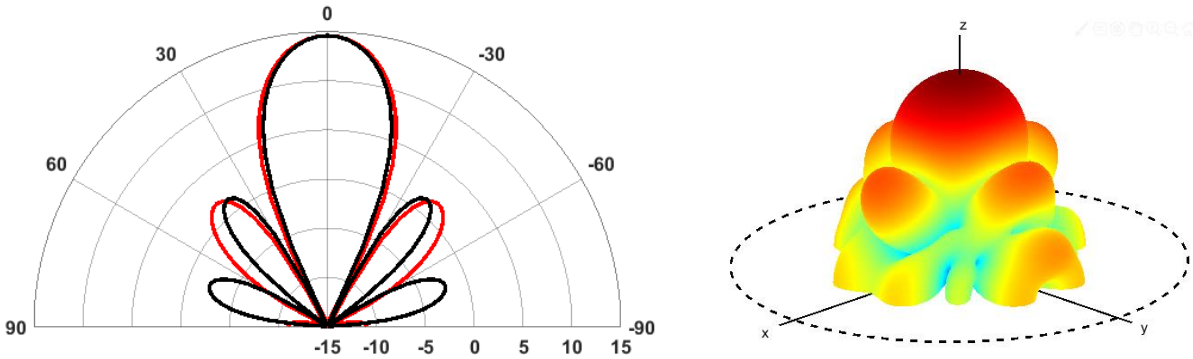

Figure 4.2-5: The plot on the left shows the attainable total directivity pattern (at 6 GHz), in the xz-plane (red curve), and the yz-plane (black curve), of the DRA shape synthesized with $N_\alpha = N_{CM}$. The broadside directivity is 14.60 dBi. The 3D plot of the directivity pattern is shown on the right.

We might question why, when[89] $D_{\max}^{Harr} = 17.65\,\text{dBi}$, we obtain $D^{\max}(N_{CM}, 0^\circ, 0^\circ) = 14.60\,\text{dBi}$. The answer can be found by referring to the sketch in Fig.3.3-2. The DRA starting shape does not fill the smallest-encompassing-sphere; if we were to use a starting shape that fills more of this

[89] The result shown in Fig.3.3-3 was in fact done for the starting shape used here (namely the same shape, dimensions, material permittivity, and frequency).

sphere[90] it might be possible to shape it to obtain a value closer to $D_{\max}^{Harr}$. Furthermore, although Harrington's expression provides the value of $D_{\max}^{Harr}$, this value is not necessarily reached for some specific desired direction (e.g. it can be in some non-broadside direction). The value of 17.65 dBi should be considered as an upper bound only, and not necessarily achievable. The value of 14.60dBi would be attainable, but only if we could perfectly excite the CMs with the modal weighting coefficients shown in Fig.4.2-4, which will typically not be possible without the use of a feeding mechanism that would likely be considered too complex for practical purposes[91]. More will be said about such considerations in what follows.

4.2.7 Shaping Outcome for the Case $N_\alpha = 1$

The shape synthesis procedure is then performed using $N_\alpha = 1$. In other words, we are demanding that the directivity be maximized in a way that results in the lowest CM contributes the most to the directivity achieved. Compared to what was allowed in Section 4.2.6, there is now much "restraint" on the CMs that can be utilized to contribute to the directivity maximization. The resultant shaped DRA is that in Fig.4.2-6. The desirable consequence is that the $|\alpha_n|$ are indeed now as shown in Fig.4.2-6 (b). The higher-order CMs now need to be less strongly excited to obtain the broadside directivity offered, that in this case is 13.66 dBi, as the attainable directivity plots in Figs.4.2-7 and 4.2-8 show. Our not wanting to allow the higher-order CMs to play a more significant role in the directivity maximization (for the good reasons mentioned earlier) has exacted the price of a 0.94 dBi decrease in the attainable directivity. This is precisely the reason that the shape synthesis process has been structured in the manner described in Chapter 3 – we want to know what the highest attainable directivity is (subject to the size and material constraints) and then wish to observe what the directivity-cost is of incorporating restraints that will allow us to realize such DRAs for different levels of feed mechanism complexity. We want the trade-offs to be transparent.

[90] But is not necessarily allowed by the occupancy constraints on the DRA to be designed using shape synthesis.
[91] We will thus not spend time discussing a feed mechanism for this particular shape synthesized DRA.

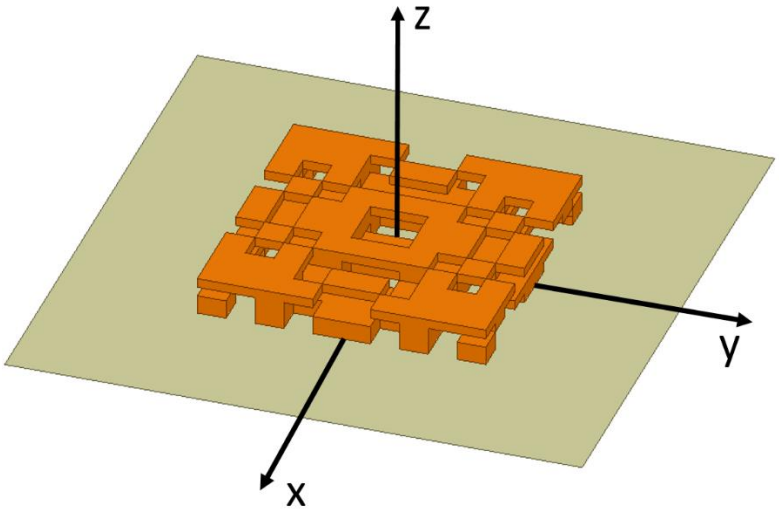

Figure 4.2-6: Geometry of the DRA shape synthesized with $N_\alpha = 1$.

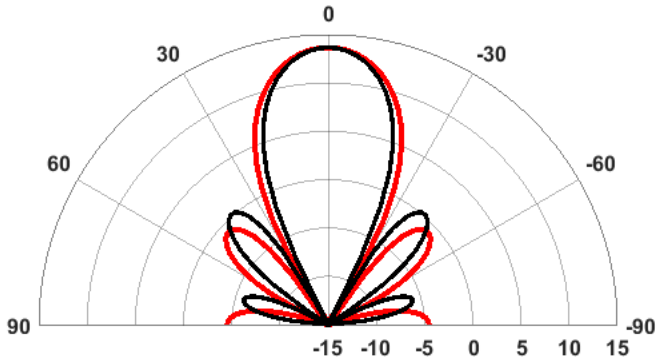

Figure 4.2-7: Attainable total directivity pattern (at 6 GHz), in the xz-plane (red curve), and the yz plane (black curve), of the shape synthesized DRA shown in Fig.4.2-6. The broadside directivity is 13.66 dBi.

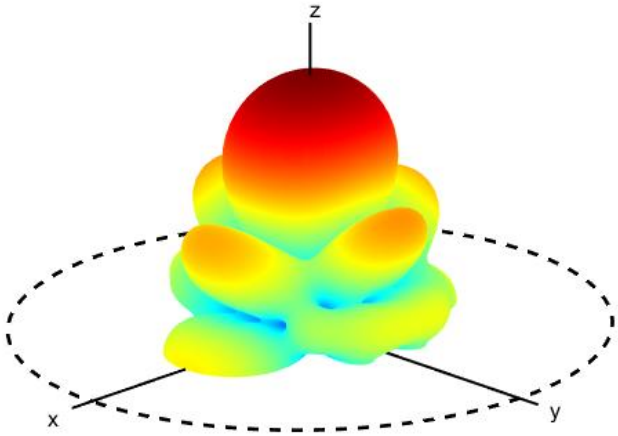

Figure 4.2-8: Total directivity 3D pattern representation (at 6 GHz) of the shape synthesized DRA shown in Fig.4.2-6. The broadside directivity is 13.66 dBi.

Before proceeding to the selection of the actual feeding ports of the shape synthesized DRA some comments on "mode control" are in order. Recall that the far-zone patterns of the CMs of the starting shape ("unshaped DRA") were shown in Fig.4.2-1. The five lowest CMs of the shaped DRA geometry in Fig.4.2-6 are shown in Fig.4.2-9. In contrast, the latter individually have broadside, or near-broadside, patterns whereas this is not the case for the unshaped DRA. The shape synthesis process has altered the CMs to "assist" it in maximizing the broadside directivity.

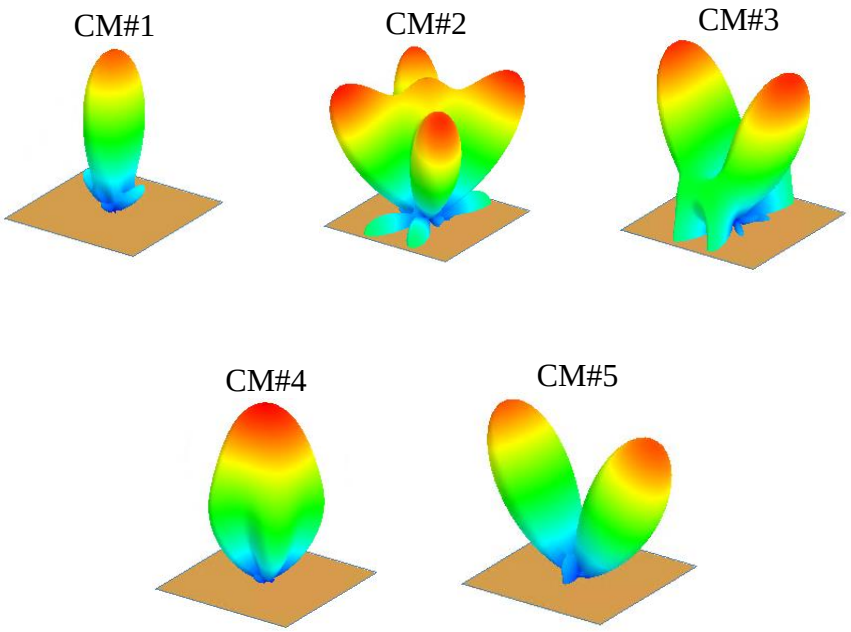

Figure 4.2-9: Computed far-zone field patterns (at 6 GHz) of the 5 most significant CMs of the shaped DRA in Fig.4.2-6.

4.2.8 Feed-Port Selection Considerations

In order to specify the actual feed mechanism type, number and locations, and so arrive at a complete design of the shape synthesized DRA, we examine the fields at the base of the DRA, for each of the significant CMs. These are shown in Fig.4.2-10 through Fig.4.2-12 for $\left|E_z(x,y,0^+)\right|$ and $\left|\bar{H}_{\tan}(x,y,0^+)\right|$. Appropriate feed mechanism types need to be used to couple to these field distributions in order to actually excite the required CMs. In the present case Fig.4.2-4(b) shows

that CM#1 is dominant. Enlarged versions of the distributions of $E_z(x, y, 0^+)$ and $H_y(x, y, 0^+)$ for CM#1 are shown in Fig.4.2-13 and Fig.4.2-14, respectively. The locations of the maxima of these quantities have been numbered (in view of their being potential locations of physical feed mechanisms), and their directions indicated.

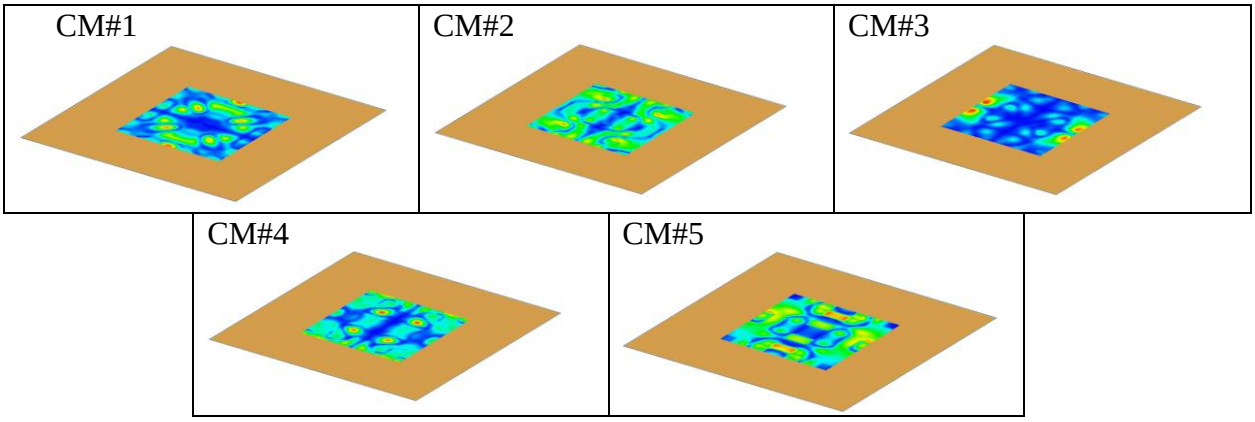

Figure 4.2-10: Magnitude of the normal component of the electric field $E_z(x, y, 0^+)$, for each CM indicated, below the shape synthesized DRA shown in Fig.4.2-6.

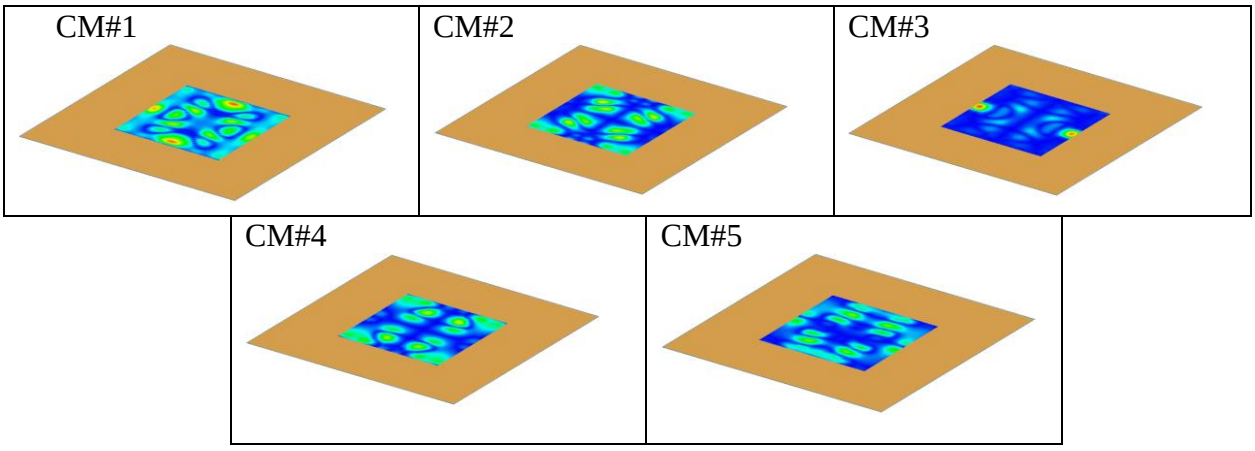

Figure 4.2-11: Magnitude of the tangential component of the magnetic field $H_y(x, y, 0^+) = \hat{y} \cdot \bar{H}_{\tan}(x, y, 0^+)$, for each CM indicated, below the shape synthesized DRA in Fig.4.2-6.

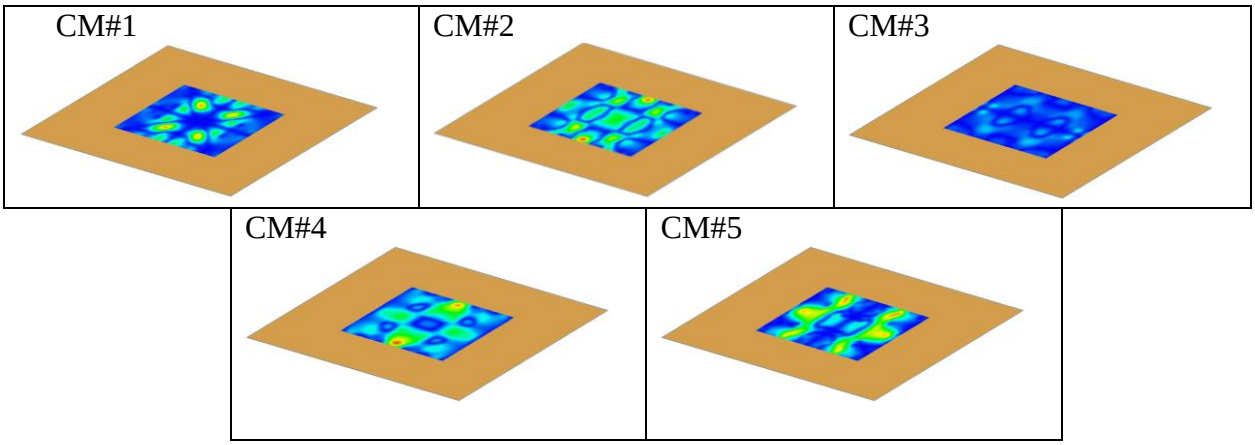

Figure 4.2-12: Magnitude of the tangential component of the magnetic field [Hx] $H_x(x,y,0^+) = \hat{x} \cdot \bar{H}_{\tan}(x,y,0^+)$ **, for each CM indicated, below the shape synthesized DRA in Fig.4.2-6.**

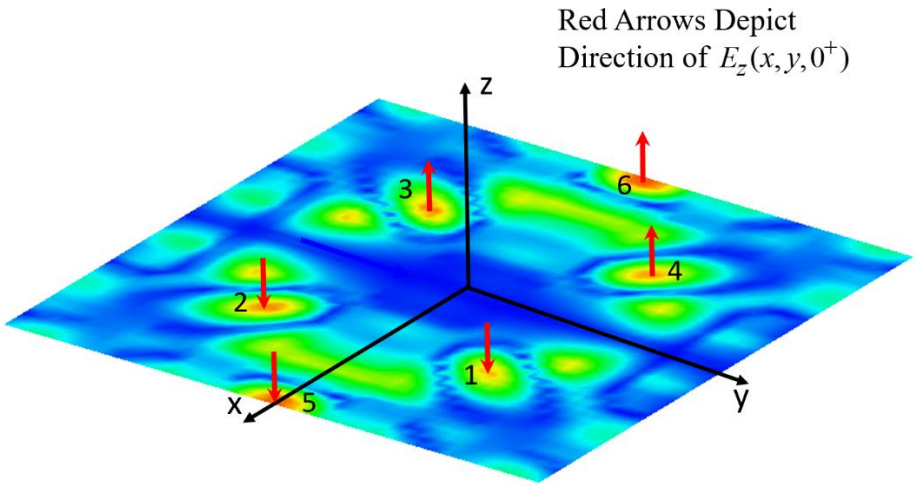

Figure 4.2-13: Sketch of electric field $E_z(x,y,0^+)$ **for CM#1, below the shape synthesized DRA of Fig.4.2-6. Location of the peaks of** $\left|E_z(x,y,0^+)\right|$ **have been numbered.**

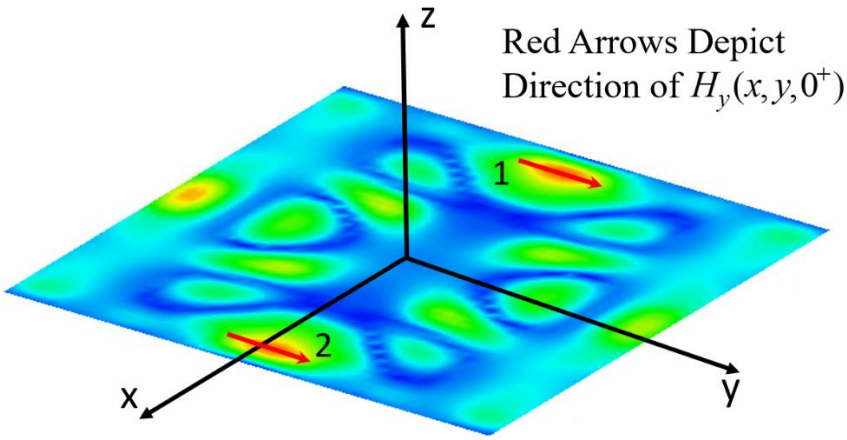

Figure 4.2-14: Sketch of the magnetic field $H_y(x,y,0^+)$ for CM#1, below the shape synthesized DRA of Fig.4.2-6. Location of the peaks of $\left|H_y(x,y,0^+)\right|$ have been numbered.

4.2.9 Feed-Mechanism Design: Four Probes

The performance described in Section 4.2.7 was that involving the attainable directivity, namely that possible, without entering the super-directivity regime, if it were possible to excite all N_{CM} modes with precisely the excitation coefficients in Fig.4.2-4(b). This would only be possible if a very large number of excitation points (the physical ports) were to be used, but this is not desirable in practice. It was for this reason that the modified F_{obj} was defined in Section 4.2.2. Thus we here consider the case of four coaxially-fed ports of the type described in Section 3.7, in other words probe feeds. These ports are located at locations 1 through 4 of Fig.4.2-13, where the magnitude of the field $E_z(x,y,0^+)$ of the dominant CM#1 has maxima[92]. A driven full-wave model of the shaped DRA, on a finite groundplane, and the four probes is constructed. The probe heights are simultaneously adjusted[93] in order to minimize the magnitude of S_{ij} for $i,j=1,2,3,4$, exploiting symmetry to reduce any computation time. Thereafter the four weights, constituting the weight vector[94] $[W]$ with which the probe feeds are to be fed, are optimized as described in Section 3.5.2

[92] We note here that, although we are using the diagrammatic representations of the various field components in the descriptions, key aspects (e.g. maxima) of these fields are easily located in an automated way by simple numerical "searching" procedures.

[93] Using an in-built optimization in the code HFSS; this is separate from the optimization algorithms used with the shape synthesis process developed in this thesis.

[94] Recall that this is different from the CM weight vector $[\mathcal{W}]$.

to maximize the actual directivity $D^{\max}(0^\circ, 0^\circ)$. It is assumed that a beamformer network[95] would be available to supply these weights. The resultant weights are shown in Table 4.2-1. They have the same magnitudes but the phases of w_3 and w_4 are at 180° relative to that of w_1 and w_2, given the opposite orientations of the $\left|E_z(x, y, 0^+)\right|$ at port#1 and port#2 compared to that at port#3 and port#4. In this post-shaping stage we are being "instructed", in this particular situation, to ensure that all four ports are effectively being fed in phase.

The computed directivity pattern in the xz- and yz-planes is that shown[96] in Fig.4.2-15, and a more qualitative rendition of the overall pattern by the 3D plot in Fig.4.2-16. It is immediately clear that the broadside directivity, at 12.1dBi, is lower than the 13.66 dBi of attainable directivity in Fig.4.2-7. It would be well to summarize the contributing reasons for this. Firstly, as already stated above, by using only four probes we cannot excite all the CMs as required in Fig.4.2-4(b) to achieve the 13.66 dBi. The use of two additional probes (e.g. at locations #5 and #6 in Fig.4.2-13) would increase the directivity, but at the cost of a more complex feed arrangement). Secondly, the insertion of physical conducting probes (or even slots, as we shall shortly see in Section 4.2.10) changes the geometry – the object is now not entirely dielectric but includes conducting probes, holes in the groundplane for the coaxial line from which the probes emerge, dielectric material removed to accommodate the probes - and hence the CMs will be perturbed[97]. Thirdly, the attainable 13.66 dBi was for an infinite groundplane, with no power radiated below it. This is not the case with this finite groundplane model, as Fig.4.2-15 confirms. If we artificially set all fields below the finite groundplane to zero, the computed broadside directivity is 12.51 dBi.

When using a DRA the feed mechanism will always contribute in some way. If the DRA proper is removed from the four-probe-fed full-wave model we obtain the directivity pattern cuts shown

[95] Many DRAs (in references mentioned in Section 2.3) designed for very specific performance have beamforming network type feed mechanisms composed of conducting transmission lines. It might then be argued that the low-loss advantage is lost. However, replacing the radiators by DRAs clearly remains worth the effort. At the higher millimetrewave frequencies the use of low-loss rectangular waveguides, now 3D printed, has started to make a comeback (e.g. [DAUR 15] at W-band 75 – 110 GHz) because of its small physical size, and slots in such waveguide walls could be used to feed a DRA at multiple points. This would likely be an acceptable fit into the whole "computational design and manufacturing" framework mentioned in Section 1.1.

[96] In all the computed performance data obtained using full-wave modelling that incorporate actual physical feed mechanisms (probes or slots) and finite groundplanes in this thesis, we have compared results when both HFSS and FEKO are used for such modelling, with insignificant differences.

[97] This is so if one thinks in terms of NMs also.

in Fig.4.2-17. As expected, the latter do not even have maxima in the broadside direction; the shaped DRA is indeed coupling to the probes and exciting the CMs in order to obtain a pattern with a directivity maximum on broadside. Its presence has not only shifted the direction of maximum directivity to the broadside directions (as required), but increased this value by 4dB.

The computed S-parameters S_{1m} for this four-probe-fed case are shown in Fig.4.2-18 as an example, and through symmetry is representative of the other ports. Improved matching (that is, lower S_{ii} magnitude values at the ports) could possibly be obtained by using a stepped probe; this would be possible if the DRA were to be fabricated using 3D printing. One issue that is immediately clear is that the magnitude of S_{ii} increases away from the centre-frequency 6 GHz. Such frequency-sensitivity is further seen in the broadside directivity plot in Fig.4.2-19, which shows that this quantity remains favourable close to 6 GHz, but falls off away from it. This is a consequence of the issue mentioned in Section 3.6.2, and emphasizes the need for a CM tool with improved tracking capabilities that would permit the DRA shape synthesis process devised here to easily incorporate bandwidth as a requirement. We did not shape synthesize to obtain a specific directivity, but to maximize the directivity obtainable with the starting material size, form and properties restrictions. Thus we could describe the result in Fig.4.2-19 as a low-profile enhanced-directivity DRA whose gain is larger than 9 dBi over an 8% bandwidth; but of course that would miss the point of the shape synthesis goal in the long term.

Table 4.2-1 : Beamforming weights of the four-probe-fed shape synthesized DRA of Fig.4.2-6.

Port Index *p*	**Port Location** (x_p, y_p)	**Beamforming Weights (w_p)**	**Probe Height (h)**
1	(13.4 mm, 13.4 mm)	$1.0 \angle 0°$	6.23mm
2	(13.4 mm, -13.4 mm)	$1.0 \angle 0°$	6.23mm
3	(-13.4 mm, -13.4 mm)	$1.0 \angle 180°$	6.23mm
4	(-13.4 mm, 13.4 mm)	$1.0 \angle 180°$	6.23mm

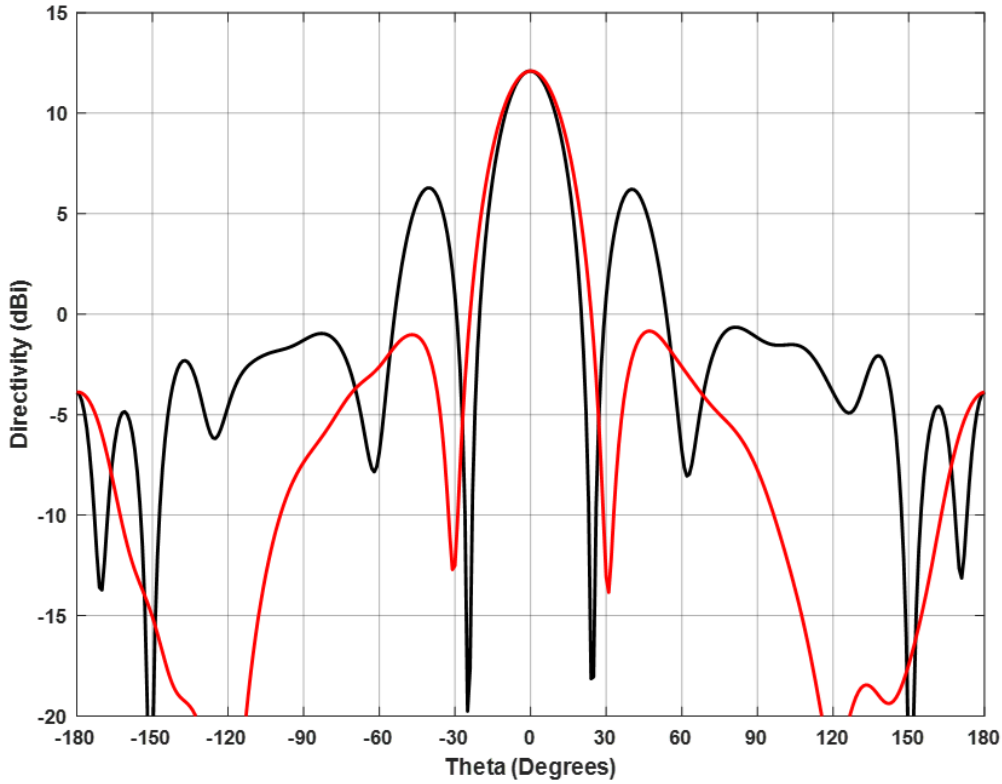

Figure 4.2-15: Directivity patterns, in the xz-plane (black) and yz-plane (red), of the four-probe-fed shape synthesized DRA of Fig.4.2-6. The directivity in broadside direction is 12.10 dBi.

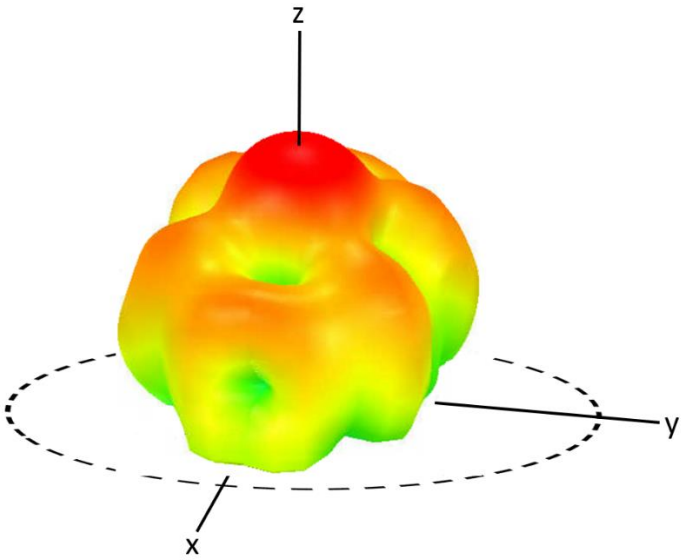

Figure 4.2-16: 3D depiction (in the upper hemisphere) of the directivity of the four-probe-fed shape synthesized DRA of Fig.4.2-6.

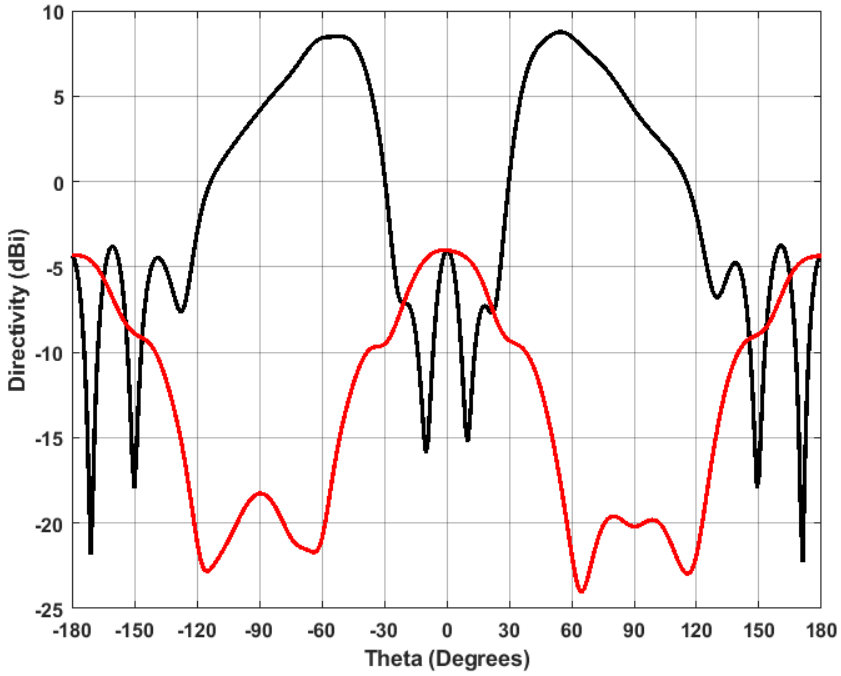

Figure 4.2-17: Directivity patterns, in the xz-plane (black) and yz-plane (red), of the four-probe-fed DRA of Fig.4.2-6, but with the dielectric material object (the "DRA proper") removed, leaving only the four probe feeds.

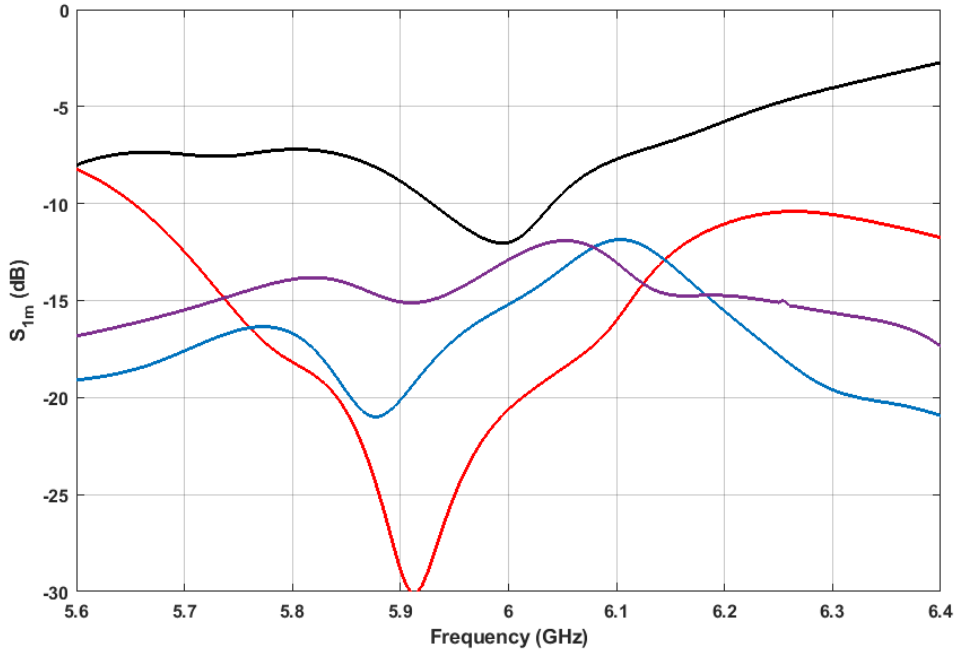

Figure 4.2-18: Magnitude of S_{11} (black), S_{12} (red), S_{13} (blue) and S_{14} (purple) versus frequency, for the shape-synthesized four-probe-fed antenna in Fig.4.2-6.

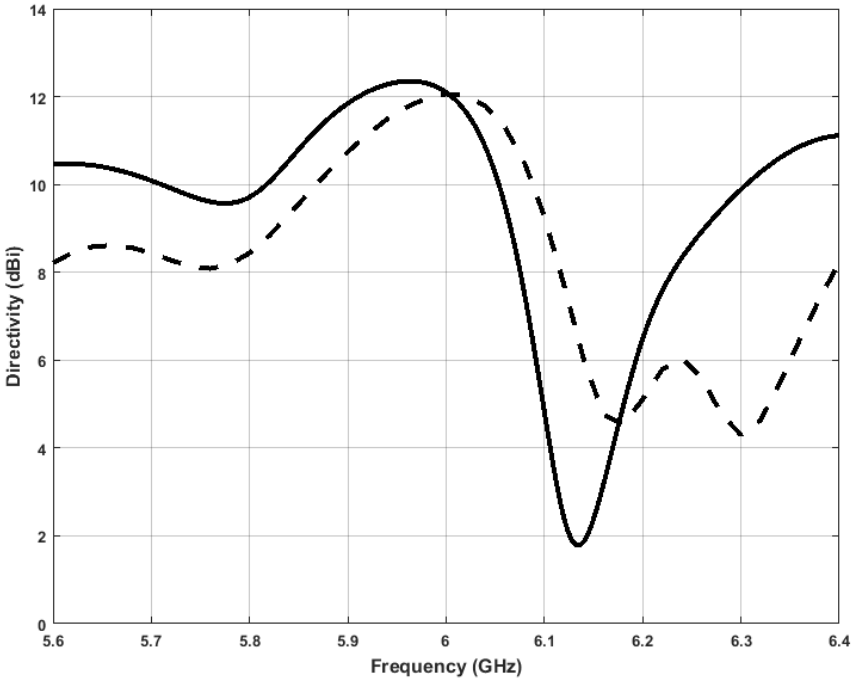

Figure 4.2-19: Maximum directivity values versus frequency for the shape synthesized DRA fed by four probes (solid curve) and by two slots (dashed curve).

4.2.10 Feed-Mechanism Design: Two Slots

Just as Fig.4.2-13 suggested the possible locations for probe feeds to couple to the dominant CM, Fig.4.2-14 shows how the magnitude of $H_y(x, y, 0^+)$ suggests the location of two slots for the same purpose. The driven full-wave model of the two-slot-fed shaped DRA, on the same finite groundplane, is used to determine the weights w_1 and w_2 of the two slots, whose locations are provided in Table 4.2-2, along with the optimized values of the said weights to maximize the broadside directivity. The resulting computed directivity pattern is that in Fig.4.2-20, the maximum broadside directivity being the same as that obtained for the four-probe-fed case. The 3D pattern (in the upper hemisphere) is depicted in Fig.4.2-21; the overall performance is different from that when the four-probe-feeding is used with the same DRA. The fact that the slots couple to the DRA modes, as we intend them to, is again confirmed by inspection of the directivity patterns in Fig.4.2-22, which are those with the DRA material removed and only the two slots radiating.

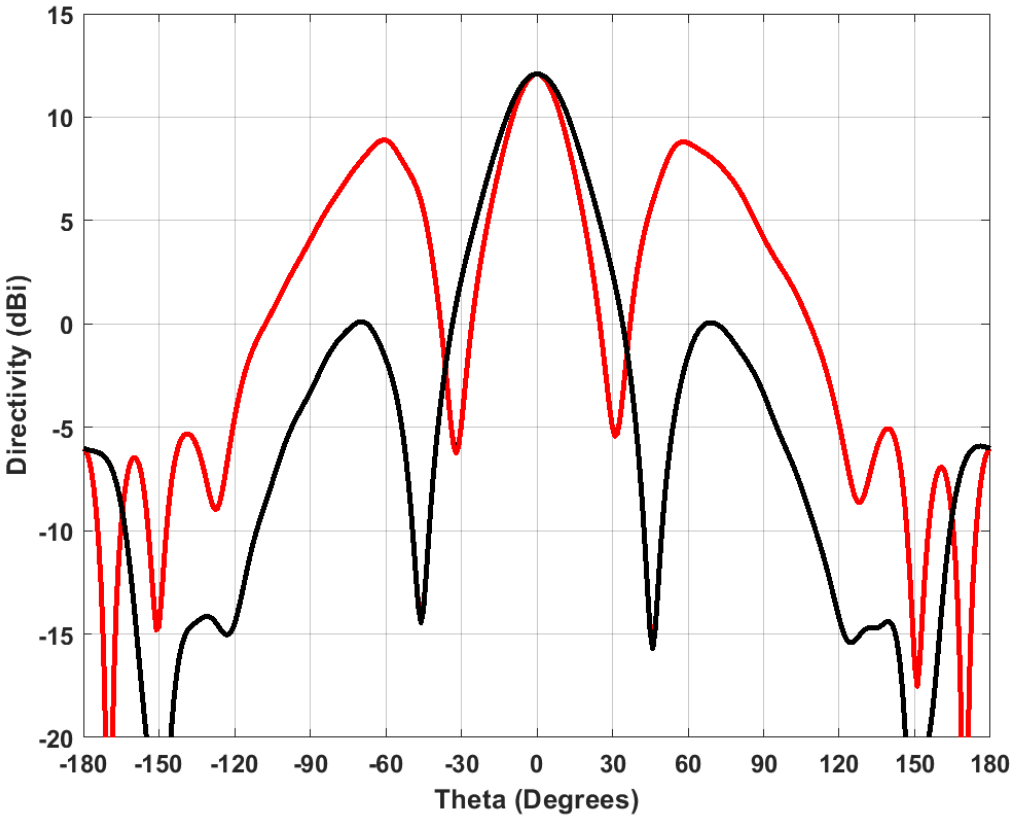

Figure 4.2-20: Directivity patterns, in the xz-plane (red) and yz-plane (black)planes, of the two-slot-fed shape synthesized DRA in Fig.4.2-6. The directivity in broadside direction is 12.09 dBi.

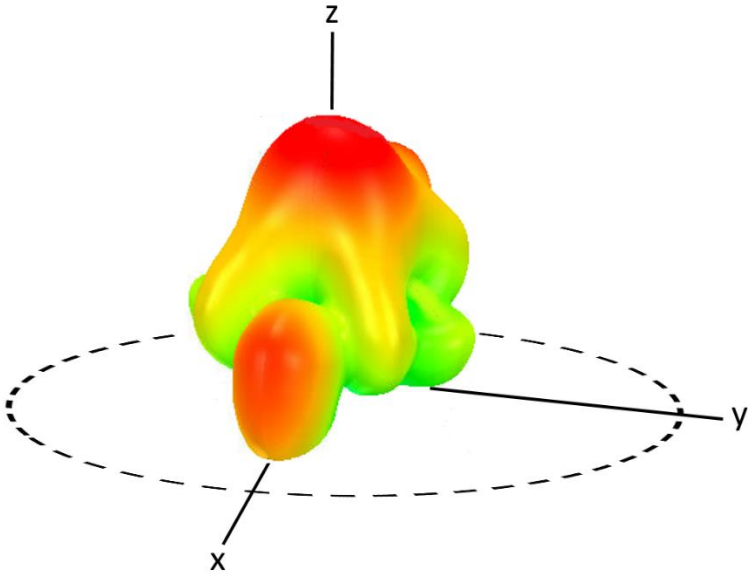

Figure 4.2-21: 3D depiction of the directivity of the four-probe-fed shape synthesized DRA in Fig.4.2-6.

Table 4.2-2 : Beamforming weights of the two-slot-fed shape synthesized DRA shown in Fig.4.2-6. The slot length is 8.4 mm and the width is 2.0 mm.

Port Index p	Port Location (x_p, y_p)	Beamforming Weights w_p
1	(31 mm, 0 mm)	$1\angle 0°$
2	(-31 mm, 0 mm)	$1\angle 0°$

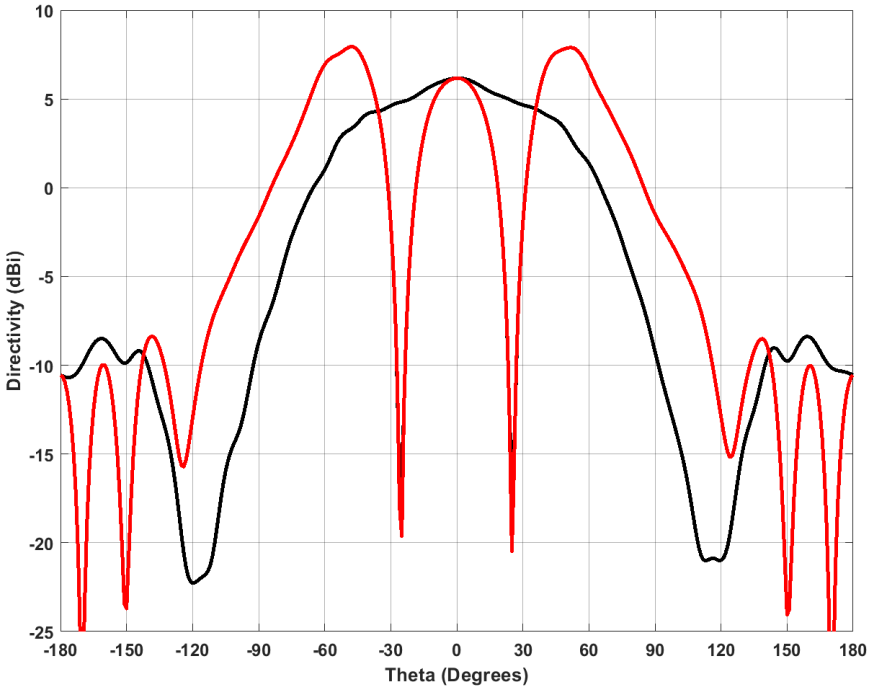

Figure 4.2-22: Directivity patterns, in the xz-plane (red) and yz-plane (black), of the two-slot-fed DRA, but with the dielectric material object (the "DRA proper") removed, leaving only the two slot feeds.

In later sections of the thesis, we will use infinitesimal dipole sources to provide "quick" estimates of what is obtained with actual feed mechanisms. We use an infinitesimal electric dipole perpendicular to the groundplane to emulate a "monopole" probe, and an infinitesimal magnetic dipole parallel to the groundplane to emulate a slot. We note that when using the infinitesimal dipoles as sources, the structure is not altered from what it was for the CM analysis except for the fact that the groundplane is finite; there is no additional conductor present (e.g. probes) or conductor removed (e.g. slots). If we do this, using the same weights for the infinitesimal dipoles as done for the actual probe and slot cases, the directivity patterns shown in Fig.4.2-23 and Fig.4.2-24 result. The patterns obtained with the infinitesimal dipole surrogates are close to those obtained

using the actual probes and slots. This suggests that the CMs of the structure with actual probes and slots change relatively little (they are a perturbation) from that without probes and slots. Thus if, as discussed in Section 3.6.3, it were possible to use sub-structure CMs (that would account for the finite groundplane), the attainable directivity and actual directivity (using probes and slots) would differ less.

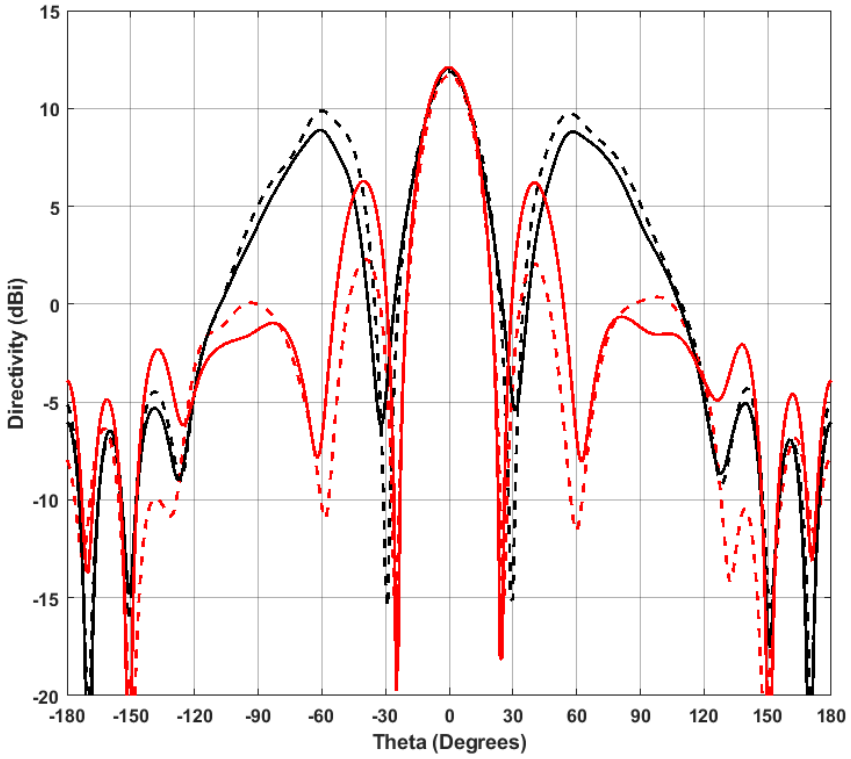

Figure 4.2-23: Directivity pattern, in the xz-plane, of the shape synthesized DRA shown in Fig.4.2-6. The black solid curve (——) is that for the appropriately excited two slots, the solid red curve (——) when it is excited by four probes, the black dashed curve (- - - -) when it is excited by two tangential infinitesimal magnetic dipoles, and the red dashed curve (- - - -) when it is excited by four perpendicular infinitesimal electric dipoles.

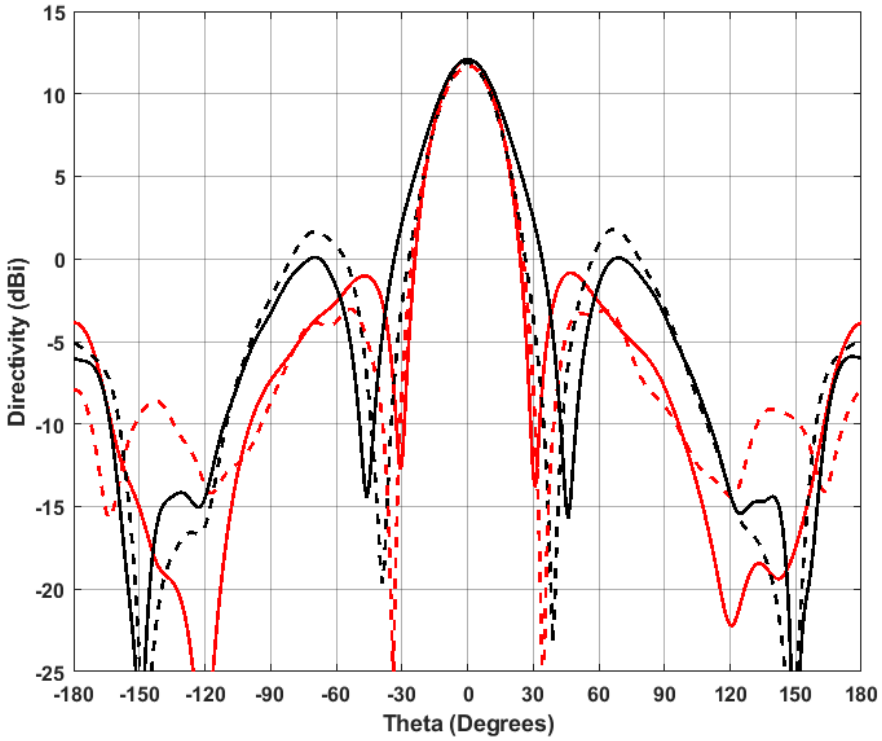

Figure 4.2-24: Directivity pattern, in the yz-plane, of the shape synthesized DRA shown in Fig.4.2-6. The black solid curve (——) is that for the appropriately excited two slots, the solid red curve (——) when it is excited by four probes, the black dashed curve (- - - -) when it is excited by two tangential infinitesimal magnetic dipoles, and the red dashed curve (- - - -) when it is excited by four perpendicular infinitesimal electric dipoles.

4.3 SHAPE SYNTHESIS OF A DRA FOR MAXIMIZATION OF OFF-BROADSIDE DIRECTIVITY $D_\phi(N_{CM},\theta_s,\phi_s)$

4.3.1 Initial Remarks

In order to further exercise the proposed shape synthesis method, we next consider the requirement to synthesize a DRA that has its maximum partial directivity $D_\phi(\theta_s,\phi_s)$ in the $(\theta_s,\phi_s)=(30^\circ,0^\circ)$ direction[98]. The starting shape (and its electrical size) is the same as in Section 4.2.2, except that quadrantal symmetry was not enforced; instead, only symmetry left and right of the xz-plane was mandated. The voxelation of the starting shape is identical to that in Section 4.2.3, with DoF equal to 100. The voxel size is contingent upon the fabrication tolerance and the desired geometrical resolution. One may initially use a certain voxel size to obtain results, and subsequently, iteratively reduce the voxel size to improve accuracy and precision in the results.

4.3.2 Construction of a Suitable Objective Function, and Shaping Recipe

The broadside case in Section 4.2 maximized the total directivity. In the present case we wish to demonstrate that specific polarization control is possible in the shape synthesis procedure, and hence will use as the first portion of the objective function in terms of the attainable partial directivity[99]

$$F_p(N_{CM},\theta_s,\phi_s)=\begin{cases}10\log\left\{D_p(N_{CM},\theta_s,\phi_s)\right\} & \text{if } \left|AR^{dB}(\theta_s,\phi_s)\right|>\left|AR_{spec}^{dB}\right| \\ C_o & \text{Otherwise}\end{cases} \qquad (4.3\text{-}1)$$

where $AR^{dB}(\theta_s,\phi_s)=20\log\left\{\left|AR(\theta_s,\phi_s)\right|\right\}$, the quantity $AR_{spec}^{dB}=20\log\left|AR_{spec}\right|$ is the smallest axial ratio magnitude allowed (to ensure good linear polarization), and constant $C_o\le 0$. Quantity $AR(\theta_s,\phi_s)$ is calculated using the expressions given in Section 2.2.6, with $(\theta,\phi)=(\theta_s,\phi_s)$ the direction in which we desire to have the maximum directivity.

[98] This direction was selected to confirm that the shape synthesis is able to provide more than merely close-to-broadside patterns.

[99] Partial directivity $D_p(\theta,\phi)$ has been defined in Section 3.2.

The actual objective function is then

$$F_{obj} = F_{\alpha}(N_{CM}, N_{\alpha})F_{p}(N_{CM}, \theta_s, \phi_s) \tag{4.3-2}$$

During shaping, for each shape of the population, we determine the $[\mathcal{W}]$ via a sub-optimization using the QFA approach that maximizes the attainable partial directivity

$$D_{p}(N_{CM}, \theta_s, \phi_s) = \frac{2\pi}{\eta_o} \frac{[\mathcal{W}]^{H}[\mathrm{A}_{p}(\theta_s, \phi_s)][\mathcal{W}]}{[\mathcal{W}]^{H}[\mathrm{B}][\mathcal{W}]} \tag{4.3-3}$$

This $[\mathcal{W}]$, for each different shape in the population at the current overall shaping iteration, is used to evaluate $D_{p}(N_{CM}, \theta_s, \phi_s)$, which upon substitution into (4.3-1) provides $F_{p}(N_{CM}, \theta_s, \phi_s)$, so that finally F_{obj} in (4.3-2) can be found for that particular shape. In both off-broadside examples below we have set $AR_{spec}^{dB} = 15dB$, often regarded as representing satisfactory linear polarization in practice [STUT 08].

4.3.3 Shaping Outcome for the Case $N_{\alpha} = 6$

The symmetries that occur in the radiation patterns of individual CMs suggest that more than a single CM is needed to maximize the attainable directivity in an off-broadside direction (that is, a non-symmetrical pattern). It is for this reason that we select $N_{\alpha} = 6$, in order to "allow" the shaping the opportunity to arrive at a shape for which several CMs are significant. The outcome is the shape synthesized DRA in Fig.4.3-1.

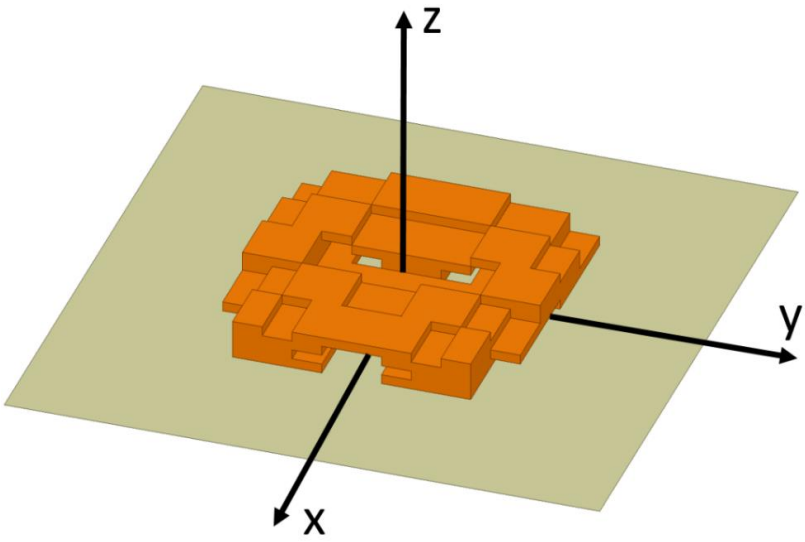

Figure 4.3-1: Geometry of the DRA shape synthesized with $N_\alpha = 6$ for maximum $D_\phi(N_{CM},\theta_s,\phi_s)$ in direction $(\theta_s = 30^\circ, \phi_s = 0^\circ)$.

Fig.4.3-2(a) shows that if we do not limit the number of CMs that are the most significant, higher-order CMs "take the lead" (which CMs would be more difficult to excite); it produces[100] an attainable $D_\phi(N_{CM},30^\circ,0^\circ)$ of 14.26dBi. On the other hand, using $N_\alpha = 6$ results in the elements of $[\mathcal{W}]$ being those in Fig.4.3-2(b), where CM#2 is the dominant mode. The attainable partial directivity patterns are those in Fig.4.3-3 and Fig.4.3-4. The attainable $D_\phi(N_{CM},30^\circ,0^\circ)$ has a value of 13.75dBi; this is the price paid for penalizing the CMs with indices $n > N_\alpha$ during shaping. The shape synthesis has been successful in keeping the unwanted $D_\theta(N_{CM},\theta,\phi)$ low. Although the axial ratio in direction $(\theta_s = 30^\circ, \phi_s = 0^\circ)$ is larger than 53dB even though we only required $AR_{spec}^{dB} > 15dB$, we have found that not limiting the axial ratio via the objective functions may cause unacceptably low axial ratios to arise. Merely limiting the axial ratio apparently steers the shape synthesis in the desired direction.

[100] This would be for a different shape to that in Fig.4.3-1.

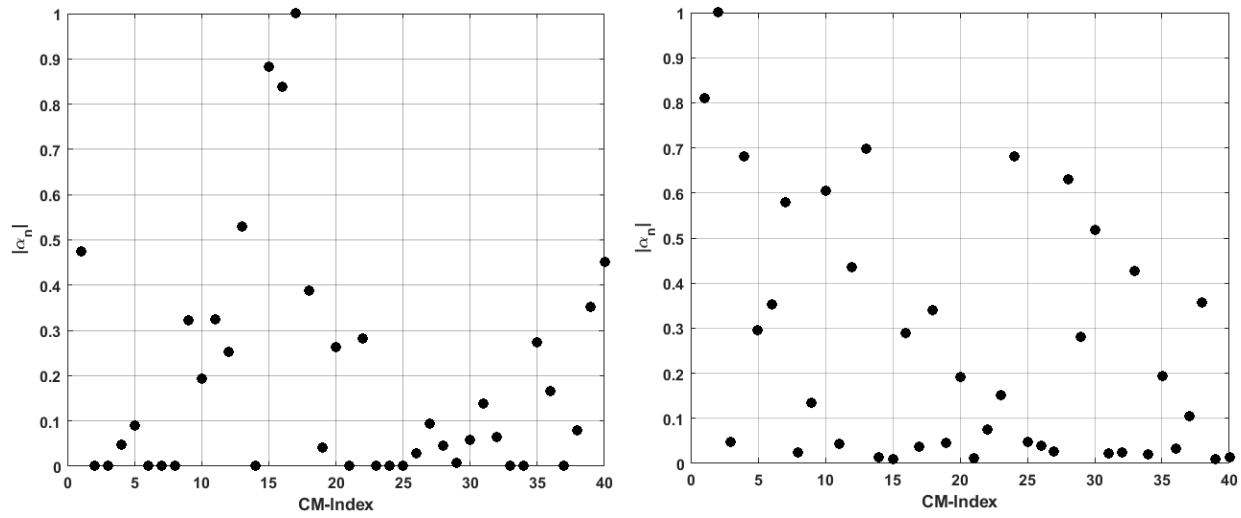

(a) **(b)**

Figure 4.3-2: Modal weighting coefficient magnitudes for achieving the ideal attainable directivity for DRAs shape synthesized (a). with all $N_\alpha = N_{CM} = 40$, and (b). with $N_\alpha = 6$.

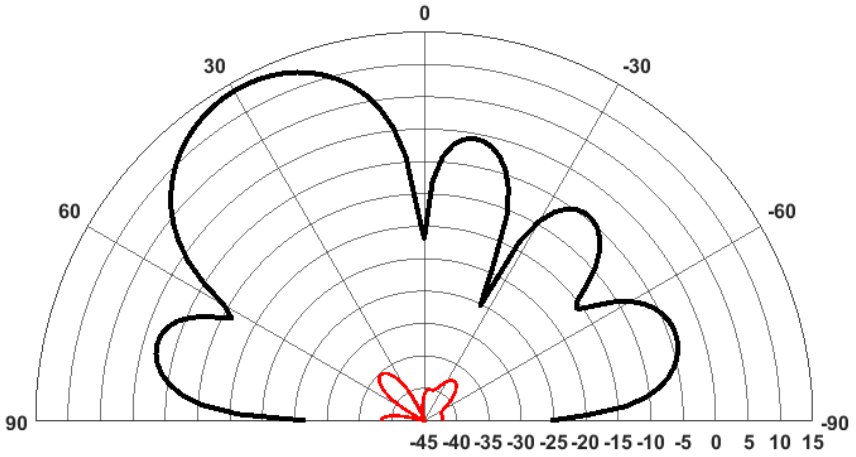

Figure 4.3-3: Attainable partial directivity pattern $D_\phi(N_{CM}, 30^\circ, 0^\circ)$, at 6 GHz, in the xz-plane (black curve) of the shape synthesized DRA of Fig.4.3-1. The directivity in direction $(\theta_S, \phi_S) = (30^\circ, 0^\circ)$ is 13.75dBi. Partial directivity pattern $D_\theta(N_{CM}, \theta, 0^\circ)$ in the same plane is the red curve, and is much lower, as required.

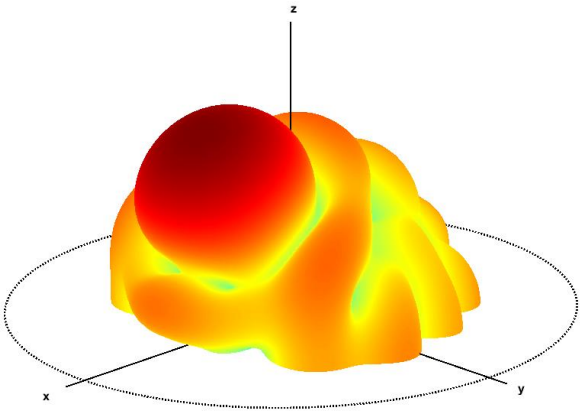

Figure 4.3-4: Attainable partial directivity 3D pattern representation $D_{\phi}(N_{CM}, 30^{\circ}, 0^{\circ})$, at 6 GHz, of the shape synthesized DRA of Fig.4.3-1. The directivity in direction $(\theta_S, \phi_S) = (30^{\circ}, 0^{\circ})$ is 13.75dBi.

4.3.4 Feed-Port Selection Considerations

In Fig.4.3-6, and Fig.4.3-7(a) and (b), we show the magnitudes of the fields $E_z(x, y, 0^+)$, $H_x(x, y, 0^+)$ and $H_y(x, y, 0^+)$ of CM#2, respectively, at the base of the DRA. Fig.4.3-7 has been added to indicate that the magnitude of $H_x(x, y, 0^+)$ at the two maxima are not the same; we see in Fig.4.3-7 that the phase of $H_x(x, y, 0^+)$ at these locations are opposite to each other. In spite of the fact that the shaping process is automated it remains useful to interpret details when examining the shape synthesized DRA and its fields. Thus we interpreted how shaping had controlled the CMs in Section 4.2.7, and in Section 4.2.9 were able to deduce a reason the optimized weights emerged to be those in Table 4.2-1. Here, for example, we have by the dashed lines in Fig.4.3-8 attempted to illustrate the half-loops formed by the electric field peaks shown in Fig.4.3-5. Examination of the sense of these half-loops corresponds precisely to the tangential magnetic field maxima locations and orientations in Fig.4.3-6 (a) and (b).

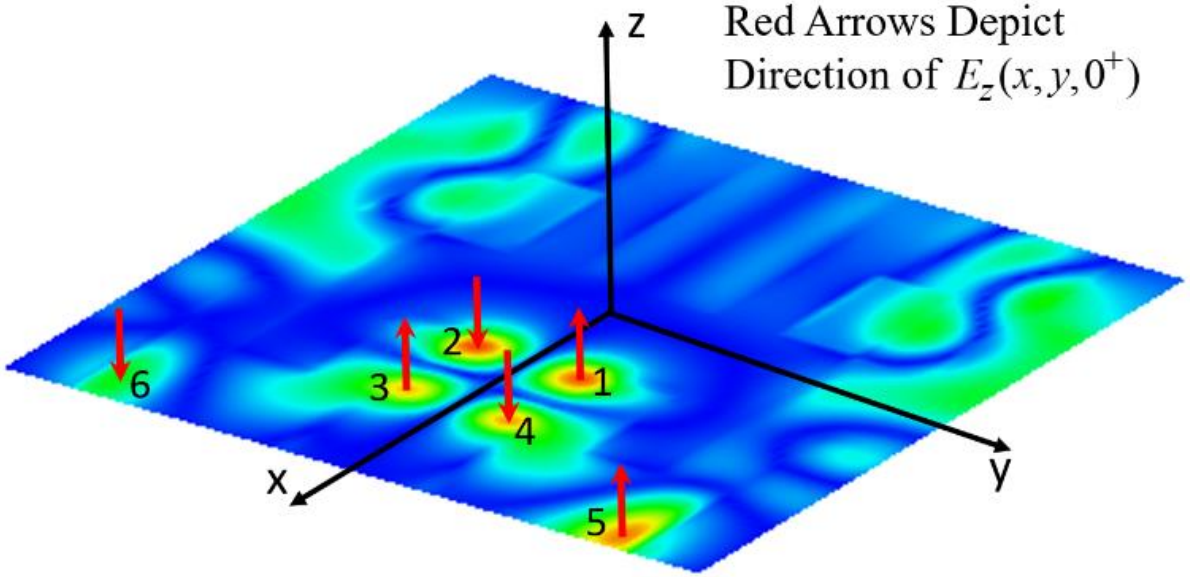

Figure 4.3-5: Sketch of electric field $E_z(x,y,0^+)$ for CM#2, below the DRA (shown in Fig.4.3-1) shape synthesized for maximum $D_\phi(N_{CM},30^\circ,0^\circ)$. Location of the peaks of $\left|E_z(x,y,0^+)\right|$ have been numbered for easy reference.

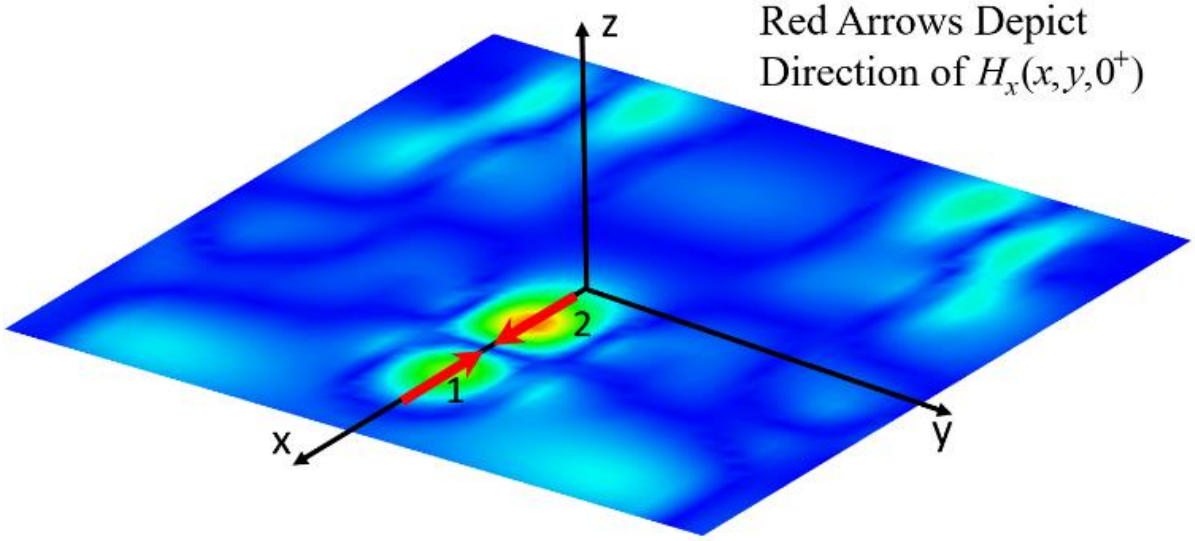

(a)

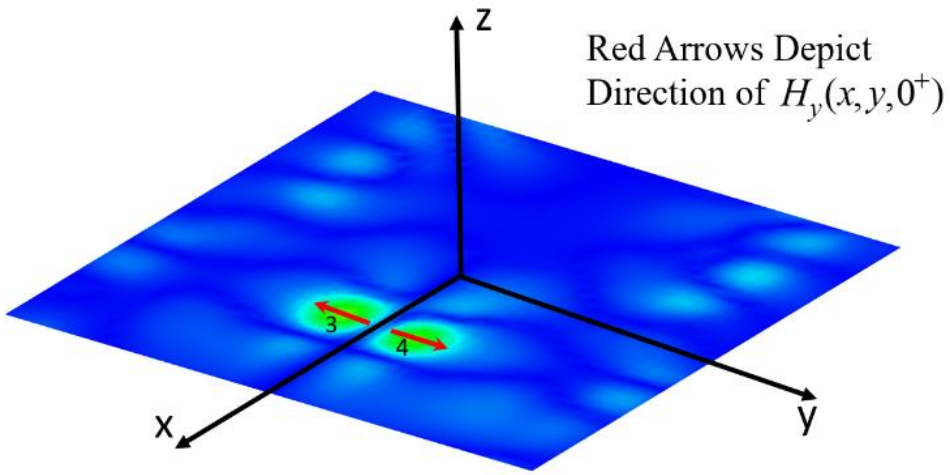

(b)

Figure 4.3-6: Sketch of the tangential magnetic field components (a). $H_x(x,y,0^+)$ **and (b).** $H_y(x,y,0^+)$**, for CM#2, below the DRA (shown in Fig.4.3-1) shape synthesized for maximum** $D_\phi(N_{CM},30^\circ,0^\circ)$ **. Location of the peaks of** $H_x(x,y,0^+)$ **have been numbered for easy reference.**

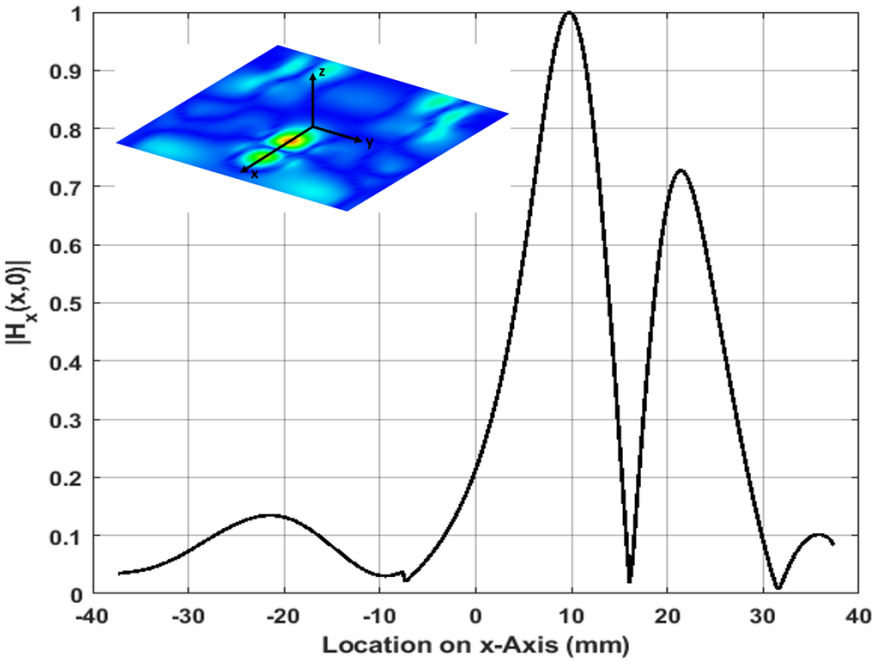

Figure 4.3-7: Magnitude of the tangential component of the magnetic field $H_x(x,y,0^+)$ **for CM#2 along the x-axis, below the DRA (shown in Fig.4.3-1) shape synthesized for maximum** $D_\phi(N_{CM},30^\circ,0^\circ)$ **.**

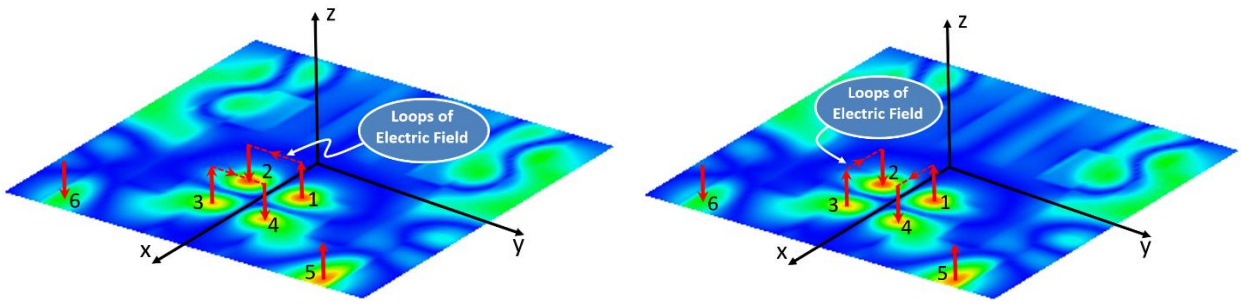

(a) **(b)**

Figure 4.3-8: Depiction of infinitesimal "half-loops" of the electric field $\bar{E}(x,y,0^+)$ for CM#2, easily related by inspection to the tangential magnetic fields $H_x(x,y,0^+)$ and $H_y(x,y,0^+)$ in Fig.4.3-6(a) and (b), respectively.

4.3.5 Feed-Mechanism Design: Slot Feeds

As before, when using actual physical mechanisms (in this case, slots) to feed the shaped DRA, it is modelled as a driven full-wave problem, and placed on a finite-sized square groundplane. Here we have two slots placed at the locations labelled in Fig.4.3-6(a), each with its long side parallel to the x-axis. Optimization of the weights produces the values reported in Table 4.3-1. The different amplitudes and phases of the two weights are seen to compensate for the different levels and orientations of $H_x(x,y,0^+)$ shown in Fig.4.3-6(a) and Fig.4.3-7. The co-polarized and cross-polarized partial directivity patterns information, $D_\phi(\theta,\phi)$ and $D_\theta(\theta,\phi)$ respectively, are displayed in Fig.4.3-9 and Fig.4.3-10. $D_\phi(\theta,\phi)$ has a maximum in direction $(\theta_s = 30^\circ, \phi_s = 0^\circ)$ as required, of value 10.76 dBi. $D_\theta(\theta,\phi)$ is low everywhere, with the axial ratio in direction $(\theta_s = 30^\circ, \phi_s = 0^\circ)$ being greater than 58dB.

As confirmation of the fact that the DRA modes are being excited, Fig.4.3-11 show the patterns when the DRA is removed and only the two slots remain. It is the presence of the DRA that causes the pattern to "scan" to the desired off-broadside direction.

Table 4.3-1 : Beamforming weights of the slot-fed shape synthesized DRA in Fig.4.3-1. The slot length is 9.4mm and the width is 3.0mm.

Port Index *p*	Port Location (x_p, y_p)	Beamforming Weights w_p
1	(21.45 mm , 0.0 mm)	$0.69 \angle 0°$
2	(9.75 mm, 0.0 mm)	$1.0 \angle 180°$

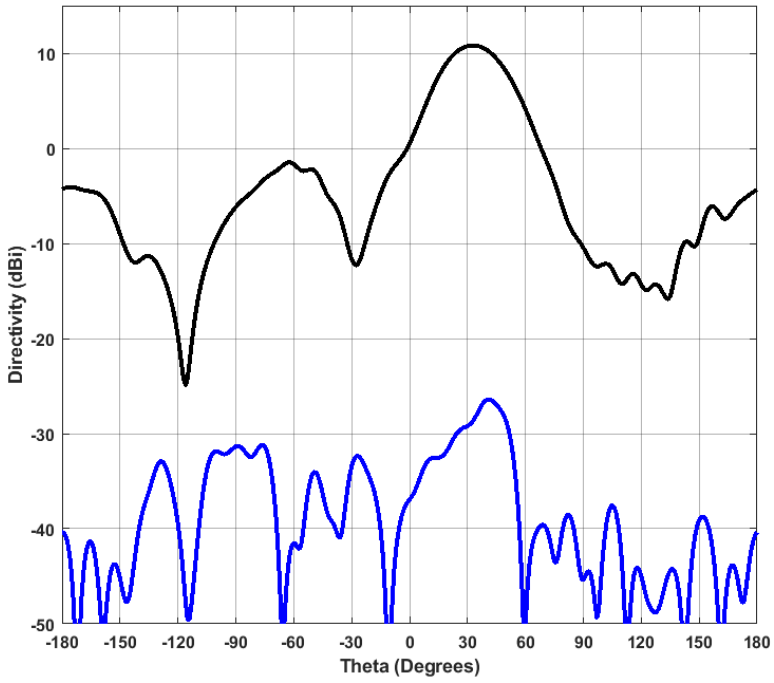

Figure 4.3-9: Co-polarized partial directivity pattern $D_\phi(\theta,\phi)$ shown as the black curve, and cross-polarized partial directivity $D_\theta(\theta,\phi)$ shown as the blue curve, at 6 GHz, in the xz-plane, of the shape synthesized DRA shown in Fig.4.3-1. Two slots are used to feed the DRA, resulting in $D_\phi(N_{CM}, 30^\circ, 0^\circ) = 10.76\,\text{dBi}$.

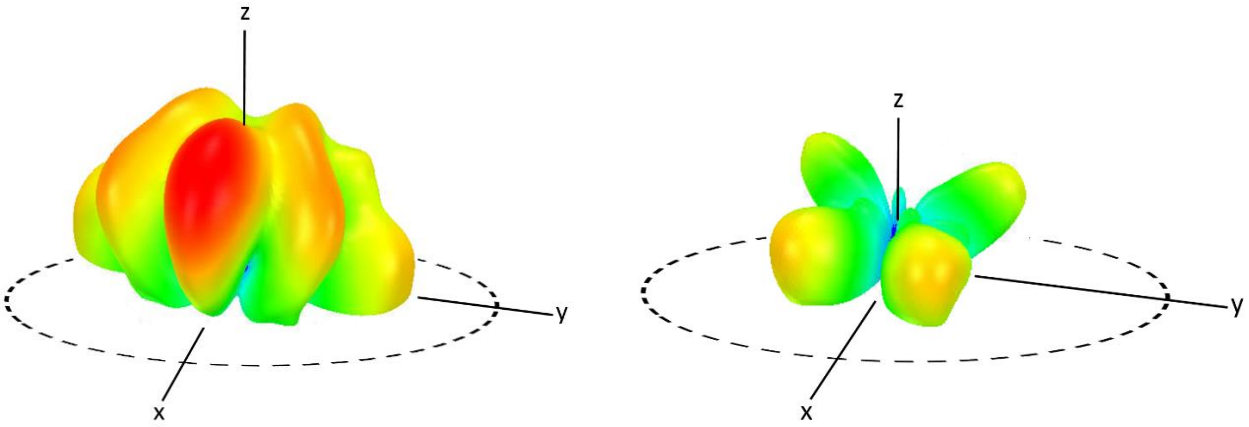

Figure 4.3-10: 3D depiction of the partial directivities $D_\phi(\theta,\phi)$ (left) and $D_\theta(\theta,\phi)$ (right) of the two-slot-fed shape synthesized DRA in Fig.4.3-1.

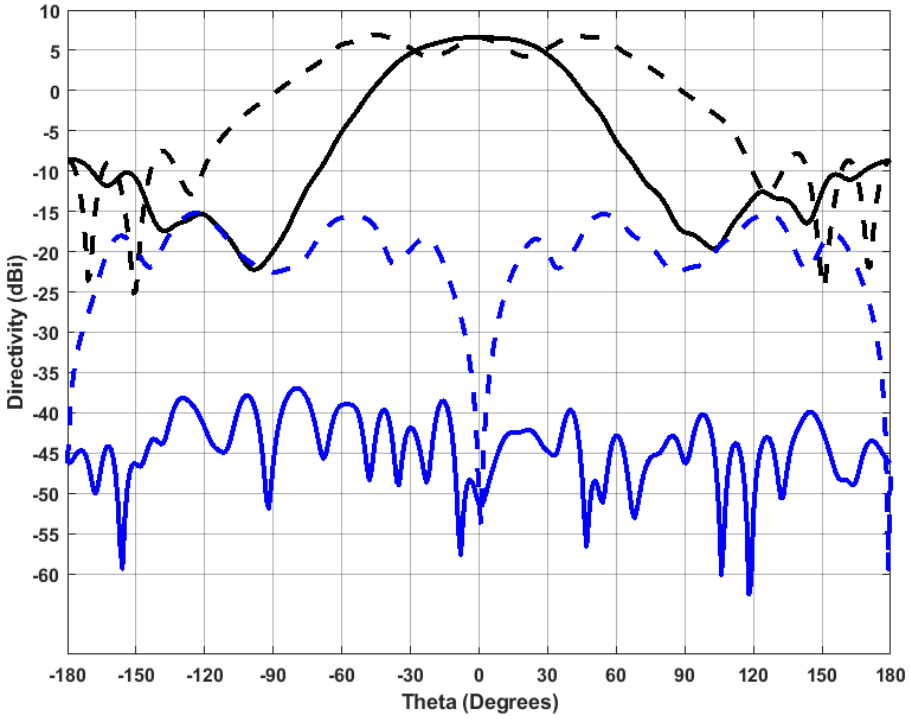

Figure 4.3-11: Partial directivity patterns $D_\phi(\theta,0^\circ)$ shown as the black curves, and partial directivity patterns $D_\theta(\theta,0^\circ)$ shown as the blue curves, at 6 GHz, with the DRA removed and only the two slots remaining. The solid curves are in the xz-plane and the dashed curves in the yz-plane.

4.3.6 Feed-Mechanism Design : Probe Feeds

The shaped DRA is next excited using four probes placed at the locations labelled #1 through #4 in Fig.4.3-5. Optimization of the weights produces the values shown in Table 4.3-2. In this instance it is not straightforward to interpret why the optimized weights turn out to have the values reported Table 4.3-2. We can understand that the weight magnitudes of ports#3 and #4 are larger than those of ports#1 and #2 – the field $E_z(x, y, 0^+)$ is significantly larger at the former locations compared to the latter.

The co-polarized and cross-polarized partial directivity patterns in the xz-plane, $D_\phi(\theta,\phi)$ and $D_\theta(\theta,\phi)$ respectively, are shown displayed in Fig.4.3-12. $D_\phi(\theta,\phi)$ has a maximum in direction $(\theta_s = 30^\circ, \phi_s = 0^\circ)$ as required[101] but, at 8.02dBi, it is almost 3dB lower than when two-slot-feeding was used for the same shaped DRA in Section 4.3.5. Furthermore, the overall pattern, seen in Fig.4.3-13, reveals high lobes away from the peak direction, once again less favourable than the two-slot-fed case previously shown in Fig.4.3-10. The S-parameters are included in Fig.4.3-14 and Fig.4.3-15 for completeness, with comments similar to those in Section 4.2-9.

In order to verify that the use of additional feed ports would allow the excitation of CMs more closely to that in Fig.4.3-2(b), and hence improve the D_ϕ, additional probes were added at locations #5 and #6 of Fig.4.3-5. The resulting optimized weights of the now six-probe-fed shaped DRA[102] are those in Table 4.3-3. The resulting radiation patterns in Fig.4.3-16 and Fig.4.3-17 are markedly improved from those of the four-probe-fed case, with the directivity increasing by 3.64dB to 11.66dBi. This is larger than that obtained with the two-slot feed in Section 4.3-5. The logical next step was to use not only the two slots (parallel to the x-axis) at locations #1 and #2 in Fig.4.3-6(a), but two additional slots (parallel to the y-axis) at locations #3 and #4 in Fig.4.3-6(b). However, this did not improve the partial directivity, since it was difficult to place four physical finite-length slots so close together at their optimal positions. This serves as an illustration of the convenience of being able to observe combination of the CM fields in the post-shaping stage and

[101] $D_\theta(\theta,\phi)$ is greatly reduced, as expected, the axial ratio in direction $(\theta_s = 30^\circ, \phi_s = 0^\circ)$ being 40dB.

[102] The same DRA as in Fig.4.3-1 of course.

be able to select different feeding mechanisms. There is nothing stopping us from using a combination of probes and slots if this would be favourable for practical reasons. If it were possible to find the CMs for dielectric objects on a PEC/substrate combination (as shown in Fig.3.6-5), then proximity feeds[103] would be an attractive solution, with the latter's fields "matched" to that of the CM combination of the attainably-excited DRA.

Table 4.3-2 : Beamforming weights of the shape synthesized DRA of Fig.4.3-1.

Port Index p	**Port Location** (x_p, y_p)	**Beamforming Weights** w_p	**Probe Height**
1	(10.3 mm, 6.0 mm)	$0.31 \angle 0°$	5.5mm
2	(10.3 mm, -6.0 mm)	$0.31 \angle 180°$	5.5mm
3	(21.5 mm, -6.0 mm)	$1.0 \angle 180°$	6.1mm
4	(21.5 mm, 6.0 mm)	$1.0 \angle 0°$	6.1mm

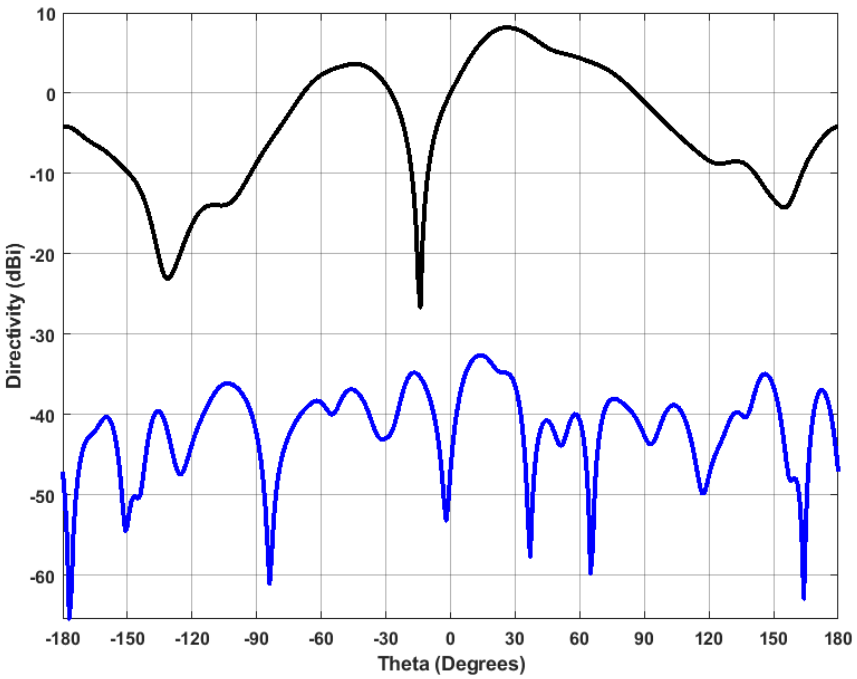

Figure 4.3-12: Co-polarized partial directivity pattern $D_\phi(\theta, 0^\circ)$ shown as the black curve, and cross-polarized partial directivity $D_\theta(\theta, 0^\circ)$ shown as the blue curve, at 6 GHz, in the xz-plane, of the shape synthesized DRA shown in Fig.4.3-1. Four probes are used to feed the DRA, resulting in $D_\phi(N_{CM}, 30^\circ, 0^\circ) = 8.02\,\text{dBi}$.

[103] In which the DRA would be placed directly on top of the conducting tracks of a microstrip or coplanar-waveguide beamforming network that "snakes" appropriately to couple to the CM-combination fields of the shape synthesized DRA.

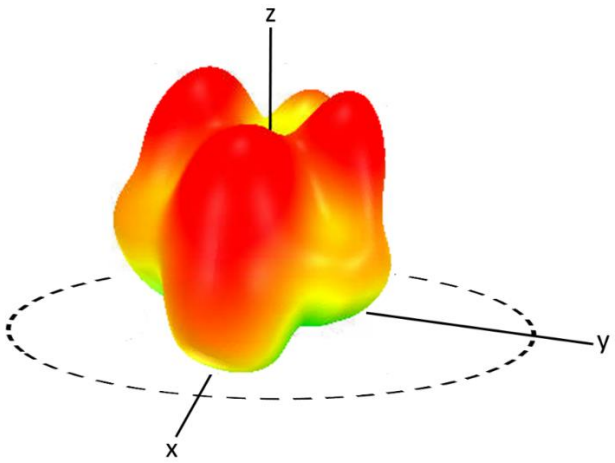

Figure 4.3-13: 3D depiction of the partial directivity $D_\phi(\theta,\phi)$ of the four-probe-fed shape synthesized DRA in Fig.4.3-1.

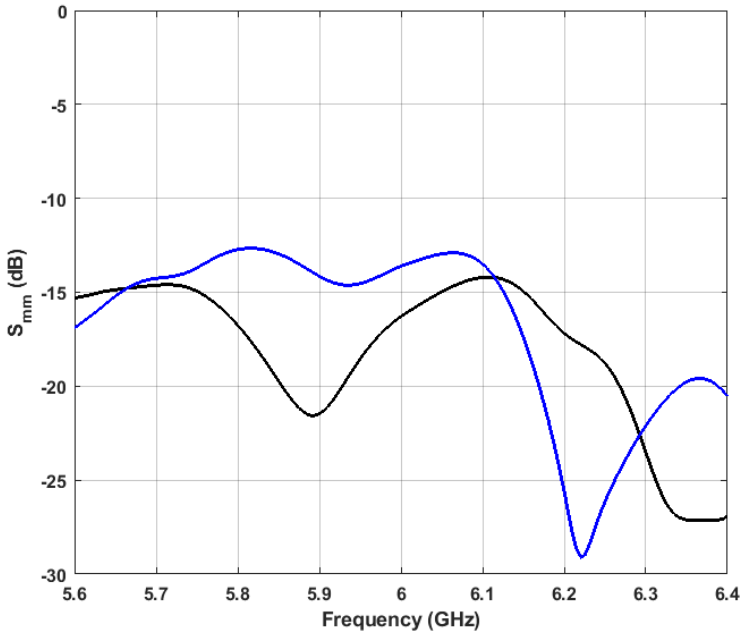

Figure 4.3-14: Magnitude of $S_{11} = S_{22}$ (black) and $S_{33} = S_{44}$ (blue) versus frequency, for the shape-synthesized 4-port probe-fed antenna shown in Fig.4.3-1.

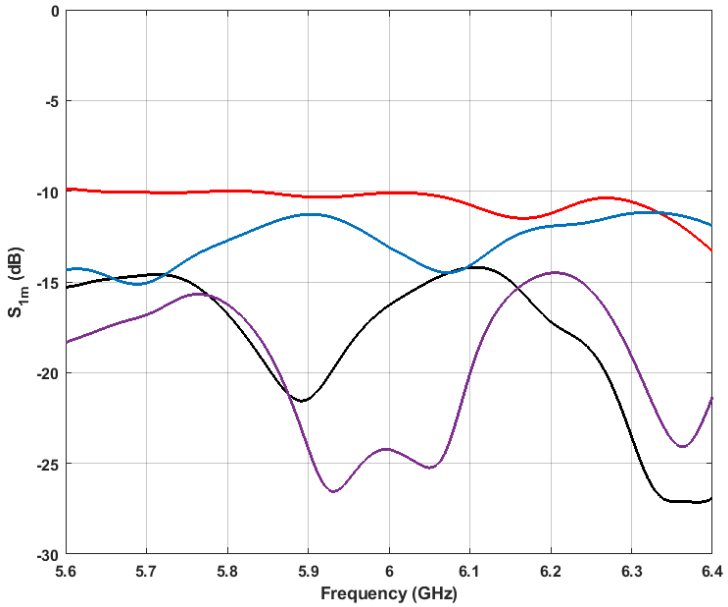

Figure 4.3-15: Magnitude of S_{11} (black), S_{12} (red), S_{13} (blue) and S_{14} (purple) versus frequency, for the shape-synthesized 4-port probe-fed antenna of Fig.4.3-1.

Table 4.3-3 : Beamforming weights of the shape synthesized DRA of Fig.4.3-1.

Port Index *p*	**Port Location** (x_p, y_p)	**Beamforming Weights** w_p
1	(10.3 mm, 6.0 mm)	$1.0 \angle 0°$
2	(10.3 mm, -6.0 mm)	$1.0 \angle 0°$
3	(21.5 mm, -6.0 mm)	$0.56 \angle 158°$
4	(21.5 mm, 6.0 mm)	$0.56 \angle 158°$
5	(32 mm, 27 mm)	$0.38 \angle 18°$
6	(32 mm, -27 mm)	$0.38 \angle 18°$

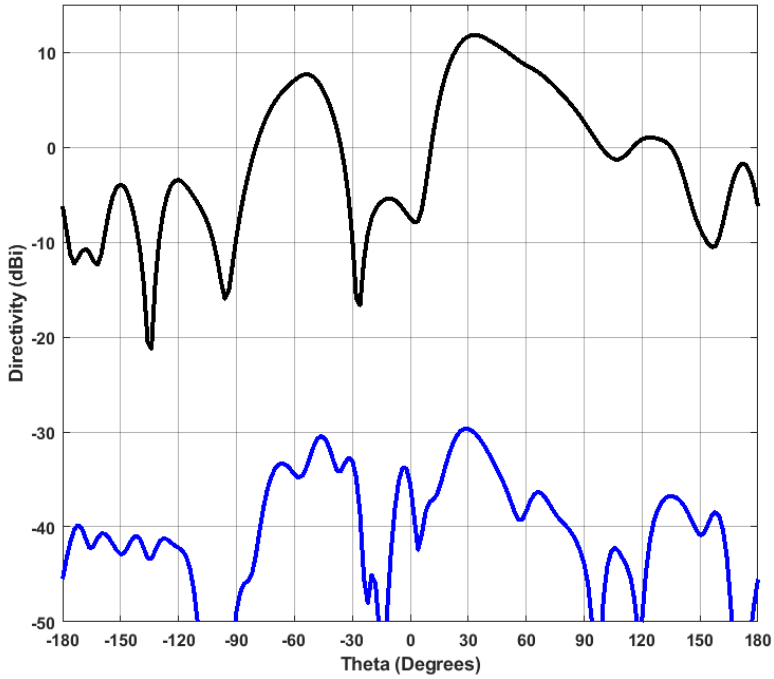

Figure 4.3-16: Co-polarized partial directivity pattern $D_\phi(\theta,0^\circ)$ shown as the black curve, and cross-polarized partial directivity $D_\theta(\theta,0^\circ)$ shown as the blue curve, at 6 GHz, in the xz-plane, of the shape synthesized DRA of Fig.4.3-1. Six probes are used to feed the DRA, resulting in $D_\phi(N_{CM},30^\circ,0^\circ)=11.66\,\text{dBi}$.

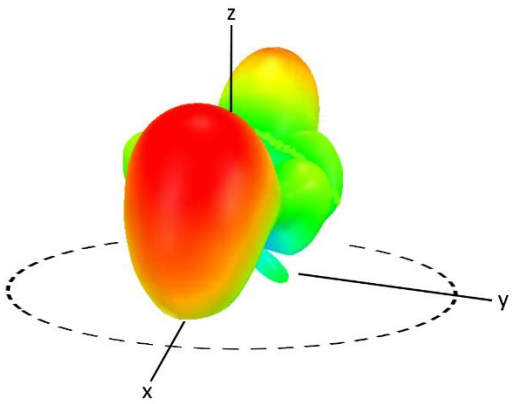

Figure 4.3-17: 3D depiction of the partial directivity $D_\phi(\theta,\phi)$ of the six-probe-fed shape synthesized DRA of Fig.4.3-1.

4.4 SHAPE SYNTHESIS OF A DRA FOR MAXIMIZATION OF OFF-BROADSIDE DIRECTIVITY $D_\theta(N_{CM}, \theta_s, \phi_s)$

4.4.1 Preliminary Remarks

The discussion in this section parallels that in Section 4.3, except that we apply the proposed shape synthesis method to synthesize a DRA that has its maximum partial directivity[104] $D_\theta(\theta, \phi)$ in the $(\theta, \phi) = (30^\circ, 0^\circ)$ direction. Thus, the descriptions will be more concisely written. The initial remarks in Section 4.3.1 apply here as well.

The objective function is as in Section 4.3-2, with $N_\alpha = 6$ but $D_p = D_\theta$ .The shaped DRA is now that in Fig.4.4-1; it is clearly different to that in Fig.4.3-1. The modal weighting coefficients and associated attainable directivity patterns obtained with $N_\alpha = 6$ (which produced the DRA in Fig.4.4-1) is that in Fig.4.4-2 and Fig.4.4-3, as well as Fig.4.4-4. The attainable D_θ is now 13.7dBi.

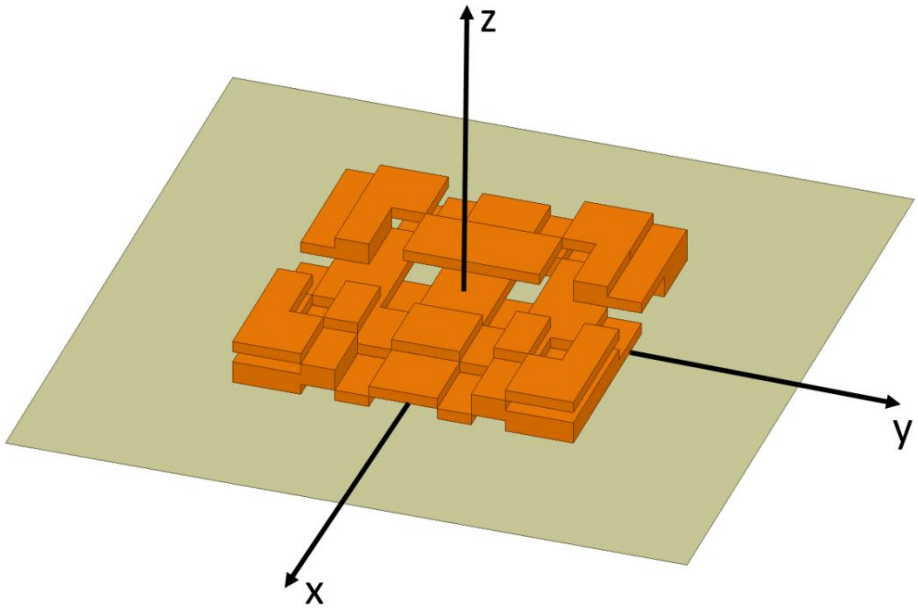

Figure 4.4-1: Geometry of the DRA shape synthesized with $N_\alpha = 6$ for maximum $D_\theta(N_{CM}, \theta_s, \phi_s)$ in direction $(\theta_s = 30^\circ, \phi_s = 0^\circ)$.

[104] As opposed to maximizing D_ϕ, as done in Section 4.3.

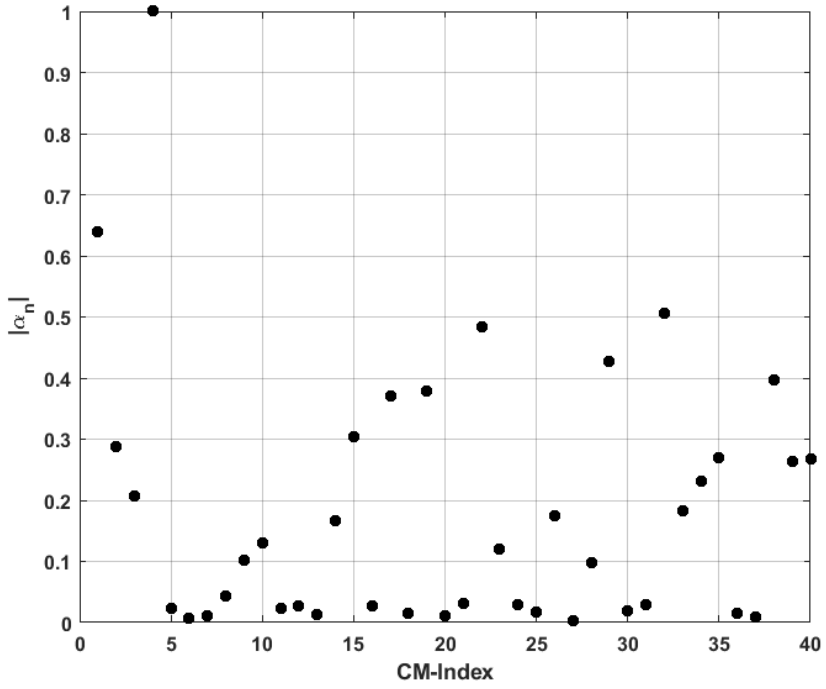

Figure 4.4-2: Modal weighting coefficient magnitudes for achieving the ideal available directivity for DRAs shape synthesized with $N_\alpha = 6$.

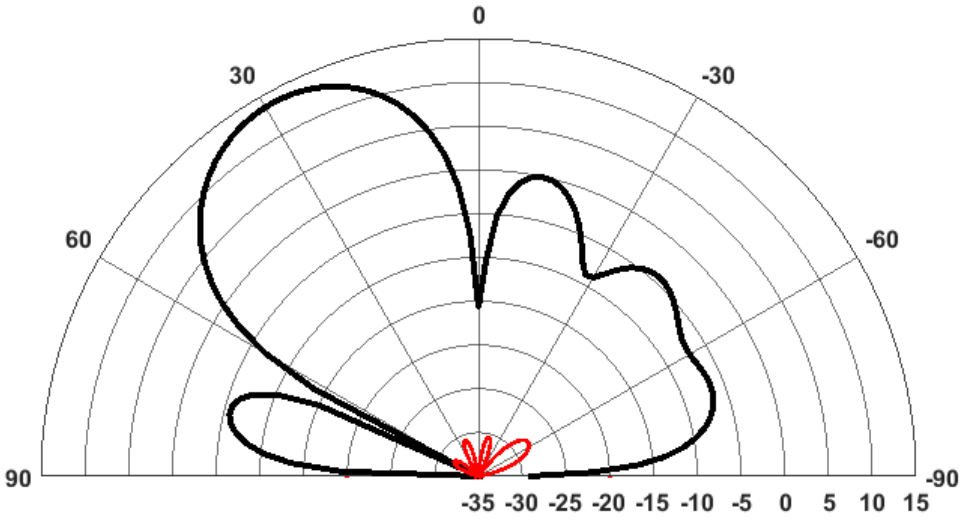

Figure 4.4-3: Attainable partial directivity pattern $D_\theta(N_{CM},\theta,0^\circ)$, at 6 GHz, in the xz-plane (black curve) for the DRA shape synthesized using $N_\alpha = 6$, with modal weights in Fig.4.4-2, and shown in Fig.4.4-1. The directivity D_θ in direction $(\theta_s,\phi_s)=(30^\circ,0^\circ)$ is 13.7dBi. Partial directivity pattern $D_\phi(N_{CM},\theta,0^\circ)$ in the same plane is shown as the red curve.

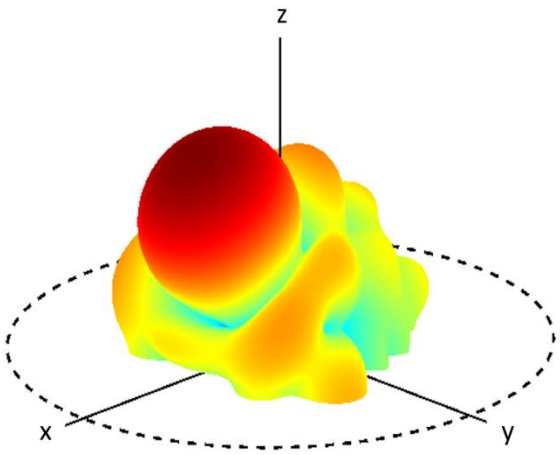

Figure 4.4-4: Attainable partial directivity 3D pattern representation $D_\theta(N_{CM},\theta,\phi)$, at 6 GHz, of the shape synthesized DRA shown in Fig.4.4-1, with a value of 13.7dBi in direction $(\theta_s,\phi_s)=(30^\circ,0^\circ)$.

4.4.2 Feed-Port Selection Considerations

An inspection of the $E_z(x,y,0^+)$ for the CMs with n ≤ Nα did not provide sufficiently sharp indications of where the feed mechanisms should be located. In such situations, it is preferable to examine[105] the superimposed form described by the function

$$F_{locz}(x,y,0^+)=\sum_{n=1}^{N_\alpha}\left|\alpha_n^{(s)}E_z^{(n)}(x,y,0^+)\right|^2 \qquad (4.4\text{-}1)$$

that is plotted in Fig.4.4-5.

4.4.3 Feed-Mechanism Design: Probe Feeds

Inspection of Fig.4.4-6 and Fig.4.4-7 shows that, using the four-probe-feed the achieved directivity pattern (with the maximum D_θ at 8.42 dBi) does not closely emulate the attainable ones in Fig.4.4-3 and Fig.4.4-4 (with the maximum attainable D_θ at 13.70 dBi). Indeed, glancing

[105] This can in fact always be used for this purpose. If used for the earlier examples it results in the same port locations obtained there from the fields of individual (as opposed to superimposed) CMs.

at these does not even evoke the thought of an antenna whose maximum D_θ has been designed to be in the said off-broadside direction. This points to the fact that the modal weighting coefficients of the CMs that offer the attainable directivity value are not being realized sufficiently closely when only four probes are used. In order to discount the effect of perturbing the structure shape (and hence its CMs) when inserting actual conducting probes as we have just done, the directivity performance was computed (using the shaped DRA and a finite groundplane) using infinitesimal electric dipoles as surrogates for the probes. The computed directivity pattern in the xz-plane is that shown in Fig.4.4-8 when two infinitesimal dipoles are placed at locations #1 and #2, four are placed at #1 through #4, and six at #1 through #6, the weights being optimized in each case in the usual way (namely that described in Section 3.5.2). Fig.4.4-8 shows that, once more as expected, $D_\theta(\theta,\phi)$ approaches that of an antenna with a directivity maximum in the off-broadside direction intended by the shape synthesis process, in the six-infinitesimal-dipole case being 9.8 dBi. The computed S-parameters of the four-probe-fed DRA are shown in Fig.4.4-9, but are unremarkable.

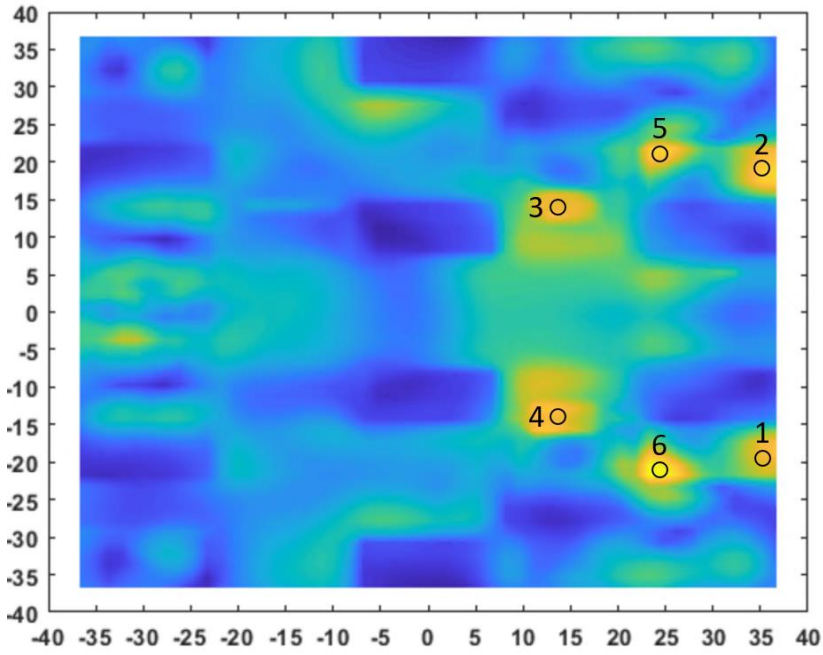

Figure 4.4-5: Sketch of the aggregate function $F_{locz}(x,y,0^+)$, below the DRA (shown in Fig.4.4-1) shape synthesized for maximum $D_\theta(N_{CM},30^\circ,0^\circ)$. Location of the peaks of $F_{locz}(x,y,0^+)$ have been numbered for easy reference.

Table 4.4-1 : Beamforming weights of the shape synthesized DRA shown in Fig.4.4-1.

Port Index *p*	Port Location (x_p, y_p)	Beamforming Weights w_p	Probe Height
1	(32.75mm,-17.25mm)	1.0 ∠-5°	4.225 mm
2	(32.75mm,17.25mm)	1.0 ∠-5°	4.225 mm
3	(14.25mm,14.25mm)	0.85 ∠0°	3.5 mm
4	(14.25mm,-14.25mm)	0.85∠0°	3.5 mm

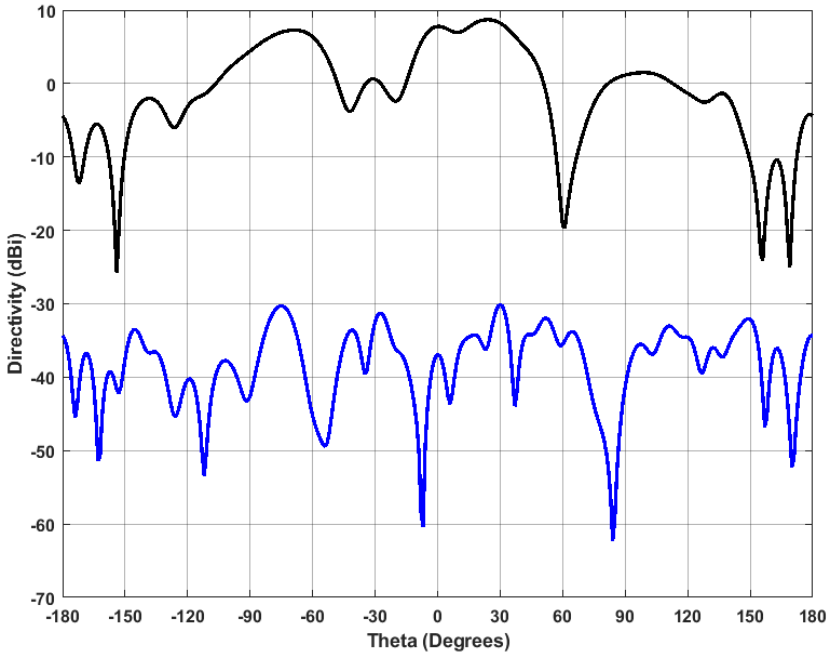

Figure 4.4-6: Co-polarized partial directivity pattern $D_\theta(\theta,\phi)$ shown as the black curve, and cross-polarized partial directivity $D_\phi(\theta,\phi)$ shown as the blue curve, at 6 GHz, in the xz-plane, of the shape synthesized DRA shown in Fig.4.4-1. Four probes are used to feed the DRA, resulting in $D_\theta(N_{CM}, 30^\circ, 0^\circ) = 8.42\,\text{dBi}$.

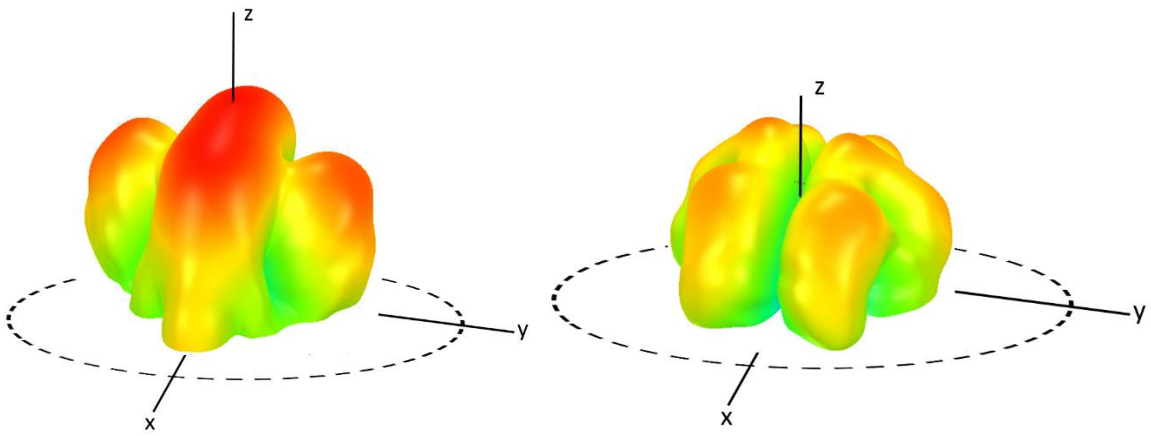

Figure 4.4-7: 3D depiction of the partial directivities $D_\theta(\theta,\phi)$ and $D_\phi(\theta,\phi)$, on the left and right respectively, of the four-probe-fed shape synthesized DRA in Fig.4.4-1.

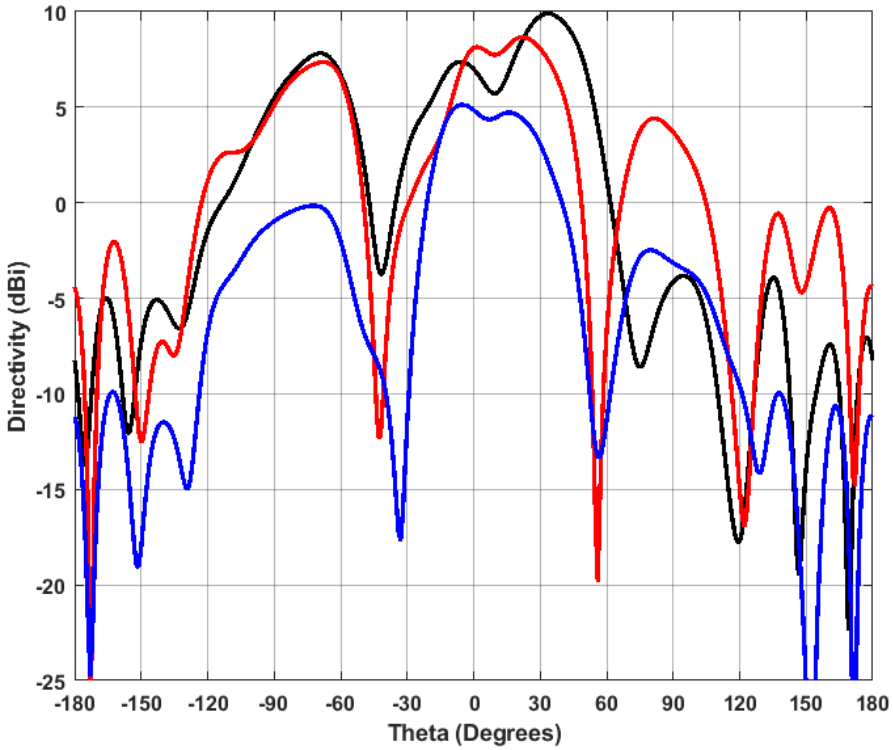

Figure 4.4-8: Co-polarized partial directivity pattern $D_\theta(\theta,\phi)$ at 6 GHz, in the xz-plane, of the shape synthesized DRA shown in Fig.4.4-1, driven by two (blue), four (red) and six (black) infinitesimal electric dipoles.

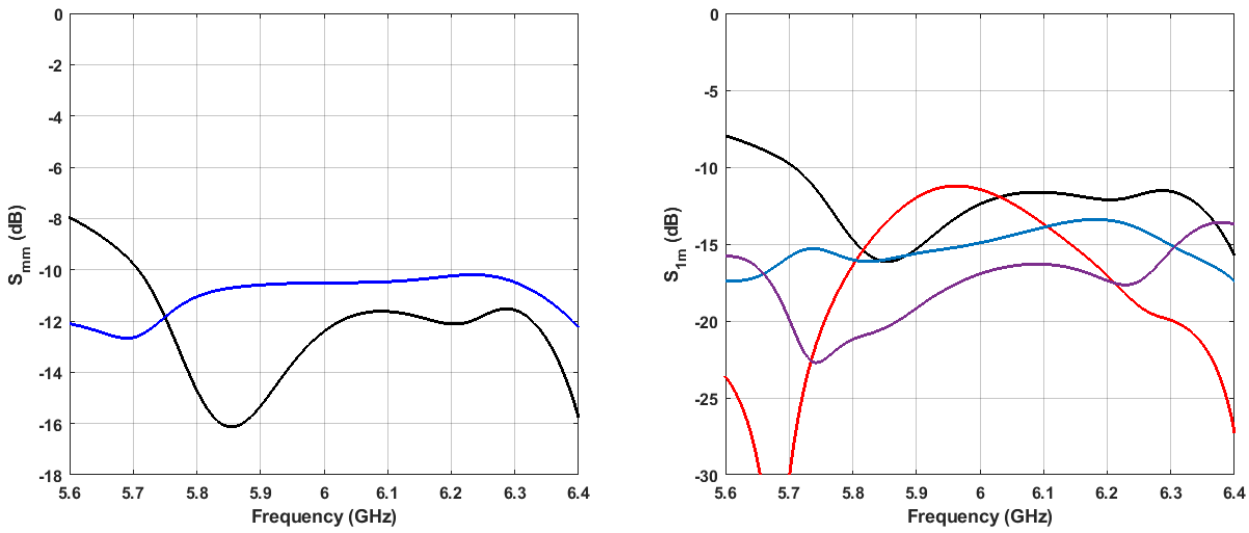

(a) **(b)**

Figure 4.4-9: (a). Magnitude of $S_{11} = S_{22}$ (black) and $S_{33} = S_{44}$ (blue) versus frequency, and (b). magnitude of S_{11} (black), S_{12} (red), S_{13} (blue) and S_{14} (purple) versus frequency, for the shape-synthesized four-probe-fed antenna shown in Fig.4.4-1.

4.4.4 Feed-Mechanism Design: Slot Feeds

Even with the six feed ports the actual off-broadside D_θ of Section 4.4.3 was not as close to the attainable value (found in Section 4.4.1) as for the other polarization case that was the subject of Section 4.3. It was seen earlier that one type of feed may provide a set of modal weighting coefficients closer to that of the CMs that offer the attainable directivity value, and thus we here examine the outcome when infinitesimal magnetic dipoles (emulating slots) are used with the shaped DRA of Fig.4.4-1. The relevant aggregate field distributions are now

$$F_{locx}(x,y,0^+) = \sum_{n=1}^{N_\alpha} \left| \alpha_n H_x^{(n)}(x,y,0^+) \right|^2 \qquad (4.4\text{-}2)$$

And

$$F_{locy}(x,y,0^+) = \sum_{n=1}^{N_\alpha} \left| \alpha_n H_y^{(n)}(x,y,0^+) \right|^2 \qquad (4.4\text{-}3)$$

as shown in Fig.4.4-10. We placed x-directed infinitesimal magnetic dipoles at locations #1 through #4, and a y-directed one at location #5, but the maximum D_θ in the required off-broadside direction was only 9dBi.

The θ-polarization under consideration in this section corresponds to the "hard-diffraction" case, whereas that in Section 4.3 (ϕ-polarization) is the "soft-diffraction" case, as regards diffraction from the edges of the finite-sized groundplane[106]. The groundplane thus influences the final radiation patterns more strongly in the present θ-polarization case. We remark that the use of sub-structure CMs would allow finite-groundplane effects to be taken into account during shaping and hence result in the maximized actual directivity approaching the maximized attainable directivity more closely.

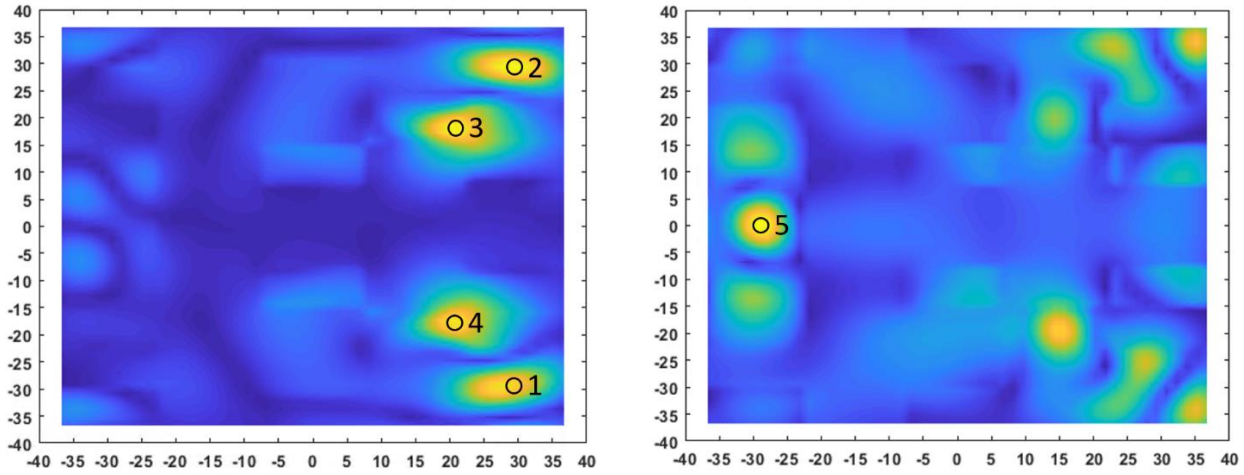

(a) **(b)**

Figure 4.4-10: Sketch of the aggregate functions (a). $F_{locx}(x,y,0^+)$**, and (b).** $F_{locy}(x,y,0^+)$**, below the DRA (shown in Fig.4.4-1) shape synthesized for maximum** $D_\theta(N_{CM},30^\circ,0^\circ)$**.**

[106] We are alerted to groundplane effects mentioned in Section 6.5 of [PETO 07].

4.5 CONCLUDING REMARKS

The goals of computational design and manufacturing for the not-too-distant future were stated in Section 1.1. Apart from such imposing aims, in the near future shape synthesis will be a useful addition to conventional design methods, even if only acting as a means of design-exploration initially. We indicated that this thesis hoped to contribute to these long- and short-term goals by developing an extended shape synthesis method, and associated tool, for DRAs. The first step was the development, in Chapter 3, of the complex computational electromagnetics-based shaping controller tool capable of performing the shape synthesis of multiport directivity-maximized DRAs. It was developed in such a way that different requirements could be accommodated by simply writing customized "plug-ins" that define a problem-specific shaping process through definition of objective functions that can involve the sorting and ranking of shapes "offered" by the main optimization algorithm as it iterates. Using this tool, the present Chapter 4 has demonstrated, for the first time, the shape synthesis of fixed-beam directivity-maximized DRAs, with the details of the feed mechanism(s) only needing to be specified at the post-shaping stage. It was seen how the actual directivity can approach the attainable directivity bound more closely as the permitted feed mechanism complexity increases; it is possible to perform such complexity trade-offs in the knowledge that (given the material form, size and property restrictions) the attainable directivity is the best one can do. If the desired attainable performance is not reached one can increase the size (e.g. height) or change the material properties, and then repeat the shape synthesis before bothering with the feeding details; the actual performance will not be better than the attainable performance. The outcomes of the shape synthesis process[107] were discussed for broadside and off-broadside fixed-beam cases, and indicated how shape synthesis can be used to deterministically design DRAs with specified polarizations. As far as the author is aware, off-broadside DRA of the kind in Section 4.3 and 4.4, with dictated polarization, have not yet been described elsewhere.

[107] Although the starting shapes were purposefully chosen so that the shape synthesis would yield low-profile enhanced-directivity DRAs, this need not be the case. The starting shape size and form, and material properties, are within the purview of the designer using the shape synthesis technique.

CHAPTER 5: SHAPE SYNTHESIS OF MULTIPORT STEERED-BEAM DIELECTRIC RESONATOR ANTENNAS

5.1 INTRODUCTORY REMARKS

Chapter 4 used the new shape synthesis procedure for directivity-optimized DRAs, developed and implemented in Chapter 3, for the design of fixed-beam directivity-optimized DRAs. The goal of the present chapter is to develop the "recipe" needed to apply the extended shape synthesis tool to the case of a steered-beam DRA with special spherical coverage requirements[108]. We use the word 'special" because they are not the usual ones where some minimum directivity over some field-of-view must be obtained (e.g. as in classical electronically steered arrays used in radar applications or wireless communications base stations which would be too complex or large or expensive for the application in mind). Instead, the coverage performance is characterized in a statistical sense via a cumulative distribution function (CDF) of the effective isotropic radiated power (EIRP), as described in Section 3.4. In order to determine the EIRP in any direction (θ_s, ϕ_s) we need to know the directivity of the antenna when it is steered to direction (θ_s, ϕ_s), the input power P_{in} to the antenna, and the radiation efficiency e_{rad} of the antenna. Knowledge of P_{in} is system-specific. Furthermore, for a DRA, the e_{rad} will largely depend on the specific material used, and will simply shift the CDF of the directivity by a constant factor. Thus we will perform the shape synthesis based on the CDF of the directivity only. Fig.3.4-1 from Section 3.4 can thus be re-drawn as depicted in Fig.5.1-1. The "perfect" curve would be a vertical line at $D^{\max}$; this would mean we are able to so alter the excitation of the shaped DRA that a directivity $D^{\max}$ is obtained in any direction[109] (θ_s, ϕ_s) on the upper hemisphere.

Section 5.2 covers all the steps in the shape synthesis of the steered-beam DRA, including interpretive discussion of the outcomes of an example application. Section 5.3 briefly indicates

[108] Antennas (albeit not DRAs, and not using shape synthesis) designed to satisfy the spherical coverage performance criterion based on the CDF of the EIRP have been reported, for example in [ZHAO 19], [HUAN 19] and [RODR 20], and typically consist of arrays of discrete printed conducting elements (e.g. dipoles; patches). [KIM 19] used CM analysis to study beam steering of a multiport antenna; however, his research was confined to PEC antennas and did not include any shape synthesis to improve performance.

[109] The "classical" case mentioned above.

how the process could be extended to include more than a single antenna working in tandem. Section 5.4 concludes the chapter, which represents the distillation of the perfected approach from many alternatives that we found to be less effective.

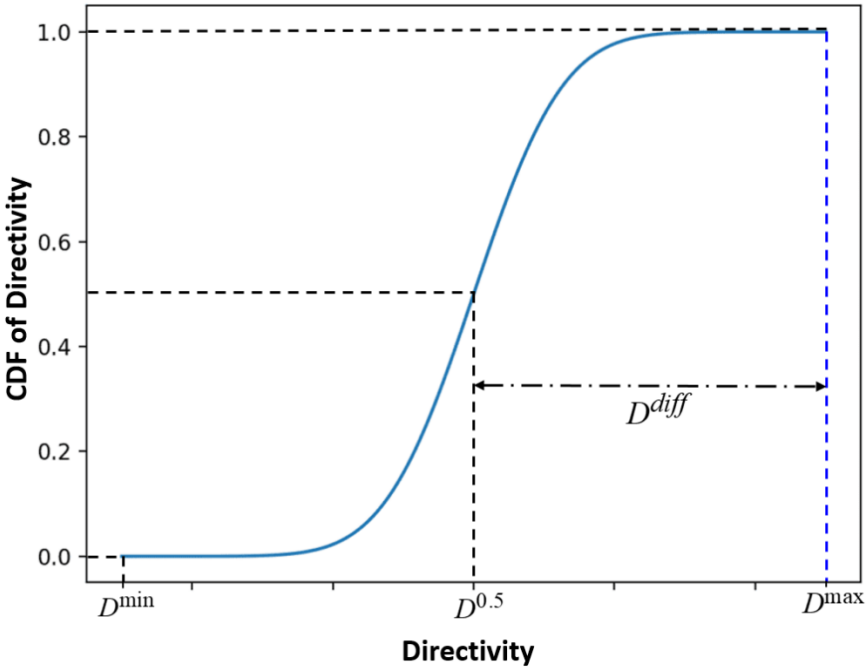

Figure 5.1-1: Reproduction of the curve in Fig.3.4-1, showing the CDF of the directivity instead of the CDF of the EIRP, of some steered-beam antenna.

5.2 SHAPE SYNTHESIS OF A DRA FOR MAXIMUM CDF OF THE DIRECTIVITY

5.2.1 Construction of a Suitable Objective Function, and Shaping Recipe

The goal is to achieve as favourable a CDF of the directivity as we are able, using a given dielectric object size (starting shape) and relative permittivity value. We need to define an objective function that will be used to rank each DRA shape in the population at each iteration of the GA algorithm as the shape synthesis process proceeds. This definition requires a number of steps, as will next be explained.

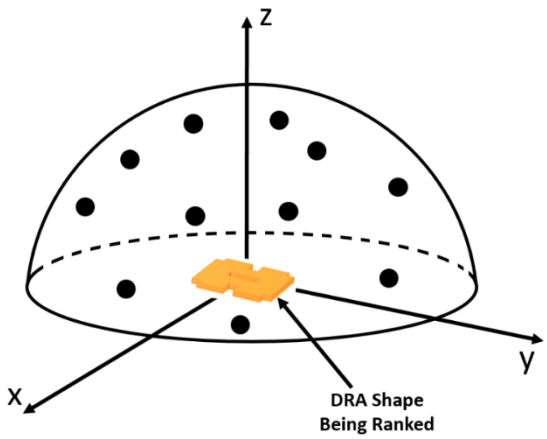

Figure 5.2-1: N_s sample directions (θ_s,ϕ_s) over the upper hemisphere[110] (at infinity) surrounding a DRA shape being ranked during the shape synthesis process.

In order to calculate the CDF of the attainable directivity for a given DRA shape, the attainable directivity is sampled in a finite number of directions[111] (θ_s, ϕ_s), $s = 1, 2, ..., N_s$, so that we will have a set of samples $D_a(\theta_s, \phi_s)$. We denote the smallest value of $D_a(\theta_s, \phi_s)$ by $D_a^{\min}$ and the largest value by $D_a^{\max}$. The CDF of the directivity is then approximated as

$$CDF\{D_{th}\} \approx \frac{\text{No. of directions in which } D_a(\theta_s, \phi_s) \le D_{th}}{N_s} \qquad (5.2\text{-}1)$$

This gives the probability that the attainable directivity will be greater than a value D_{th}, for $D_a^{\min} \le D_{th} \le D_a^{\max}$. We can use this to "read off" the value of $D_a^{0.5}$.

[110] As in Chapter 4, for reasons provided in Section 3.6.3 and Section 3.8, the DRA is considered to be positioned on an infinite groundplane; hence the consideration of only the upper hemisphere during shaping. As before, once shaping has been completed, the performance of the driven antenna is computed using a finite groundplane.

[111] We always ensure that these are spread out fairly evenly over the upper hemisphere, and not unduly concentrated over any part of it. We also increase the value of N_s until it is certain a sufficient number of sample points is being used.

The attainable directivity $D_a(\theta_s,\phi_s)$ for each sample direction (θ_s,ϕ_s), for the particular DRA shape, is obtained by using the weight vector $[\mathcal{W}^{(s)}]$ that maximizes[112]

$$D_a(\theta_s,\phi_s)=\frac{2\pi}{\eta_o}\frac{[\mathcal{W}^{(s)}]^H[\mathrm{A}(\theta_s,\phi_s)][\mathcal{W}^{(s)}]}{[\mathcal{W}^{(s)}]^H[\mathrm{B}][\mathcal{W}^{(s)}]} \tag{5.2-2}$$

These $[\mathcal{W}^{(s)}]$ are determined via a sub-optimization using the QFA approach devised in Section 3.2, with

$$[\mathcal{W}^{(s)}]=\left[\alpha_1^{(s)} \quad \alpha_2^{(s)} \quad \cdot \quad \cdot \quad \alpha_{N_{CM}}^{(s)}\right]^T \tag{5.2-3}$$

The objective function value for the particular DRA shape, with u_1 and u_2 user-assigned weight factors, is then found as

$$F_{obj}=F_\alpha(N_{CM},N_\alpha)\left[u_1\,CDF\left\{D_{\mathrm{a}}^{0.5}\right\}+u_2\,CDF\left\{D_{\mathrm{a}}^{\max}\right\}\right] \tag{5.2-4}$$

In other words, the CDF values are "penalized" by F_α if they require too significant a contribution by the higher-order CMs to achieve the said values. We have used $u_1=0.25$ and $u_1=0.75$ so that $u_1+u_2=1$, because we want the terms $u_1\,CDF\left\{D_{\mathrm{a}}^{0.5}\right\}$ and $u_2\,CDF\left\{D_{\mathrm{a}}^{\max}\right\}$ to be roughly the same values so that the optimizer places almost the same emphasis on these equally important CDF quantities. At the end of the shaping process, the "unpenalized" CDF of the directivity describes the performance of the steered-beam shape synthesized DRA. It should be emphasized that $D_a(\theta_s,\phi_s)$ is the attainable directivity in the particular directions, in the sense that if it is possible to realize the $[\mathcal{W}^{(s)}]$ values, then such directivities can be attained. In practice we have to excite the shaped DRA with feed mechanisms located at a finite number of ports, and then the actual directivity values $D(\theta_s,\phi_s)<D_a(\theta_s,\phi_s)$ will be achieved; the CDF of the directivity $D(\theta_s,\phi_s)$ is reported as the "final" performance of the shaped DRA.

[112] We remind the reader that these column vectors $[\mathcal{W}^{(s)}]$ are those of Section 3.2, that have N_{CM} elements, and not $[W^{(s)}]$ that have N_p elements.

5.2.2 Shape Synthesis Outcome

The starting shape (above an infinite groundplane) and size are again the same as shown in Fig.4.2-3, and the operating frequency is 6 GHz once more. The objective function is that defined in Section 5.2.1, with $N_\alpha = 14$. The latter is a much larger value than selected for the fixed-beam cases in Chapter 4. The reason is that more CMs need to be excitable if we are to be able to steer the pattern maximum in a way that many directions over the upper hemisphere can be "serviced" with an acceptable directivity. Quadrantal symmetry was imposed (so that DoF = 100); this seemed reasonable because we wish to "cover" the complete upper hemisphere. The outcome of the shape synthesis process is the DRA geometry shown in Fig.5.2-2.

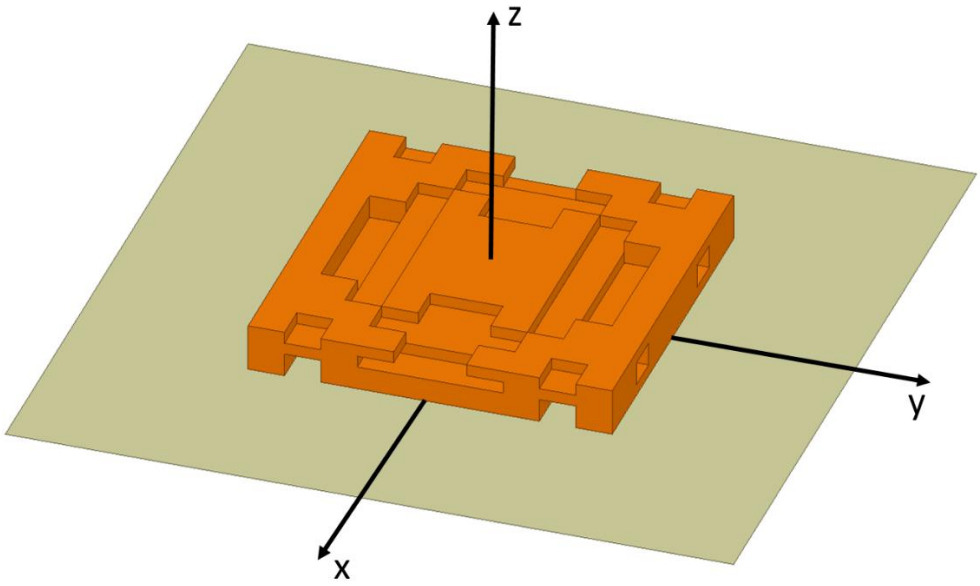

Figure 5.2-2: Geometry of the DRA shape synthesized with $N_\alpha = 14$ for maximum CDF of the directivity over the upper hemisphere.

The CDF of the attainable directivity (for the shaped DRA geometry shown in Fig.5.2-2) is plotted[113] as curve (a) in Fig.5.2-3. It is clear that the shape synthesis process is able to produce a CDF curve, namely (a), that is close to vertical[114]. Curve (b) is what we get if we do not impose

[113] Fig.5.2-3 shows several curves, identified as (a) though (f), and will be referred to several times in the discussion in this chapter. All curves have been plotted on the same graph to facilitate easy comparison. We ask the reader to attend to a particular curve only one it has been referred to in the text.
[114] We noted in Section 5.1 that a vertical CDF of directivity curve is the perfect situation.

the restraint $N_\alpha = 14$ but instead loosen this to $N_\alpha = N_{CM}$, using which the shape synthesis process produces a geometry different to that in Fig.5.2-2. Curve (a) is slightly "lower" than (b) because of the restraint imposed when setting $N_\alpha < N_{CM}$ in order to obtain a shape that is more easily excited in practice. The reason is illustrated in Fig.5.2-4, which presents the distribution of $D_a(\theta_s, \phi_s)$ values over the upper hemisphere. The more non-superdirective CMs allowed to contribute to the antenna performance the more directions in which $D_a(\theta_s, \phi_s)$ is high. We observe that the almost "classical" coverage referred to in Section 5.1 is in fact evident in Fig.5.2-4, and is reflected in the near-vertical CDF curves (a) and (b) in Fig.5.2-2. We next proceed to the selection of the feed ports.

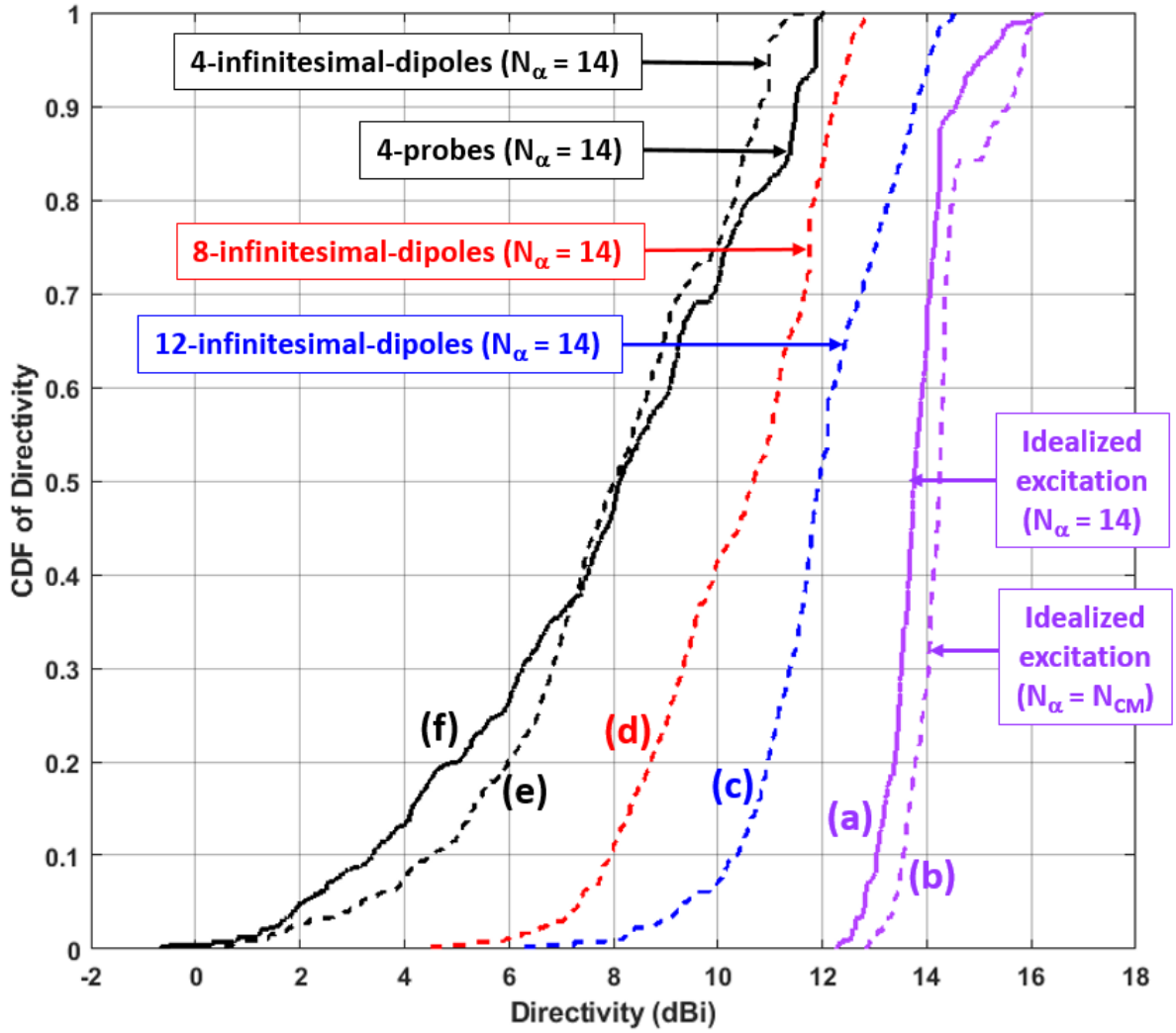

Figure 5.2-3: Computed CDF of the directivity at the shaping frequency 6 GHz.

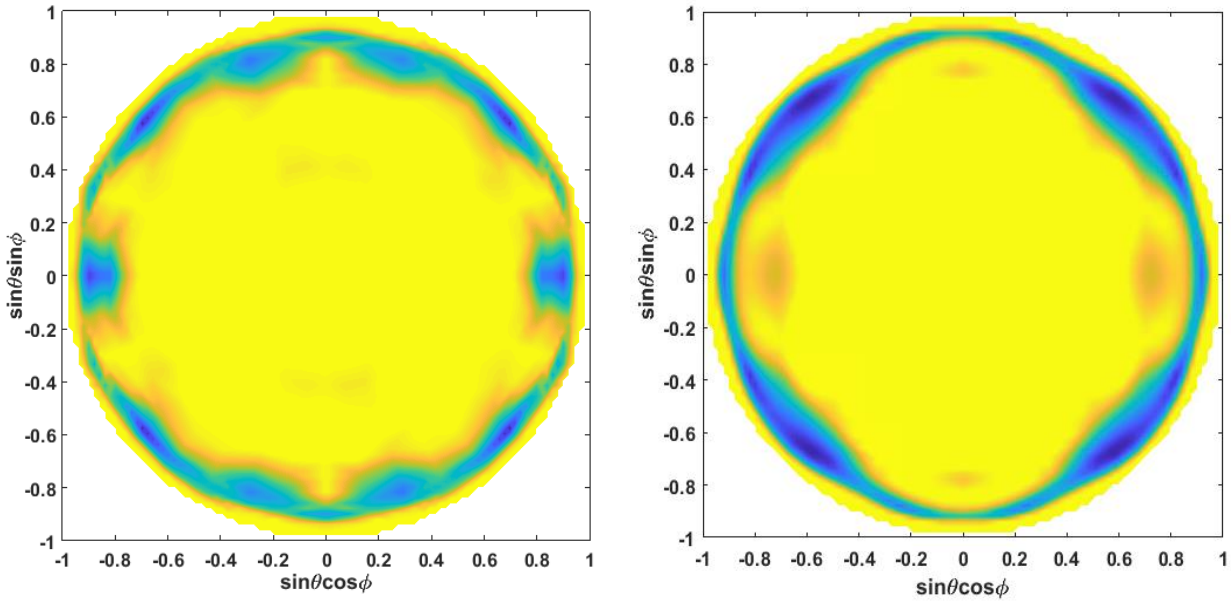

Figure 5.2-4: Colour plot of $D_a(\theta_s,\phi_s)$ for the DRA shape synthesized using $N_\alpha = N_{CM}$ (left) and $N_\alpha = 14$ (right). Yellow represents a higher value of $D_a(\theta_s,\phi_s)$ than blue.

5.2.3 Feed-Port Selection Considerations

In this steered-beam case different CMs need to be excited for different directions (θ_s,ϕ_s), and so the selection of the best port locations differs from that for the fixed-beam cases in Chapter 4. We therefore form the function[115]

$$F_{loc}(x,y,0^+) = \sum_{s=1}^{N_s}\left\{\sum_{n=1}^{N_\alpha}\left|\alpha_n^{(s)}E_z^{(n)}(x,y,0^+)\right|^2\right\} \qquad (5.2\text{-}5)$$

This sums the normal components of the electric field of each of the contributory CMs at the base of the shaped DRA, but scaled by the CM weighting coefficients $[\mathcal{W}^{(s)}]$ for each of the N_s directions that have been used to determine the CDF of the attainable directivity. This is shown in Fig.5.2-5 for the DRA in Fig.5.2-2. The peaks of $\left|F_{loc}(x,y,0^+)\right|$ have been identified as (x_p,y_p) for $p=1,2,\ldots$, numbered in order of increasing $\left|F_{loc}(x_p,y_p,0^+)\right|$ values.

[115] A similar form would be used, in terms of the tangential magnetic field, if the intention was to excite the shaped steered-beam DRA using slots. Here we will consider probe excitation only.

A full-wave driven model of the shaped DRA, with a finite-sized groundplane, is constructed[116]. It is first used to assess the performance using infinitesimal electric dipoles (normal to the groundplane) as the excitation. We know from Chapter 4 that these provide a good indication of what actual probe feeds will do. Infinitesimal electric dipoles are located at the N_p ports[117] numbered in Fig.5.2-5, and detailed in Table 5.2-1. The weights[118] $[W^{(s)}]$ of the N_p ports are optimized, as described in Section 3.5.2, in order to maximize[119] $F_{obj} = CDF\left\{D^{0.5}\right\} + CDF\left\{D^{\max}\right\}$. In other words, the far-zone fields of the driven DRA on the finite groundplane are computed for each infinitesimal dipole in turn (with the others not excited), and superposition of these fields then used when several dipoles are excited.

The resulting computed CDF of the actual directivity performance, based on $D(\theta_s, \phi_s)$, is shown as curves (c), (d) and (e) in Fig.5.2-3, for $N_p = 4$, then $N_p = 8$, and finally $N_p = 12$ ports, respectively. The associated $D(\theta_s, \phi_s)$ distributions are those in Fig.5.2-6; it is clear that there is no longer the "classical" coverage referred to in Section 5.1. As expected, the lower the number of ports the further the CDF of the directivity curve of the port-excited DRA departs from that based on $D_a(\theta_s, \phi_s)$. The larger the number of ports (value of N_p) utilized the closer it is to effectively obtain $[\mathcal{W}^{(s)}]$ values that provide the upper bound, namely the CDF of the attainable directivity. In order to improve the CDF of the directivity we might need to try an electrically larger starting shape, or perhaps allow inhomogeneous material (although this would require an improved volume-integral-equation based CM solver, as discussed in Section 3.6.5).

[116] As described in Section 2.4.

[117] When using infinitesimal dipoles there are no physical ports present, but we will for simplicity nevertheless still refer to them as "ports".

[118] Recall that there are N_S such sets for a given antenna.

[119] Observe that this uses the actual *D* (namely that obtained from a driven problem), and not the attainable D_a (that determined using the CM weighting coefficients).

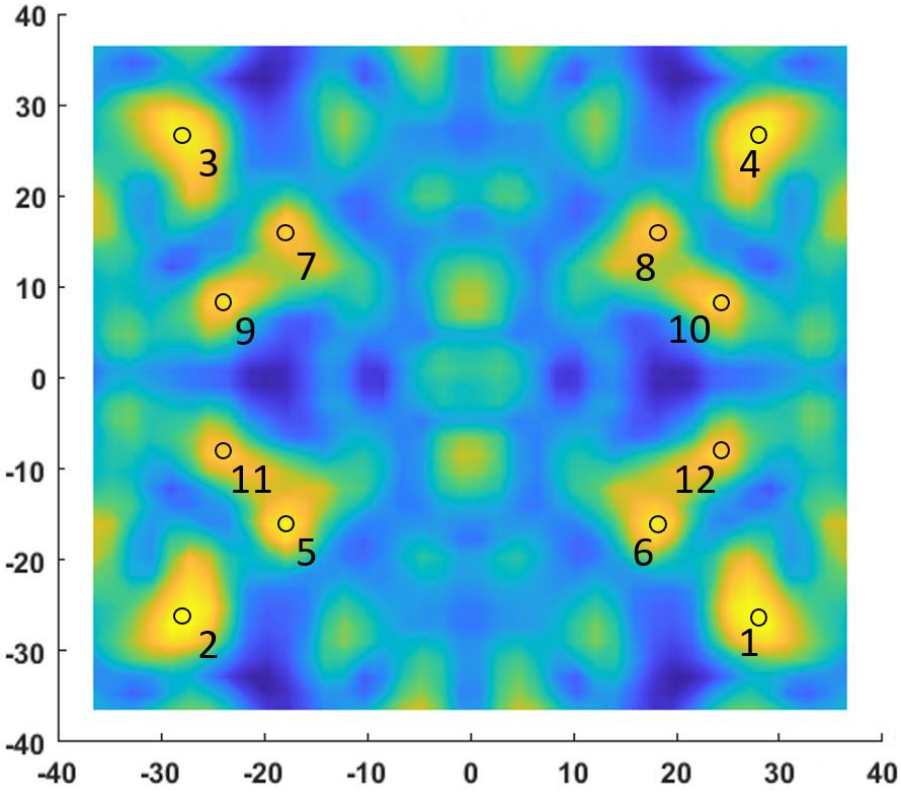

Figure 5.2-5: Colour plot of $\left|F_{loc}(x,y,0^{+})\right|$ below the 75mm x 75mm shaped DRA.

Table 5.2-1 : Locations of the Peak Values of $\left|F_{loc}(x,y,0^{+})\right|$ for the shape synthesized DRA.

Port Index *p*	**Peak Location (x_p, y_p)**
1	(27.19 mm, -25.31 mm)
2	(-27.19 mm, -25.31 mm)
3	(-27.19 mm, 25.31 mm)
4	(27.19 mm, 25.31 mm)
5	(-17.81 mm, -15.94 mm)
6	(17.81 mm, -15.94 mm)
7	(-17.81 mm, 15.94 mm)
8	(17.81 mm, 15.94 mm)
9	(-23.44 mm, 8.44 mm)
10	(23.44 mm, 8.44 mm)
11	(-23.44 mm, -8.44 mm)
12	(23.44 mm, -8.44 mm)

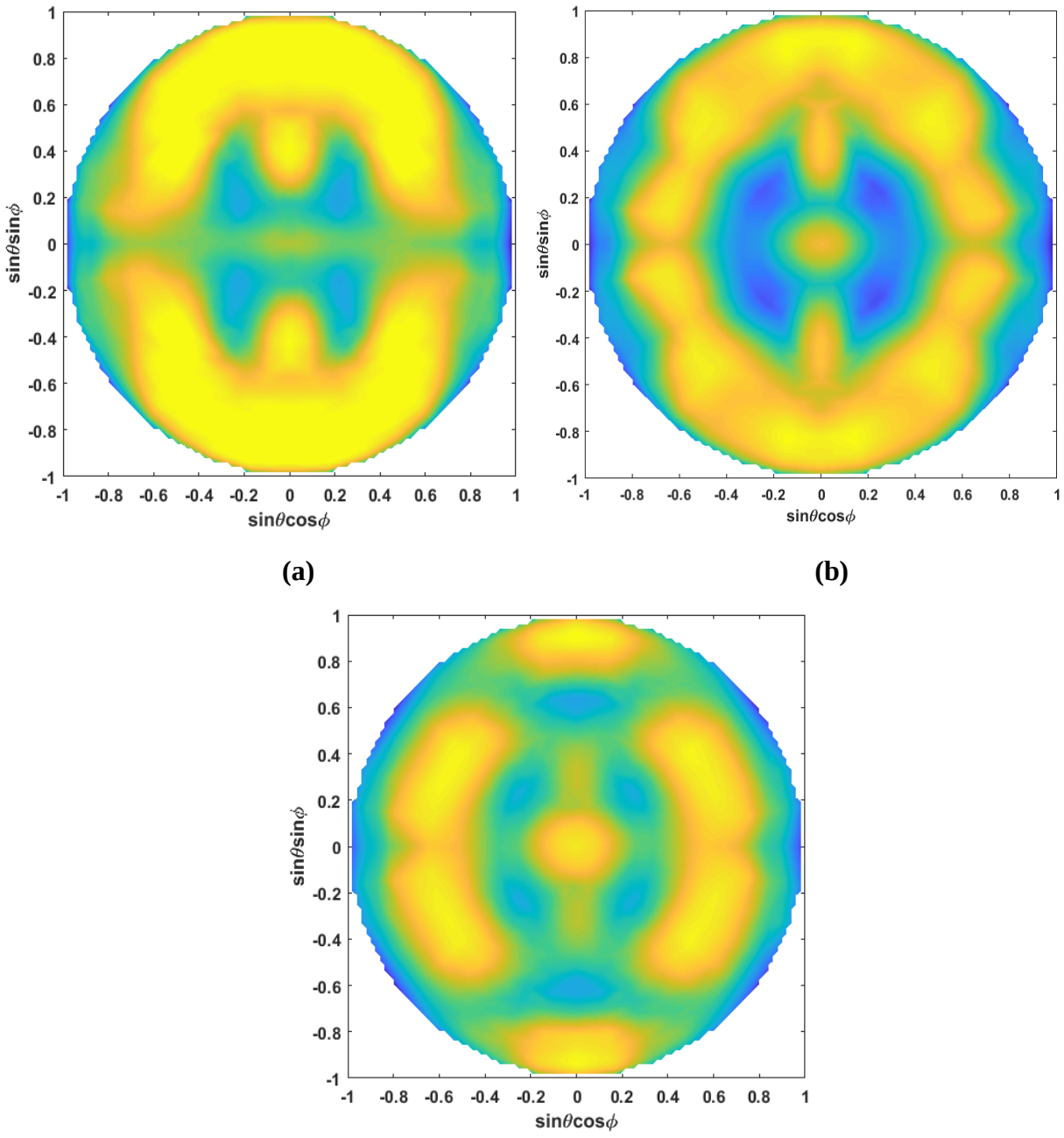

(a) **(b)**

(c)

Figure 5.2-6: Colour plot of $D(\theta_s, \phi_s)$ for the DRA shape synthesized using $N_\alpha = 14$, and excited by (a). 12 infinitesimal electric dipoles, (b). 8 infinitesimal electric dipoles, and (c). 4 infinitesimal electric dipoles.

5.2.4 Feed-Mechanism Design: Four Probes

We next used four probe feeds at the $p = 1, 2, 3, 4$ locations in Table 5.2-1, and optimized[120] their weights $[W^{(s)}] = [w_1^{(s)}, w_2^{(s)}, w_3^{(s)}, w_4^{(s)}]^T$ for best $F_{obj} = CDF\left\{D^{0.5}\right\} + CDF\left\{D^{\max}\right\}$. The resultant spherical coverage performance is represented by curve (f) in Fig.5.2-3, and the distribution in Fig.5.2-7(a). All the CDF of directivity results thus far have assumed an "∞-bit" phase shifter. The above procedure to find the weights $[W^{(s)}] = [w_1^{(s)}, w_2^{(s)}, w_3^{(s)}, w_4^{(s)}]^T$ for the four-probe-fed shaped DRA was repeated under the assumption of a 6-bit phase shifter, as outlined in the second part of Section 3.5.2. For the sake of interest, we show the resulting selection of phase values in Fig.5.2-8. Fig.5.2-9 shows that the CDF of the directivity for the ∞-bit and 6-bit assumptions, and is encouraging in that little degradation takes place when using the more practical 6-bit assumption, as also confirmed by Fig.5.2-7(b). Finally, Fig.5.2-10 once again reveals, as already noted in Section 3.6.2 and Section 4.2.9, the necessity for the CM analyses of dielectric objects that could be reliably done over a band of frequencies[121] and not only at a single frequency.

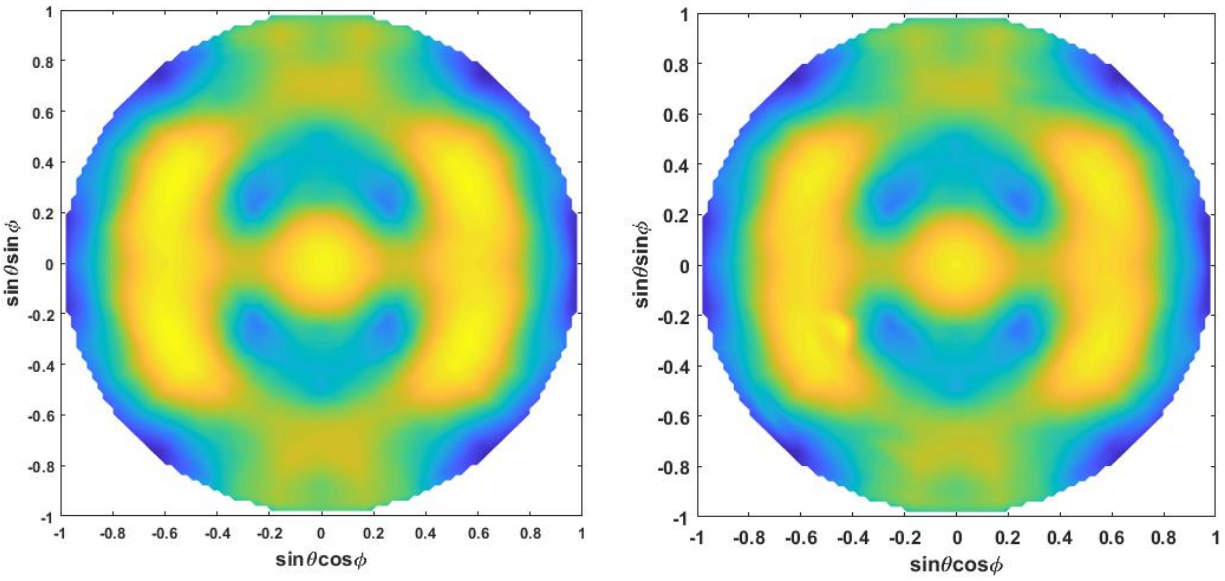

Figure 5.2-7: Colour plot of $D(\theta_s, \phi_s)$ for the DRA shape synthesized using $N_\alpha = 14$, and excited by (a). 4 probes, with any phase in the range [0°, 360°] permitted for the probe weights, and (b). 4 probes with only 64 discrete phases (as permitted by a 6-bit phase shifter) permitted for the probe weights.

[120] As described in the first part of Section 3.5.2.
[121] Namely with correct mode tracking.

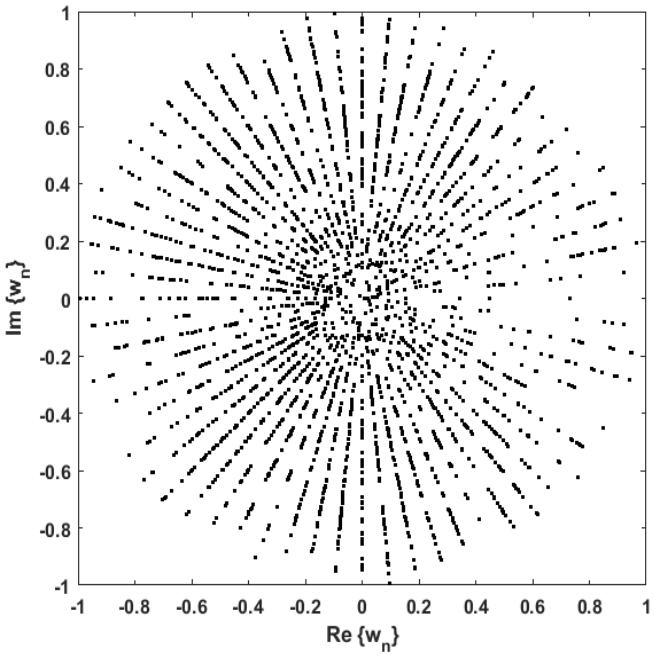

Figure 5.2-8: Collection of N_S computed complex weights when the phase of the weights of the four probes can only take on the 64 discrete values permitted by a 6-bit phase shifter.

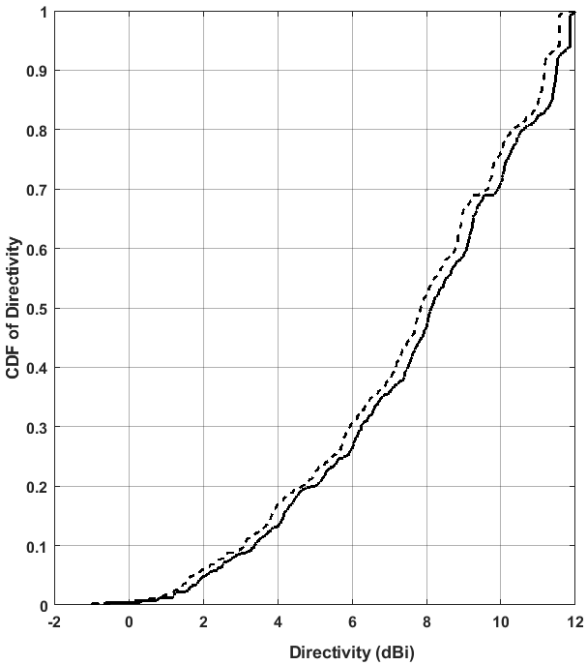

Figure 5.2-9: Computed CDF of the directivity at the shaping frequency 6 GHz. The solid curve (——) is that when the DRA is fed by four probes, with any phase in the range [0°, 360°] permitted for the probe weights, and is the same as curve (f) in Fig.5.2-3. The dashed curve (- - - -) is that when the phase of the weights of the four probes can only take on the 64 discrete values permitted by a 6-bit phase shifter.

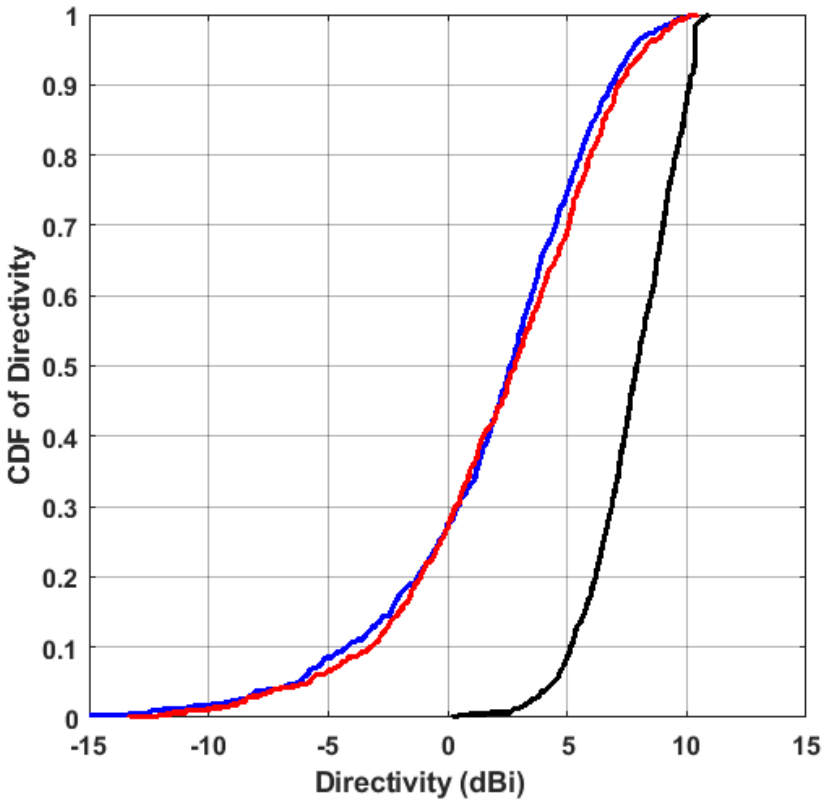

Figure 5.2-10: Computed CDF of the directivity at the shaping frequency 6 GHz (black line), and at 5.8 GHz (red line) and 6.2 GHz (blue line), when the shaped DRA is fed by four probes whose weights were determined at 6 GHz).

5.3 THE USE OF MORE THAN ONE SUB-ANTENNA

In order to satisfy spherical coverage performance that can perhaps not be satisfied by a single antenna[122], more than a single DRA located at different locations on a platform, such as the top and two sides might be needed, as illustrated in Fig.5.3-1 in the present context. The requirement would be that such sub-antennas together must provide the CDF of directivity performance needed for a successful wireless communications link. It is of course the CDF of the combination of the DRA sub-antennas that is of importance, and so these can be simultaneously, but separately, shaped and the CDF of the directivity evaluated for their combination. Alternatively, the sub-antennas can, during shaping, considered to be of the same shape, and the CDF evaluated from

[122] This has been suggested in [ZHAO 19], albeit not in the context of shape synthesis, and not for DRAs (which have on fact not yet been considered for steered-beam spherical coverage by others.

their combined pattern performance. Another approach could be to divide the coverage region into (possibly overlapping) sectors, each to be "serviced" by a relevant sub-antenna, with the CDF being defined over the appropriate sector during independent shaping of a sub-antenna. At any rate, the shaping procedure developed in this chapter could be used, if a sub-structure CM analysis capability were to become available, as discussed in Section 3.6.3.

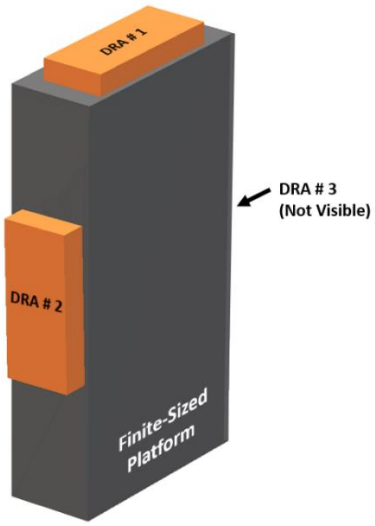

Figure 5.3-1: A finite platform with three sub-antennas to be shaped for combined contributions for spherical coverage.

5.4 CONCLUSIONS

A novel recipe for the shape synthesis of a DRA for maximization of its CDF-of-directivity has been devised and applied in an illustrative example[123]. Such shape synthesis has not yet been reported in the literature for any antenna type. It was shown how, at the post-shaping stage, the CM information can be used to locate the feed ports, and how the actual CDF-of-directivity of the port-excited DRA can increasingly closely approach the attainable CDF-of-directivity, by using more excitation ports. This adds clarity to the trade-offs that exist when the DRA has physical size, material parameter, and other constraints imposed at the start. This was achieved by customizing the shaping recipe and objective function as new "plug-ins" to the shaping controller developed in Chapter 3.

[123] Recall that the fact that the feed mechanism details need not be selected prior to shaping allows the shape synthesis to provide a true "best attainable case".

CHAPTER 6: GENERAL CONCLUSIONS

The original contributions to the overall subject of the shape synthesis of dielectric resonator antennas presented in this thesis are as follows (extracted from the concluding sections of Chapters 3, 4 and 5) :

- A shape synthesis method (of a shape-first/feed-next kind) has been developed to design directivity-maximized dielectric resonator antennas for the first time. The shape-first/feed-next shape synthesis approach for directivity-maximized performance has not been previously described for any antenna type, and thus is new in general terms also. It was previously only applicable to electrically-small antenna structures that are single-mode in the sense that the lowest-order characteristic mode entirely determines the antenna performance. The extension developed here permits the use of several characteristic modes, known to be needed for enhanced directivity.
- It has been demonstrated that, one is now able to deterministically design fixed-beam directivity-maximized DRAs with prescribed polarization and maximum-directivity direction, or even steerable-beam DRAs with directivity-maximized spherical coverage requirements. It is no longer necessary to use prescribed shapes and then try to do as well as one can by adjusting their feature dimensions, or have to the devise new near-canonical shapes on a design-by-design basis. It can already act as a useful addition to conventional design approaches, but also lays a piece of the groundwork for incorporating DRA design in the computational design and manufacturing framework expected in the future.
- Although the development of the directivity-maximized shaping tool was in essence a means to an end, it represents a contribution of value. The shaping controller has been developed in MATLAB, and the optimization algorithm and full-wave computational electromagnetics modeller software are available commercially. Thus, the tool need not remain “in-house” but could be used by others.

Preliminary portions of the work have been presented in two conference papers:

- **M. Nassor**, et al., "Some numerical experiments on enhanced-directivity dielectric resonator antennas”, IEEE International Antennas and Propagation Symposium Digest, 2021.
- **M. Nassor**, et al., "On the inverse design of dielectric resonator antenna structures for beam-steering", 15th European Conference on Antennas and Propagation (EuCAP), 2021.

There remain some issues/cases whose investigation in the future would prove useful. The shape synthesis method relies on an ability to compute the characteristic modes of the structure as it is being shaped. It has been recalled at various points in the text that future lifting of the present

limitations on the characteristic mode analysis[124] in computational electromagnetics engines would allow the developed shape synthesis to be improved, without changing the overall approach. The needed work on such augmentation of characteristic mode theory (albeit not its use in shape synthesis) has in fact been completed by researchers over the last four years. Once it finds its way into commercial computational electromagnetics engines, the author's shape synthesis method could be relatively easily enhanced in the following ways:

■ The availability of reliable tracking capabilities (noted in Section 3.6.2) for the characteristic modes of dielectric objects would permit the shape synthesis to be applied over a band of frequencies, and thus improve the bandwidth properties of the shaped DRAs.

■ The availability of a sub-structure characteristic mode ability (noted in Section 3.6.3) would allow the shape synthesis method (shaping for directivity maximization) to be performed using finite-sized groundplanes, or even more complex platforms, and with a wider choice of post-shaping feeding mechanisms. The shaped DRAs in wireless devices would always have to operate in the presence of other "mechanical" conducting and penetrable objects [COLL 19]; if coupling to these objects is going to add some loss the designer might as well exploit such objects when shaping the DRA for maximum attainable performance. The designer could craft the performance of dielectric resonator antennas in complex environments, an act compatible with the future goals of computational design and manufacturing goals. No doubt commercial computational electromagnetics codes will eventually be upgraded to have a sub-structure characteristic mode capability.

■ The availability of fast volume integral equation methods (noted in Section 3.6.5) would permit the use of piecewise homogeneous DRAs.

■ The quadratic form approach was a key contributor to the realization of the shape synthesis method. As noted in Section 3.2, sidelobe level and other pattern constraints, could be incorporated into it, further supplementing the control the designer is able to achieve in the DRA shape synthesis process.

[124] Discussed in Section 3.6.

REFERENCES

[ALAK 21] A.Alakhras and D.A.McNamara, “The shape synthesis of 3D electrically-small conducting surface antennas”, Electronics Letters, Vol.57, No.8, pp.311-313, April 2021.

[ALAN 23] M.D.Alanazi, “A review of dielectric resonator antennas at mm-wave band”, Eng, vol.4, pp.843-856, 2023.

[ALJA 18] A.Aljanah and D.A.McNamara, “Shape synthesis of 3-layer transmitarray elements”, IEEE Int. Antennas & Propagat. Symp. Digest, Boston, USA, July 2018. 21.

[ALJA 18] A. Aljanah and D. A. McNamara, "Shape Synthesis of 3-Layer Transmitarray Elements," 2018 IEEE International Symposium on Antennas and Propagation & USNC/URSI National Radio Science Meeting, 2018, pp. 257-258.

[ALJA 21] A.Aljanah, E.Almajali and D.A.McNamara, “Some observed outcomes of the shape synthesis of dual-band transmitarray elements”, IEEE Int. Antennas & Propagat. Symp. Digest, Singapore, December 2021.

[ALRO 14a] H. Alroughani, J. L. T. Ethier and D. A. McNamara, "Observations on computational outcomes for the characteristic modes of dielectric objects," IEEE Antennas and Propagation Society International Symposium, pp. 844-845, 2014.

[ALRO 14b] H. Alroughani, J. L. T. Ethier and D. A. McNamara, "On the classification of characteristic modes, and the extension of sub-structure modes to include penetrable material", International Conference on Electromagnetics in Advanced Applications (ICEAA), pp. 159-162, 2014.

[ALRO 16] H.Alroughani, J.Ethier and D.A.McNamara, “On the orthogonality properties of sub-structure characteristic modes”, Microwave & Optical Technology Letters, Vol.58, No.2, pp.481-486, Feb.2016.

[ALRO 17] H. Alroughani, "An enhanced algorithm in tracking characteristic modes of dielectric objects," 2017 International Applied Computational Electromagnetics Society Symposium - Italy (ACES), Firenze, Italy, 2017.

[ALRO 20] H.Alroughani & D.A.McNamara, “The shape synthesis of dielectric resonator antennas”, IEEE Trans. Antennas Propagation, Vol.68, No.8, pp.5766-5777, Aug.2020.

[ALTA 21] FEKO, Altair Inc. (www.altair.com).

[ALTS02] E. Altshuler, "Electrically small self-resonant wire antennas optimized using a genetic algorithm," IEEE Transactions on Antennas and Propagation, vol. 50, no. 3, pp. 297-300, 2002.

[ANSY 20] HFSS, Ansys Inc. (www.ansys.com).

[AOKI 11] Y. Aoki, H. Deguchi, and M. Tsuji, “Reflectarray with arbitrarily-shaped conductive elements optimized by genetic algorithm”, IEEE Antennas and Propagation International Symposium, Spokane, Washington, USA, July 2011.

[BAND 88] J.W.Bandler and S.H.Chen, “Circuit optimization : The state of the art”, IEEE Trans. Microwave Theory Tech., Vol.36, No.2, pp.424-443, Feb.1988.

[BAND69] W. Bandler, “Optimization methods for computer-aided design,” IEEE Transactions on Microwave Theory and Techniques, vol. mtt-17, 1969.

[BOYU 22] M.Boyuan, J.Pan, Y.Liu, D.Yang and Y.Guo, “Higher-order characteristic modes based broad-beam dielectric resonator antenna”, IEEE Antennas and Wireless Propagation Letters, vol. 21, no. 4, pp. 818-822, April 2022.

[CAPE 11] M. Capek, P. Hazdra, and J. Eichler, “A method of tracking characteristic numbers and vectors”, Progress EM. Research B, Vol. 33, pp. 115-134, 2011.

[CAPE 19] M. Capek, L. Jelinek, and M. Gustafsson, “Shape synthesis based on topology sensitivity,” IEEE Trans. Antennas Propag., vol. 67, no. 6, pp. 3889 – 3901, June 2019.

[CHAI 07] R.Chair, A.A.Kishk and K.F.Lee, "Wideband stair-shaped dielectric resonator antennas", IET Microw. Antennas Propag., vol.1, no.2, pp.299-305, April 2007.

[CHAN 77] Y. Chang, R.F. Harrington, “A Surface formulation for characteristic modes of material bodies”, IEEE Trans. Antennas Propagat., Vol. 25, No. 6, pp 789 – 795, November 1977.

[CHEN 19] Z.Chen, S.Zheng and V.Okhmatovski, “Tensor train acceleration of method of moments solution of volume integral equation on structured and unstructured grids”, ICEAA-IEEE APWC, Granada, Spain, Sept.2019.

[CHEN 71] D.K.Cheng, “Optimization techniques for antenna arrays,” Proc. IEEE, vol. 59, no. 12. pp. 1664–1674, Dec. 1971.

[CHOO 05] H. Choo and H. Ling, "Design of electrically small wire antennas using a pareto genetic algorithm," IEEE Transactions on Antennas and Propagation, vol. 53, no. 3, pp. 1038-1046, 2005.

[COLL 19] B.S.Collins, “Practical application of small antennas in hardware platforms”, IET Microwaves, Antennas & Propagation, Vol.13, No.11, pp.1883-1888, 2019.

[DASH 17] S.K.K.Dash, T.Khan and Y.M.M.Antar, “A state-of-art review on performance improvement of dielectric resonator antennas”, Int. Journal of RF and Microwave Computer-Aided Engineering, vol.28, 2018.

[DAUR 15] M. D'Auria, W. J. Otter, J. Hazell, B. T. W. Gillatt, C. Long-Collins, N. M. Ridler and S. Lucyszyn, “3-D printed metal-pipe rectangular waveguides”, IEEE Trans. on Components, Packaging and Manufacturing Technology, vol. 5, no. 9, pp. 1339-1349, Sep. 2015.

[DEEP 09] K.Deep, K.P.Singh, M.L.Kansal and C.Mohan, “A real coded genetic algorithm for solving integer and mixed integer optimization problems”, Applied Mathematics and Computation, Vol.212, No.2, pp.505–518, 2009.

[DENG 19] C.Deng, Z.Xu, A.Ren and S.V.Hum, “TCM-based bezel antenna design with small ground clearance for mobile terminals”, IEEE Trans. Antennas Propagat., vol.67, no.2, pp.745-754, Feb.2019.

[DENG 22] B.Deng, D.Pan, Z.Duan, J.Liu and F.Wu, “A compact 90-96 GHz 6-bit vector modulator phase shifter in 28nm CMOS for phased array applications”, Microwave & Optical Technology Letters, vol.65, no.11, Aug.2022.

[DICA 18] F.A.Dicandia, S.Genovesi and A.Monorchio, “Efficient excitation of characteristic modes for radiation pattern control by using a novel balanced inductive coupling element”, IEEE Trans. Antennas Propagat., Vol.66, No.3, pp.1102-1113, March 2018.

[DICH 97] Dich, M. (1997). Accurate determination of antenna directivity. IEEE Transactions on Antennas and Propagation, 45(10), 1502-1503.

[EREN11] A. Erentok and O. Sigmund, "Topology optimization of sub-wavelength antennas," IEEE Transactions on Antennas and Propagation, vol. 59, no. 1, pp. 58-69, 2011.

[ELSA 22] H. El-Sawaf, W. M. Abdel-Wahab and S. Safavi-Naeini, "Mm-wave 3D-printed DRAs for Cost-effective Emerging 5G- and SatCom Applications", IEEE International Symposium on Antennas and Propagation, pp.1838-1839, Denver, Colorado, USA, July 2022.

[ESSE 96] K. P. Esselle, "A low-profile rectangular dielectric-resonator antenna," in IEEE Transactions on Antennas and Propagation, vol. 44, no. 9, pp. 1296-1297, Sept. 1996, doi: 10.1109/8.535389.

[ETHI 12] J.Ethier & D.A.McNamara, "A Sub-structure characteristic mode concept for antenna shape synthesis", Electronics Letters, Vol.48, No.9, April 2012.

[ETHI 14] J.Ethier and D.A.McNamara, “Antenna shape synthesis without prior specification of the feedpoint locations”, IEEE Trans. Antennas Propagat., Vol.62, No.10, pp.4919-4934, Oct.2014.

[ETHI 14a] J.Ethier, D.A.McNamara, J.Shaker & R.Chaharmir, “Reflectarray synthesis with similarity-shaped fragmented sub-wavelength elements”, IEEE Trans. Antennas Propagation, Vol.62, No.9, pp.4498-4509, Sept.2014.

[ETHI 14b] J.Ethier and D.A.McNamara, “Antenna shape synthesis without prior specification of the feedpoint locations”, IEEE Trans. Antennas Propagation, Vol.62, No.10, pp.4919-4934, Oct.2014.

[FEKO 21] FEKO, Altair Inc. (www.altair.com).

[GOLD 89] David E. Goldberg. 1989. Genetic Algorithms in Search, Optimization and Machine Learning (1st. ed.). Addison-Wesley Longman Publishing Co., Inc., USA.

[GOUD 17] S. Goudos, "Antenna design using binary differential evolution," IEEE Antennas and Propagation Magazine, pp.74-93, Feb.2017.

[GRIF 06] L. Griffiths and C. Chung, "Broadband and multiband antenna design using the genetic algorithm to create amorphous shapes using ellipses", IEEE Transactions Antennas and Propagation, Vol.54, No.10, pp.2776 – 2782, 2006.

[GUST 22a] M.Gustafsson, L.Jelinek, K.Schab and M.Capek, "Unified theory of characteristic modes – Part I : Fundamentals", IEEE Transactions on Antennas and Propagation, vol. 70, no. 12, pp. 11801-11813, Dec. 2022.

[GUST 22b] M.Gustafsson, L.Jelinek, K.Schab and M.Capek, "Unified theory of characteristic modes – Part II : Tracking, Losses, and FEM Evaluation", IEEE Transactions on Antennas and Propagation, vol. 70, no. 12, pp. 11814-11824, Dec. 2022.

[HANS 82] R.C.Hansen, “Linear Arrays”, in : A.W.Rudge, K.Milne, A.D.Olver and P.Knight (Edits.), Handbook of Antenna Design (IEE Electromagnetic Wave Series, 1982).

[HARR 58] R. Harrington, "On the gain and beamwidth of directional antennas," in IRE Transactions on Antennas and Propagation, vol. 6, no. 3, pp. 219-225, July 1958.

[HARR 72] R. F. Harrington, J. Mautz, Y. Chang, “Characteristic modes for dielectric and magnetic bodies,” IEEE Transactions on Antennas and Propagation, Vol. AP-20, No. 2, pp. 194 – 198, March 1972.

[HASS 14] E. Hassan and M. Berggren,”Topology optimization of metallic antennas”, IEEE Transactions on Antennas and Propagation, vol.62, no.5, pp.2488-2500, May 2014.

[HASS 20] E.Hassan, B.Scheiner, F.Michler, M.Berggren, E.Wadbro, F.Röhrl, ”Multilayer topology optimization of wideband SIW-to-waveguide transitions”, IEEE Transactions on Microwave Theory and Techniques, Vol.68, No.4, pp.1326-1339, April 2020.

[HEHE 23] S.P.Hehenburger, S.Caizzone and A.G.Yarovoy, “Additive manufacturing of linear continuous permittivity profiles and their application to cylindrical dielectric resonator antennas”, IEEE Open Journal of Antennas & Propagation, vol.4, pp.373-382, 2023.

[HU 21] L. Hu, Y. Liu, Q. Cheng, and J. Wang, "3D printing of dielectric resonator antennas: recent advances and challenges," IEEE Access, vol. 9, pp. 25287-25300, 2021.

[HUAN 19] H.Huang, Y.Wang and X.Jian, “Novel integrated design of a dual-band dual polarization 5G mm-wave antenna array with a U-slotted full-metal casing for a cellular phone”, 13th European Conf. Antennas Propagation (EuCAP), Krakow, Poland, April 2019.

[IQBA 15] M.S.Iqbal and K.P.Esselle, “A low-profile dielectric resonator antenna for wideband applications”, IEEE Int. Antennas Propagat. Symp. Digest, pp.440-441, Vancouver, Canada, 2015.

[JENS 11] J.S.Jensen and O.Sigmund, “Topology optimization for nano-photonics”, Laser Photonics Review, Vol.5, No.2, pp.308-321, 2011.

[JOHN 99a] J. Johnson and Y.Rahmat-Samii, "Genetic algorithms and method of moments (GA/MOM) for the design of integrated antennas", IEEE Transactions on Antennas and Propagation, vol.47, pp.1606-1614, 1999.

[JOHN 99b] J. Johnson and Y. Rahmat-Samii, "Evolutionary designs of integrated antennas using genetic algorithms and method of moments (GA/MoM)", Electromagnetic Optimization by Genetic Algorithms (Wiley, 1999).

[KAJF 83] D.Kajfez, A.W.Glisson & J.James, “Evaluation of modes in dielectric resonators using a surface integral equation formulation”, IEEE Trans. Microwave Theory Tech., Vol.31, No.12, pp.1023-1029, Dec.1983.

[KAJF 84] D.Kajfez, A.W.Glisson & J.James, “Computed modal field distributions for isolated dielectric resonators”, IEEE Trans. Microwave Theory Tech., Vol.32, No.12, pp.1609-1616, Dec.1984.

[KEYR 16] Keyrouz, S., & Caratelli, D. (2016). Dielectric Resonator Antennas: Basic Concepts, Design Guidelines, and Recent Developments at Millimeter-Wave Frequencies. International Journal of Antennas and Propagation, 2016, 1-20.

[KIM 19] D. -W. Kim, J. -H. Kim and S. Nam, "Beam steering of a multi-port chassis antenna using the least squares method and theory of characteristic modes," in IEEE Transactions on Antennas and Propagation, vol. 67, no. 8, pp. 5684-5688, Aug. 2019, doi: 10.1109/TAP.2019.2920288.

[KISH 07] A.A.Kishk and Y.M.M.Antar, “Dielectric resonator antennas”, Chap.17 in : J.L.Volakis (Edit.), Antenna Engineering Handbook (McGraw-Hill, 2007).

[KUOS 22] M.Kuosmanen, P.Ylä-Oijala, J.Holopainen and V.Viikari, “Orthogonality properties of characteristic modes for lossy structures", IEEE Transactions on Antennas and Propagation, vol. 70, no. 7, pp. 5597-5605, July 2022.

[LAWR 10] J.K.Lawrence, “On the use of natural-mode basis functions for electromagnetic analysis of arbitrary conducting surfaces”, Master’s Thesis, Department of Electrical Engineering, Clemson University, Dec.2010. Available at https://tigerprints.clemson.edu/all_theses/990/

[LI 18] R. Li, D. McNamara, G. Wei and J. Li, "Increasing radiation efficiency using antenna shape optimization approach," in IEEE Antennas and Wireless Propagation Letters, vol. 17, no. 3, pp. 393-396, March 2018.

[LIAN 08] X.-L.Liang and T.A.Denidni, “Cross T-shaped dielectric resonator antenna for wideband applications”, Electron. Lett., vol.44, no.20, pp.1176-1177, Sept.2008.

[LIND 99] D. Linden and E. Altshuler, "Design of wire antennas using genetic algorithms", Chapter 8 in : Y. Rahmat-Samii and E. Michielssen (Edits.), Electromagnetic Optimization by Genetic Algorithms (Wiley, 1999).

[LIU 04] Y.Liu, S.Safavi-Naeini, S.K.Chaudhuri and R.Sabry, "On the determination of resonant modes of dielectric objects using surface integral equations", IEEE Trans. Antennas Propagat., Vol.52, pp.1062-1069, 2004.

[LIU 16] H. Liu and M. Yan, "Electrically small loop antenna standing on compact ground in wireless sensor package," IEEE Antennas and Wireless Propagation Letters, vol. 15, pp. 76-79, 2016.

[LIU 23] Y. -T. Liu, B. Ma, S. Huang, S. Wang, Z. J. Hou and W. Wu, "Wideband low-profile connected rectangular ring dielectric resonator antenna array for millimeter-wave applications," in IEEE Transactions on Antennas and Propagation, vol. 71, no. 1, pp. 999-1004, Jan. 2023, doi: 10.1109/TAP.2022.3164235.

[LO 66] Y.T.Lo, S.W.Lee and Q.H.Lee, “Optimization of directivity and signal-to-noise ratio of an arbitrary antenna array”, Proc. IEEE, Vol.54, No.8, Aug. 1966.

[LUDI 14] D. J. Ludick, J. V. Tonder and U. Jakobus, "A hybrid tracking algorithm for characteristic mode analysis", Int. Conf. Electromagnetics Advanced Applications (ICEAA), Aruba, pp. 455-458, Aug. 2014.

[MATLAB] MATLAB, Matrix Mathematic Language Software. (www.mathworks.com)

[MCNA 20] D.A.McNamara, Notes for Course ELG4118 : Wave Propagation & Antennas, School of Electrical Engineering & Computer Science, University of Ottawa, Canada, 2017.

[MIRH 16] S. Mirhadi and M. Soleimani, "Ultra wideband antenna design using discrete Green's functions in conjunction with binary particle swarm optimisation," IET Microwaves, Antennas & Propagation, vol. 10, no.2, pp.184-192, 2016.

[MISH 21] R. K. Mishra, P. K. Behera, and S. K. Parida, "Miniaturized dielectric resonator antenna using dielectric metamaterial superstrate," IEEE Antennas and Wireless Propagation Letters, vol. 20, no. 1, pp. 149-153, Jan. 2021.

[MUKH 20] B.Mukherjee, P.Patel and J.Mukherjee, “A review of the recent advances in dielectric resonator antennas”, Journal of Electromagnetic Waves and Applications, vol.34, no.9, pp.1095-1158, 2020.

[NASE 21] P.Naseri and S.V.Hum, “A Generative machine learning-based approach for inverse design of multilayer metasurfaces”, IEEE Trans. Antennas Propagation, Vol.69, No.9, pp.5725-5739, Sept.2021.

[NASS 21] M. Nassor, H. Alroughani, E. Almajali, D. A. McNamara and M. C. E. Yagoub, "On the inverse design of dielectric resonator antenna structures for beam-steering," 15th European Conference on Antennas and Propagation (EuCAP), 2021.

[NGUY 21] T. A. Nguyen, A. Abbosh, and B. C. Lovell, "Dielectric resonator antennas fabricated using low-cost 3d printing for wireless communication applications," IEEE Transactions on Antennas and Propagation, vol. 69, no. 2, pp. 789-794, Feb. 2021.

[NOMU 13] T.Nomura, M.Ohkado, P.Schmalenberg, J.Lee, O.Ahmed and M.Bakr, “Topology optimization method for microstrips using boundary condition representation and adjoint analysis”, 43rd European Microwave Conf., pp.632-635, Nuremberg, Germany, Oct.2013.

[OHIR 04] M. Ohira, H. Deguchi, M. Tsuji, and H. Shigesawa, “Multiband single-layer frequency selective surface designed by combination of genetic algorithm and geometry-refinement technique,” IEEE Transactions on Antennas and Propagation, vol. 52, no. 11, pp. 2925-2931, November 2004.

[PAN 16] Y. M. Pan and S. Y. Zheng, "A Low-profile stacked dielectric resonator antenna with high-gain and wide bandwidth," in IEEE Antennas and Wireless Propagation Letters, vol. 15, pp. 68-71, 2016, doi: 10.1109/LAWP.2015.2429686.

[PEAR 84] L.W.Pearson, “The Singularity expansion representation of surface currents on a perfectly conducting scatterer”, pp.229-251 in L.B.Felsen (Edit.), Hybrid Formulation of Wave Propagation and Scattering (Martinus Nijhoff Publishers, Dordrecht, The Netherlands, 1984).

[PETE 97] A.Peterson, S.Ray and R.Mittra, Computational Methods for Electromagnetics (IEEE Press, 1997).

[PETO 07] A.Petosa, Dielectric Resonator Antenna Handbook (Artech House, 2007).

[PETO 10] A.Petosa and A. Ittipiboon, "Dielectric resonator antennas: A historical review and the current state of the art," in IEEE Antennas and Propagation Magazine, Vol.52, No.5, pp.91-116, Oct.2010.

[PHIL 21] C.Phillips and V.I.Okhmatovski, “Fast direct solution of 2D scalar volume integral equation via tensor train decomposition for scatterers of arbitrary shape”, Int. Applied Computational Electromagnetics Society (ACES) Symposium, August 2021 [Virtual Symposium].

[QAMA 20] A. Qamar, M. Tariq, S. Muhammad, and S. S. Hasan, "Design of a wideband dielectric resonator antenna using a metamaterial ground plane," IEEE Antennas and Wireless Propagation Letters, vol. 19, no. 1, pp. 71-75, Jan. 2020.

[RAHM 99] Y. Rahmat-Samii and E. Michielssen (Edits.), Electromagnetic Optimization by Genetic Algorithms (Wiley, 1999).

[RAHM 07] Y. Rahmat-Samii, Reflector Antennas, Chapter 15 in: J. L. Volakis (Edit.), Antenna Engineering Handbook (McGraw-Hill, 2007), 4th Edition.

[RAIN 12] B. Raines, and Roberto Rojas, “Wideband characteristic mode tracking”, IEEE Trans. Antennas Propagat., Vol. 60, No. 7, pp.3537-3541, July 2012.

[RAO 13] S. Rao, L. Shafai, and S. K. Sharma (Edits.), Handbook of Reflector Antennas and Feed Systems, Vol. I, II, and III (Artech House, 2013).

[RIBL 48] H. J. Riblet, “Note on the maximum directivity of an antenna,” Proc. IRE, vol. 36, no. 5, pp. 620–623, 1948.

[RODR 20] R.Rodríguez-Cano, S.Zhang and G.F.Pedersen, “Transparent mm-wave array on a glass substrate with surface wave reduction, 14th European Conf. Antennas Propagation (EuCAP), Copenhagen, Denmark, March 2020.

[SALU 18] M. Salucci, F.Robol, N.Anselmi, M.A.Hannan, P.Rocca, G.Olivieri, M.Donelli and A.Massa, "S-Band spline-shaped aperture-stacked patch antenna for air traffic control applications," IEEE Transactions on Antennas and Propagation, vol. 66, no. 8, pp. 4292-4297, 2018.

[SINC 48] G.Sinclair, “Theory of models of electromagnetic systems”, Proc.IRE, Vol.36, pp.1364-1370, 1948.

[SING 22] S.S.Singhwal, L.matekovits, B.K.Kanaujia, J.Kishor, S.Fakhte and A.Kumar, “Dielectric resonator antennas”, IEEE Antennas and Propagation Magazine, , pp.26-39, June 2022.

[STUT 08] W.Stutzman and S.Licul, “Synthesis Methods for Antennas” in C.A.Balanis (Edit.), Modern Antenna Handbook (Wiley, 2008) pp.631.

[THAM 10] L.Z.Thamae and Z.Wu, “Broadband bowtie dielectric resonator antenna”, IEEE Trans. Antennas Propagat., vol.58, no.11, pp.3707-3710, Nov.2010.

[THOR 05] B. Thors, and H. Holter, "Broadband fragmented aperture phased array element design using genetic algorithms", IEEE Transactions Antennas propagate vol. 53, pp. 3280-3287, 2005.

[TOIV 10] J. Toivanen and P. Ylä-Oijala, “Gradient-based shape optimization of ultra-wideband antennas parameterized using splines,” IET Microwaves, Antennas & Propagation, vol. 4, pp. 1406-1414, 2010.

[TOIV10] J. Toivanen and P. Ylä-Oijala, “Gradient-based shape optimization of ultra-wideband antennas parameterized using splines,” IET Microwaves, Antennas Propagat., vol. 4, pp. 1406-1414, 2010.

[TREF 11] L.N.Trefethen, “Trefthen’s Index Cards – Forty Years of Notes About People, Words and Mathematics” (World Scientific Publishers Ltd, 2011).

[WANG 22] L. Wang et al., "Stable high-gain linearly and circularly polarized dielectric resonator antennas based on multiple high-order modes," in IEEE Transactions on Antennas and Propagation, vol. 70, no. 12, pp. 12270-12275, Dec. 2022, doi: 10.1109/TAP.2022.3209627.

[WELZ 91] Welzl, E. (1991), 'Smallest enclosing disks (balls and ellipsoids)', Lecture Notes in Computer Science, Vol. 555, pp. 359-370.

[WU 17] Q.Wu, “Computation of characteristic modes for dielectric bodies using volume integral equation and interpolation”, IEEE Antennas Wireless Propagat. Lett., Vol.16, pp.2963-2966, 2017.

[YAMA 09] T. Yamamoto and T. Tsukagoshi, "Efficient antenna miniaturization technique by cut off of chromosome-length in genetic algorithm," Asia Pacific Microwave Conference, Singapore, pp. 1837-1840, 2009.

[YANG 07] L. Yang, A. Rida, R. Vyas, and M. M. Tentzeris, “RFID tag and RF structureson a paper substrate using inkjet-printing technology,” IEEE Trans. Microw. Theory Tech., vol. 55, no. 12, pp. 2894–2901, Dec. 2007.

[YANG 19] B. Yang and J. Adams, "A shape-first, feed-next design approach for compact planar MIMO antennas," Progress in Electromagnetics Research, Vol. 77, 157–165, 2019.

[YAO 21] H. Yao, L. Zhang, Y. Liu, and J. Wang, "A Wideband dielectric resonator antenna with stepped cross-section and optimized feeding," IEEE Antennas and Wireless Propagation Letters, vol. 20, no. 3, pp. 476-480, March 2021.

[ZHAN 21] J. Zhang, C. Wu, J. Li, and Y. Chen, "A Triple-band dielectric resonator antenna with controllable frequencies using multiple split-ring resonators," IEEE Antennas and Wireless Propagation Letters, vol. 20, no. 2, pp. 255-259, Feb. 2021.

[ZHAO 19] K.Zhao, S.Zhang, Z.Ho, O.Zandar, T.Bolin, Z.Ying and G.F.Petersen, “Spherical coverage characterization of 5G millimeter wave user equipment with 3GPP specifications”, IEEE Access, Vol.7, pp.4442-4452, Jan.2019.

[ZHEN 20] Y. Zheng, C. Liu, Y. Liu, and Y. Liu, "Dual-band dielectric resonator antenna with multi-band rejection using hybrid metamaterial," IEEE Access, vol. 8, pp. 30180-30188, 2020.

[ZHOU 22] L.Zhou, Y.Huang, Z.Zhang and L.Zhou, “A low-profile and broadband silicon-based dielectric resonator antenna”, International Symposium on Antennas & Propagation (ISAP), Sydney, Australia, 2022.

[ZUO 20] L.Zuo, C. Lv, Y. Jiao, and Y. Wang, "A Hybrid dielectric resonator antenna with improved bandwidth and impedance matching," IEEE Transactions on Antennas and Propagation, vol. 68, no. 5, pp. 3385-3389, May 2020.

APPENDIX : GENETIC ALGORITHM SETTINGS

Option Name	Value/Type	Description/ Note
Population Type	Bit String	Every bit in the chromosome signifies a block in the structure: 1 signifies block presence and 0 absence. Used for shaping.
	Double Vector	Used for finding port weights in 6-bit phaser case.
Population Size	100	The number of individuals.
Initial Population	Specified	Initial geometry from a previous optimization run was used in the final optimization.
Scaling Function	Proportional	"The scaling function converts raw fitness scores returned by the fitness function to values in a range that is suitable for the selection function. Proportional makes the expectation proportional to the raw fitness score" [125].
Selection Factor	Tournament	"Selects each parent by choosing individuals at random" the default number (4) was selected.
Reproduction	Elite count	Five elite individual with best fitness scores survive to the next generation.
Mutation function	Uniform	"Mutation functions make small random changes in the individuals in the population, which provide genetic diversity and enable the genetic algorithm to search a broader space.". Uniform was selected since it does not make a difference since 0 and 1 are used here

[125] The content is taken from MATLAB description of each option listed in the MATLAB manual. The tabular format was suggested by H. Alroughani.

Mutation Rate	0.01	The default value was used.
Crossover	Scattered	This combines two parents to produce a new individual for the subsequent generation. A random binary is created. If the random vector has "1" then it take a gene from the first parent and if "0" it takes it from the second parent.
Migration	Both	Both is the migration of the nth subpopulation migrates into both the (n–1)th and the (n+1)th subpopulation. This intends to move individual between subpopulations.
Migration Fraction	0.2	The default value was used.
Generation	20	Number of specified generations.
Stall Generation	2	"If the average change in the fitness function value over Stall generations is less than Function tolerance, the algorithm stops".
Function Tolerance	1e-6	The default value was used.